IPP-Report

MAX-PLANCK-INSTITUT
FÜR PLASMAPHYSIK

Riccardo Stucchi

Non-Maxwellian Distribution Functions: Landau Damping and Beyond

IPP 2024-17
Juli 2024

Technische Universität München
Max Planck Institut für Plasmaphysik

Non-Maxwellian Distribution Functions: Landau Damping and Beyond

Riccardo Stucchi

Thesis submitted
within the Master program in Physics
(Applied and Engineering Physics)

Supervisor: Dr. Philipp Lauber
Second Examiner: Dr. Gregor Birkenmeier

November 22, 2023

Contents

Motivation

$\pi\lambda\acute{\alpha}\sigma\mu\alpha$ is commonly referred to as the fourth state of matter. It emerges when, at sufficiently high temperature, the atoms of a gas dissociate into electrons and ions, and the system gets electromagnetically activated. In the context of kinetic theory, plasma species are described by the distribution function $f(\mathbf{x}, \mathbf{v}, t)$, that quantifies the probability of finding a particle in an infinitesimal phase-space volume $d^3\mathbf{x}d^3\mathbf{v}$ around $(\mathbf{x}, \mathbf{v})$.

Assuming that collisions between particles are elastic and that the average time between collisions is significantly shorter than the time scales of the physical processes under consideration, the statistical equilibrium of a plasma is typically and accurately characterized by the Maxwell-Boltzmann distribution function. However, in certain less frequent yet significant and intriguing scenarios, the distribution function deviates considerably from the Maxwell-Boltzmann distribution (see Fig. 1):

- **Kappa κ distributions:** In space plasmas, such as in the solar wind and in solar corona, particle populations can be often described by κ distributions. κ distributions emerge as the stable statistical equilibrium in the context of non-extensive statistical mechanics [1] and, compared to Maxwellian distributions, they feature high energy tails. They are tightly bound with the concept of correlation between particles [2]: as collisionality increases, the particle correlation is destroyed and one retains the correlation-free Maxwellian distribution.

- **Incomplete distributions:** In laboratory plasmas, in presence of potential barriers, such as sheats near material walls or probes, a trapped-passing boundary is created for one or more species. As a consequence, at the edge of an absorbing wall sheath the passing interval of the electron distribution will be empty, and an incomplete distribution is created.

- **Slowing-Down distribution:** In ignited fusion plasmas, 3.5MeV α particles are produced isotropically via the Deuterium-Tritium fusion reaction. Given their high energy compared to the background and due to the low intra-species collisionality, α particles do not thermalize to a Maxwellian state. Instead, they slow-down via collisions with the background plasma to a stable distribution known as Slowing-Down, whose functional dependence is derived from the Fokker-Planck equation [3].

The present master's thesis originates from the objective of extending the linear gyrokinetic dispersion relation for shear Alfvèn waves [4] to include non-Maxwellian velocity distributions, in particular the Slowing-Down distribution. From a practical standpoint, this generalization primarily involves the implementation of an all-solve numerical scheme, initially proposed by Xie [5], to computationally evaluate integrals of the following form:

$$\int \frac{f(v)}{v - z} dv. \tag{1}$$

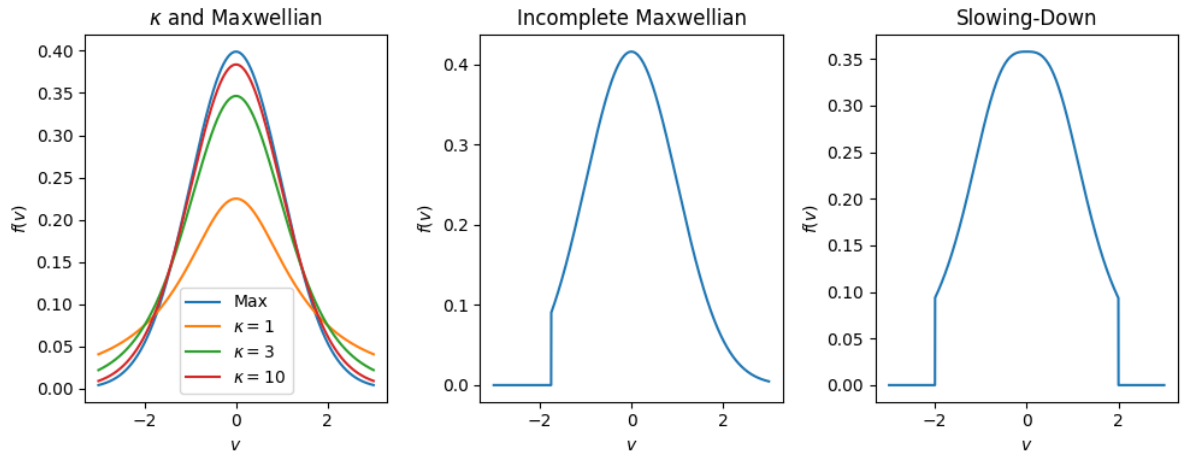

Figure 1: Examples of distribution functions.

While the integration of such an integral for Maxwellian distributions can be conveniently expressed using the Faddeeva function, a readily computable function available in standard numerical libraries, the same does not hold true for non-Maxwellian distributions. In these cases, the aforementioned algorithm proves to be invaluable.

In the original paper, the numerical scheme was introduced and examined within the context of the 'simple' Landau damping problem. In the present work, a thorough review of the original work is conducted (Chapter 5), including an error analysis dependent on the scheme's parameters. This analysis essentially confirms the method's validity, contingent upon the proper adjustment of these parameters, and leads us to delineate a simple strategy to adopt when better accuracy is required.

Mathematically, the algorithm is founded on the well-established Landau's integration contour and analytical continuation techniques. However, in the current investigation, it has become apparent that these methods are not totally well-defined when the distribution function has compact support or exhibits other non-analytical characteristics. Therefore, the aim of Part I, i.e. chapters 1 to 4, is to delve deeper into the Landau damping problem in the context of non-entire distribution functions. This aim extends well beyond the original intentions of Xie's paper and necessitates a reevaluation of Landau's original description of Landau damping.

Part II, i.e. chapters 6 to 9, is instead dedicated to the implementation of Xie's numerical scheme into the linear gyrokinetic dispersion relation for Shear Alfvén waves. First, we generalise the dispersion relation to non-Maxwellian distributions. Subsequently, after analysing potential obstacles connected to the extension to non-Maxwellian distributions, we provide some example solutions for the generalised dispersion relation.

Part I

Landau Damping

Chapter 1

Landau Damping: Introduction

In this chapter, we introduce the Landau damping phenomenon. After a brief historical overview (Sec. 1.1), we present the main physical interpretations of the phenomenon (Sec. 1.2). While drawing inspiration from the explanations of Chen [6] and O'Neil [7], the exposition here features additional illustrations that, as we believe, might help in the intuitive understanding of the phenomenon. Finally, Sec. 1.3 outlines the structure of the upcoming chapters in Part I.

1.1 Historical Overview

In the realm of plasma kinetic theory, the high frequency longitudinal electrostatic dynamics is described by the Vlasov-Poisson (VP) system of equations,

$$\frac{\partial f_{e,1}}{\partial t} + v\frac{\partial f_{e,1}}{\partial x} - \frac{e}{m_e}E\frac{\partial f_{e,0}}{\partial v} - \frac{e}{m_e}E\frac{\partial f_{e,1}}{\partial v} = 0, \tag{1.1}$$

$$\frac{\partial E}{\partial x} = -\frac{e}{\epsilon_0}\int \mathrm{d}v f_{e,1}, \tag{1.2}$$

where $f_{e,0}(v)$ and $f_{e,1}(x,v,t)$ are respectively the equilibrium and perturbation parts of the 1D electron distribution function $f_e(x,v,t)$. It is assumed that the ions are motionless and represent a constant uniform neutralizing distribution $f_i(v)$, such that

$$\sum_s \rho_s = \int \left[ef_i(v) - ef_{e,0}(v) - ef_{e,1}(x,v,t)\right]\mathrm{d}v = -e\int f_{e,1}(x,v,t)\mathrm{d}v. \tag{1.3}$$

Moreover, the 1D electron distribution function $f_e(x,v,t)$ corresponds to the 3D electron distribution function integrated over the 2 dimensions transversal to the wave vector $\mathbf{k} = k\hat{\mathbf{k}}$,[1]

$$f_e(x,v,t) = \int f_e(\mathbf{x},\mathbf{v},t)\mathrm{d}^2\mathbf{x}_\perp\mathrm{d}^2\mathbf{v}_\perp = f_{e,0}(v) + f_{e,1}(x,v,t). \tag{1.4}$$

The first significant attempt to address the linear Vlasov-Poisson (LVP) system[2] was made by Vlasov in the early 1940s [8]. He sought real-frequency solutions of the form $const \cdot e^{-i\omega t + ikx}$ and derived a dispersion relation $\omega = \omega(k)$ that contained a problematic divergent integral,

$$\epsilon(\omega,k) = 1 + \frac{1}{k\epsilon_0}\frac{e^2}{m_e}\int_{-\infty}^{\infty}\frac{\partial f_{e,0}(v)/\partial v}{\omega - kv}\mathrm{d}v = 0. \tag{1.5}$$

[1] Here, when referring to the dimensions of the distribution function, we condense the spatial dimension and the corresponding velocity dimension into a single dimension. In other words, the coordinates (x,v) account for a single dimension.

[2] The linearization simply consists in setting the term $E\frac{\partial f_{e,1}}{\partial v}$ from Eq. (1.1) to zero.

To overcome this singularity problem, he resorted to taking the Cauchy principal value of the integral. However, as later pointed out by Landau [9], this choice was not justified and resulted in incorrect results. Landau himself then revisited Vlasov's treatment and, by allowing for complex oscillation frequencies and by employing appropriate complex integration techniques, he astonished the community by predicting a wave-damping phenomenon in a collisionless plasma, i.e., Landau damping. Practically, when solving the LVP system, Landau demonstrated that the electric field solution exponentially decreases over time.

During the first $10-15$ years after the publication, Landau's paper remained in the shade, and it was cited and used in only a few publications because of the absence of research programs investigating hot collisionless plasmas. These few early publications mainly focused on explaining Vlasov's ill-defined dispersion relation and finding more physical ways to avoid its singularity. Landau's mathematical approach had managed to circumvent the singularity problem but had not provided a physical explanation for the singularity itself. In this context, Van Kampen [10] demonstrated that Vlasov's initial approach was not wholly incorrect, and he showed that general electric field solutions — even Landau-damped ones — could be expressed as a superposition of a continuous set of real-frequency singular eigenfunctions.

The early 1960s marked a significant turning point for the recognition of Landau damping. Firstly, the experimental verification by Malberg and Wharton [11], complemented by an intuitive and physical derivation by Dawson [12], affirmed the effect's physical reality. Secondly, large-scale fusion research programs gained prominence, and the importance of Landau damping for fusion plasmas was recognized right away. Consequently, research into Landau damping branched into two primary directions. On one side, a more fundamental approach, closely tied to the VP system (both linear and nonlinear), aimed to uncover the fundamental nature of the phenomenon and provide a more rigorous mathematical foundation. On the other side, a more pragmatic approach identified Landau damping in virtually all other modes of plasma oscillations, and it unveiled and studied the profound impact of Landau damping on plasma systems, for instance, in terms of anomalous transport in both fusion and astrophysical plasmas.

Today, after more than 70 years since its prediction, Landau damping is still an extremely living concept. It is one of the building blocks of modern plasma physics,[3] and the methods developed for its study have proven their effectiveness in other areas of physics (gravitating systems, continuum mechanics, high energy physics, biological systems[4]). Moreover, the mathematical community also recognized its significance when, in 2010, Villani was awarded the Fields Medal for his work on nonlinear Landau damping [14]. However, despite its long story of success, Landau damping remains enigmatic in some regards, and its interpretation in various specific settings is still a challenging problem.

As a final comment aimed at avoiding potential confusion, a brief remark on the adopted terminology is required. Strictly speaking, Landau damping refers to the collisionless damping phenomenon for any kind of plasma oscillation. Despite this, with a slight abuse of notation, we will use the expressions "Landau damping problem" and "VP problem" interchangeably, since in the first chapters of this thesis, we will analyze Landau damping exclusively in the context of the VP problem.

[3] Ryutov [13] estimated that "approximately every third paper on plasma physics and its applications contains a direct reference to Landau damping"

[4] See Ryutov's review [13] for references to Landau damping outside plasma physics.

1.2 Physical Pictures and Interpretations of Landau Damping

The literature concerning the fundamental understanding of Landau damping is extensive and continually expanding. It includes a broad spectrum of interpretations and derivations whose compatibility with one another is frequently far from being proven. Furthermore, this range of approaches varies from being more intuitive, albeit less rigorous, to being more rigorous, but often shrouded in an obscure cloak of intricate mathematical abstractions. Therefore, providing a comprehensive, organic, and up-to-date overview of the current state of the art is challenging. And we turn down this challenge. Instead, we will limit our discussion to the two concepts that recur the most in textbook explanations of Landau damping, i.e., wave-particle interaction and phase mixing, and we will later offer a concise overview of crucial aspects that challenge the standard physical interpretations, calling for a deeper investigation into the damping phenomenon.

1.2.1 Wave-Particle Interaction

The very essence of the Landau damping phenomenon corresponds to the wave-particle interaction. To gain a simple picture of the physics involved, we perform an elementary simulation, where a monochromatic electric field interacts with a 1D population of independent charged particles. A population of $N = 200000$ particles, starting from a spatially uniform Maxwellian distribution at $t = 0$, evolves according to the equation of motion

$$m\frac{\mathrm{d}^2x}{\mathrm{d}t^2} = -eE\sin(kx - \omega t). \tag{1.6}$$

Under the *a priori* assumption that $E(t)$ undergoes small damping, we set E, the amplitude of the electric field, as a constant.[5,6] To simulate the particle dynamics, we employ a straightforward Euler scheme and we consider only the spatial region $[-\pi/k, \pi/k]$. This means that whenever the equation of motion brings a particle outside $[-\pi/k, \pi/k]$, we shift the particle position by one wavelength, back into $[-\pi/k, \pi/k]$. This shift does not alter the force acting on the particle and simulates a distribution function spread over an infinite length in the wave field's propagation direction. The results are shown in figures 1.1 and 1.2.[7] Two main conclusions can be drawn:

- The total kinetic energy of the particle population, defined as $E_k(t) = \frac{m}{2}\sum v_i(t)^2$, increases and, because of energy conservation, this gain has to occur at the expense of the wave energy. Wave damping is thus predicted.
- The particle velocity distribution function is primarily affected in the resonant region $v \approx \omega/k$, indicating that particles with velocities close to the wave phase velocity are the key contributors to the energy exchange.

To better understand how to the energy exchange process works, we consider the phase space diagram in the wave reference frame of Fig. 1.3.[8] A particle with initial conditions (x'_0, v'_0) will trace a path along the constant energy curve,

$$\frac{mv'^2}{2} - \frac{eE}{k}\cos(kx') = H(x'_0, v'_0) = \frac{mv'^2_0}{2} - \frac{eE}{k}\cos(kx'_0),$$

[5] If we consider $E(t) = e(t)e^{-\gamma t}$ as an ansatz, we can expand $E(t) = e(t)(1 - \gamma t)$ as $\gamma \to 0$ and consider $e(t)\gamma t$ as a next order term in the equation of motion, Eq. (1.6).

[6] The simple dynamical system of Eq. (1.6) is the basis of the derivations of Stix [15] and Chen [6], that reproduce Landau's original result in the limit of small damping $\gamma \ll \omega$ (see Sec. 2.2). The assumption of constant E has been contested in Ref. [16].

[7] The simulation was run with the following parameters: $m = 1$, $k = 1$, $\omega = 1$, $E = 1/(2\pi)$, $e = 1$.

[8] The suggested explanation is inspired, but not identical, to the one provided in Ref. [6].

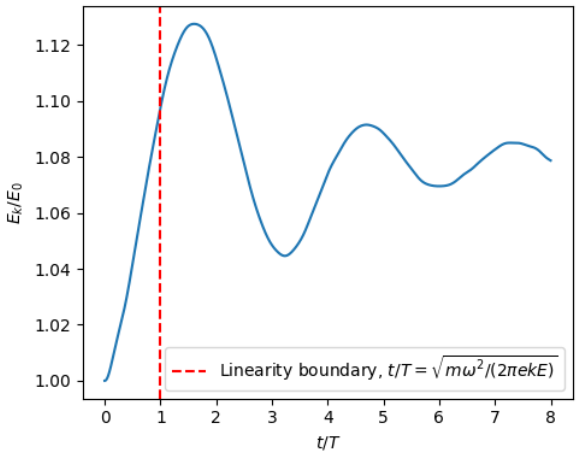

Figure 1.1: Temporal evolution of the total kinetic energy $E_k(t)$ of the particles. The total kinetic energy is normalised to $E_0 = \frac{m}{2}\sum v_i(0)^2$, time t is normalized to $T = 2\pi/\omega$.

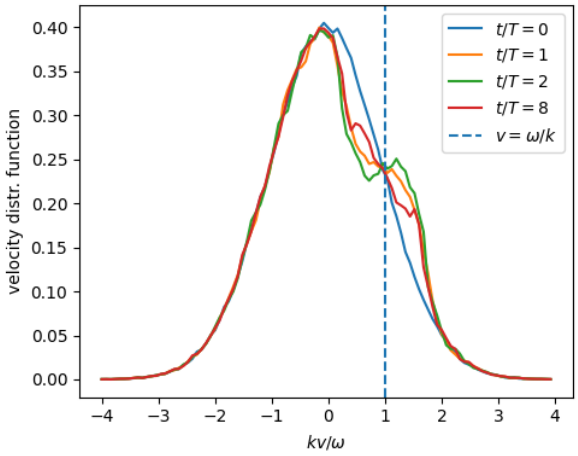

Figure 1.2: Comparison of the velocity distribution function (spatially averaged) at different time points. The velocity axis is normalized to vk/ω.

where the dash denotes the coordinates in the wave reference system, defined by

$$\begin{cases} v' &= v - \frac{\omega}{k}, \\ x' &= x - \frac{\omega}{k}t. \end{cases} \tag{1.7}$$

Let us focus on short time scales where particles do not complete a full $(x_0, v_0) \to (x_0 + 2\pi n/k, v_0)$ cycle.[9] To be more quantitative, we follow [17] and set $\tau_{osc} = \sqrt{m/(ekE)}$ - i.e., the inverse of the oscillation frequency of a particle in a quadratic electric potential - as a measure of these time scales. Moreover, let us first consider only passing particles with $v > \omega/k$. The initial condition is represented in the left sub-figure of Fig. 1.4: the Maxwellian distribution induces a particle gradient on the $H(x_0, v_0)$ curve and we distinguish two regions at higher particle concentration (yellow and orange) and one region in between at lower particle concentration. As time progresses, the 3 regions flow to the right and the orange region progressively jumps

[9] $n = 0$ for trapped particles ($H(x_0, v_0) < eE/k$, closed orbits) and $n = 1$ for passing particles ($H(x_0, v_0) > eE/k$, open orbits).

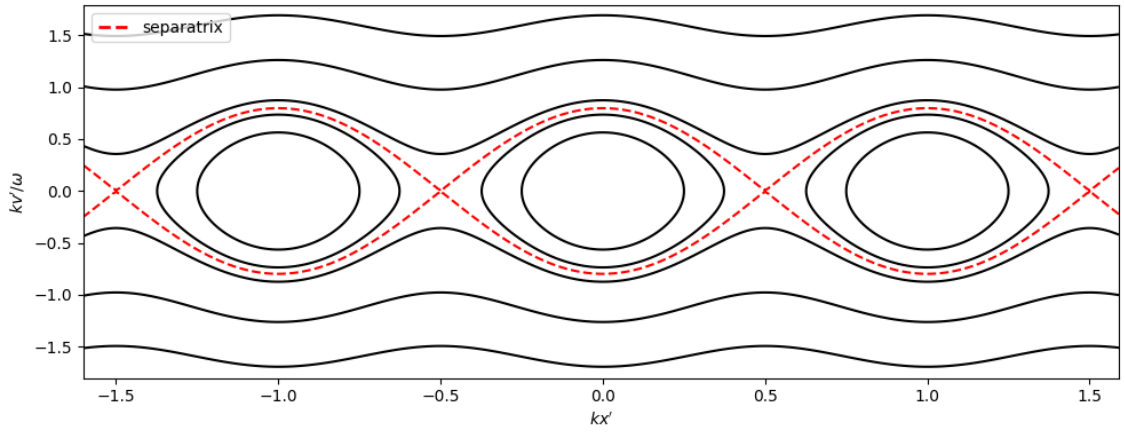

Figure 1.3: Phase-space diagram in the wave reference frame, with $m = 1$, $k = 1$, $E = 1/(2\pi)$. The black solid curves represent constant energy curves; the red dashed line separates open and closed orbits. The wave reference frame coordinates (x', v') are normalized to $(x'/k, kv'/\omega)$. In the given v range $[-v_a, v_a]$, the particle concentration is maximum at $-v_a$ and minimum at v_a

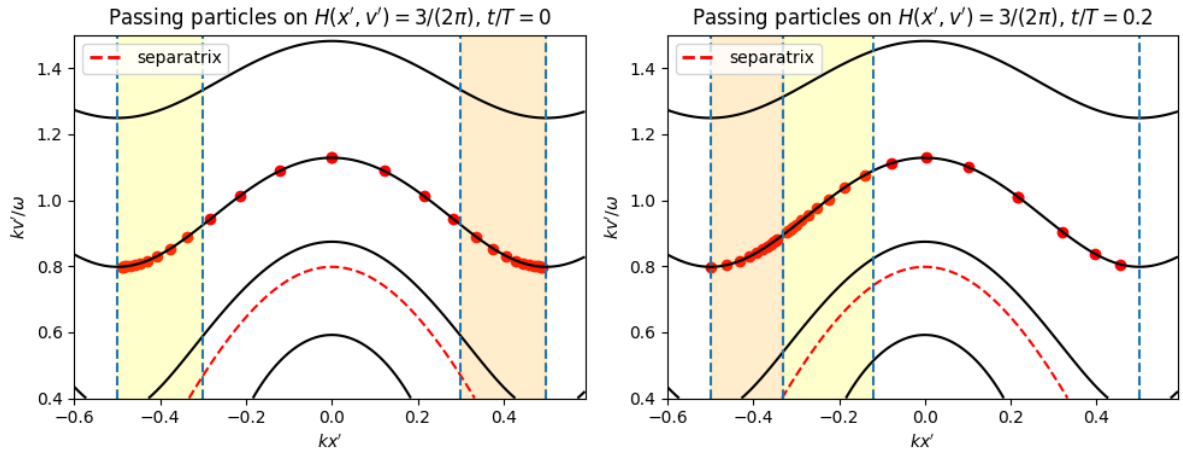

Figure 1.4: Phase-space location for passing particles $H(x', v') = 3/(2\pi)$, for two different time points, $t = 0$ (**Left**) and $t/T = 0.2$ (**Right**).

from the far right to the far left. As depicted in the right sub-figure of Fig. 1.4, we end up in a scenario where the higher concentration regions are on the left side and gaining energy, while the low concentration regions are on the right side and losing energy. We conclude that passing particles with $v > \omega/k$ absorb energy. With a very similar argument we can show that the same conclusion holds true for passing particles with $v < \omega/k$ and trapped particles. The introduced mechanism thus qualitatively explains the energy absorption that occurs at short time scales (see Fig. 1.1 at $t < \tau_{osc}$) and the wave damping, associated through energy conservation to this energy gain, corresponds to the linear Landau damping.

1.2.2 Phase Mixing

A more mathematical interpretation of Landau damping is related to the concept of phase mixing and emerges naturally when solving the LVP system for the distribution function $f_{e,1}$, instead of directly for the electric field. Intuitively, it corresponds to the idea that the integral

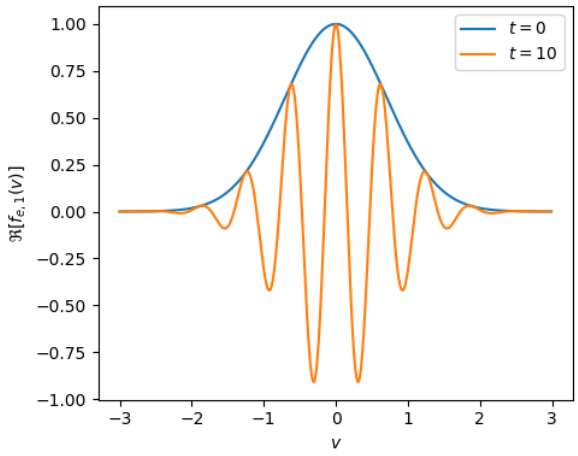

Figure 1.5: Comparison of $\Re[f_{e,1}(v)]$ at $t = 0$ and $t = 10$. $f_{e,1}(v)$ evolves according to Eq. (1.9)

of a rapidly oscillating function is close to zero and it is mathematically based on the Riemann property of Fourier transforms, namely the fact that under proper smoothness conditions the Fourier transform of a function goes to zero as t goes to infinity,

$$\left| \int_{-\infty}^{\infty} g(\omega) e^{-i\omega t} \mathrm{d}\omega \right| \to 0, \quad \text{as } t \to \infty. \tag{1.8}$$

To get a qualitative idea of phase mixing for the LVP system, one considers the approximate expression [17]

$$\frac{\partial f_{e,1}(v)}{\partial t} \approx -i \cdot const \cdot v f_{e,1}(v), \tag{1.9}$$

which has dispersion relation

$$\omega = const \cdot v. \tag{1.10}$$

Eq. (1.10) indicates that Eq. (1.9) has different eigenfrequencies for different points in velocity space. Thus, as depicted in Fig. 1.5, an initially smooth velocity distribution function will lose smoothness due to the fact that different velocity components oscillate at different frequencies. The electric field,

$$E = \frac{1}{ik} \frac{q}{\epsilon_0} \int_{-\infty}^{\infty} f_{e,1}(v) \mathrm{d}v, \tag{1.11}$$

is then the integral of a rapidly oscillating function — in the v-variable — as $t \to \infty$, hence the damping.

As a side note, despite Eqs. (1.9)-(1.11) being deduced under the linear approximation, the concept of phase-mixing is crucial for the interpretation of non-linear Landau damping as well. For further details about this aspect, we refer to the work of Villani and Mouhot [14].

1.2.3 An Additional Perspective on the Small Damping Non-Linear Regime

Up to this point, our primary focus has been directed at the linear damping, that constitutes the central theme of this thesis. In the context of the simplified model introduced in Sec.1.2.1, the linear regime describes the system at short time scales $t < \tau_{osc}$. Nevertheless, by exploiting the same simplified model, we can offer a straightforward explanation for the non-linear phase depicted in Fig. 1.1 at $t > \tau_{osc}$. Returning to the phase space diagram, we initialize particles according to the same spatially uniform Maxwellian distribution and track the evolution of

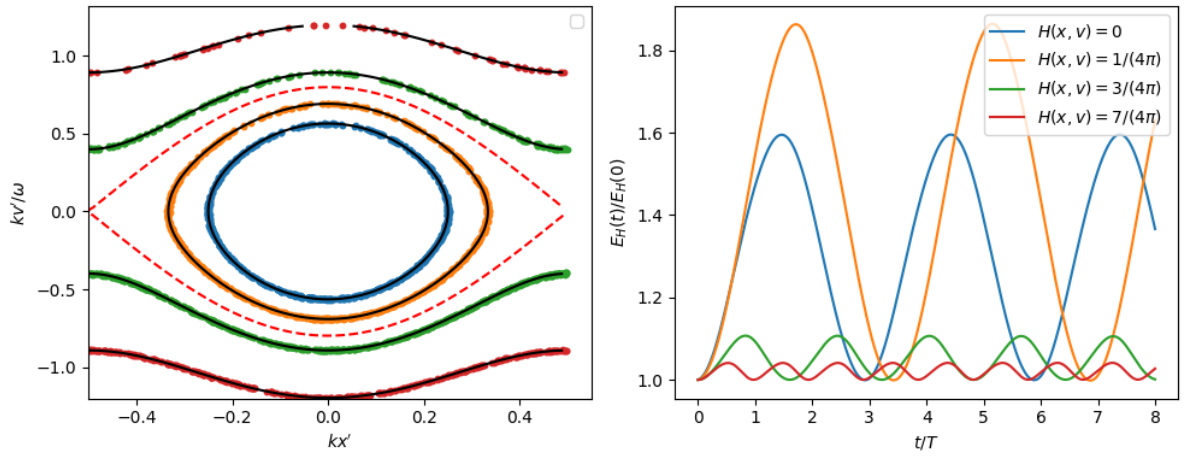

Figure 1.6: Left - The chosen particles are plotted on the corresponding orbit in phase space. Notice that due to the velocity gradient, particles with higher velocity are more sparse. **Right** - Temporal evolution of the total kinetic energy $E_H(t)$ on single orbits.

kinetic energy in two different cases. Initially, we examine individual phase space trajectories and plot the evolution of the kinetic energy $E_H(t)$, defined as:

$$E_H(t) = \left[\frac{m}{2}\sum_i v_i(t)^2\right]_{H<H(x_i,v_i)<H+\delta H} \tag{1.12}$$

In the right sub-figure of Fig. 1.6, the kinetic energy evolution for particles moving along the orbits $H = [0, 1/(4\pi), 3/(4\pi), 7/(4\pi)]$ is displayed. Two observations can be drawn from Fig. 1.6:

1. The total kinetic energy of particles following a single orbit exhibits stable oscillations over time. This is expected, since phase space orbits are periodic in the velocity variable. The oscillation frequency increases for orbits farther from the resonance (where the absolute value of velocity is larger), and the oscillation amplitude increases near the separatrix $H = 1/(2\pi)$, where the difference $v_{max} - v_{min}$ along a trajectory is larger.[10]

2. Most importantly, we notice that the initial kinetic energies $E_H(0)$ are near an $E_H(t)$ oscillation minimum, and that $E_H(t)$ oscillates around an average value larger than $E_H(0)$. This fact is a consequence of the velocity distribution gradient. A flatter distribution function or an inverted sign gradient would result in $E_H(t)$ oscillations starting at points farther from an oscillation minimum.

Now, let us consider a different case by taking into account the kinetic energy evolution of particles moving in the region $H < H(x, v) < H + \Delta H$. Here, we define

$$E_{H,\Delta H}(t) = \left[\frac{m}{2}\sum_i v_i(t)^2\right]_{H<H(x_i,v_i)<H+\Delta H}. \tag{1.13}$$

The right sub-figure of Fig. 1.7 shows $E_0(t)$, $E_{0,1}(t)$ and $E_{0,10}$. A crucial observation is made: increasing ΔH suppresses the oscillation amplitude observed in 1.6. In other words, 1.7 provides a vivid illustration of phase mixing: the summation of stable oscillations with different

[10] This is not completely true, as it appears that the maximum amplitude occurs around $H = 1/(4\pi)$. Further investigation on this aspect is required, and may clarify which orbits contribute the most to the energy exchange.

frequencies leads to a suppressed oscillation. Moreover, since $E_k(t)$ from Fig. 1.1 corresponds to $E_{-1/(2\pi),\infty}(t)$, Fig. 1.7 shows that by including all orbits $E_{H,\Delta H}(t)$ returns the kinetic energy evolution $E_k(t)$ of the whole system (Fig. 1.1).

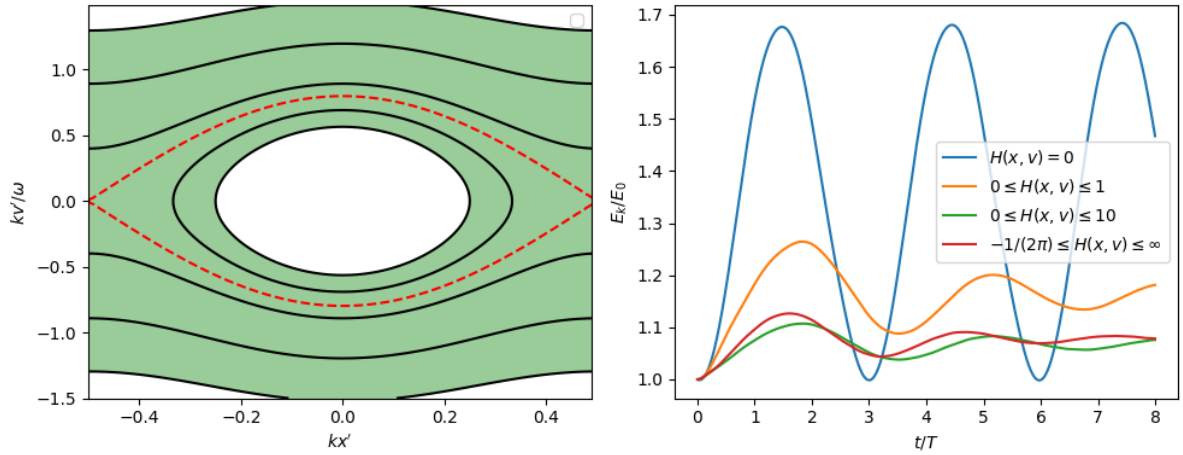

Figure 1.7: Left - Green region corresponds to orbits with $0 \leq H \leq 1$. **Right** - Temporal evolution of the total kinetic energy $E_{H,\Delta H}(t)$ for different regions in phase space.

From the previous observations, we arrive at the following conclusions: under the approximation of small damping, linear Landau damping can be explained as the initial response of the collective motion of particles on single orbits, transitioning to a higher energy configuration, as discussed in Sec. 1.2.1). On the other hand, the non-linear phase features a suppressed oscillation around an energy value larger than the initial energy value. The oscillation suppression can be explained in terms of phase mixing of stable oscillations, while the final energy value is still a consequence of the fact that the initial configuration is a low energy state because of the (negative) velocity gradient. Hence, because of energy conservation, the particle population energy gain directly implies an energy loss for the interacting electric field $E(t)$, and a non-linear phase for the damping of the wave is predicted.

As final comments, we reiterate the importance of the small damping assumption for the simplified model used. If this condition is not met, accounting for the electric field in a consistent manner — as in Eq. (1.11) — is mandatory. Moreover, it is worth noticing that in the current and previous sections we have employed the concept of phase mixing in two different ways. The phase mixing in 1.2.2 involves $f_{e,1}$ and applies to the general VP system (both linear and non-linear), while the phase mixing in Sec. 1.2.3 involves kinetic energy oscillations, and applies only to the non-linear phase of the small damping model (introduced in section 1.2.1).

1.2.4 Landau Damping, Alternative Problems and Interpretations

Finally, here is a list of some of the complementary aspects that come up when a deeper understanding of Landau damping is sought.

- **Collisions:** Landau damping is a collisionless effect. The condition of negligible collisionality can be generally achieved by assuming high temperature plasma and high frequency oscillations. However, collisions might also play an important role, as argued in Ref. [15], for example in the transition from the linear to the non linear damping regime. In general, the linear Landau damping can be justified over short time scales, such that the particles do not complete full cycles in phase space ($\gamma\tau_{osc} \gtrsim 1$). But if the collision rate is rapid

enough, so that $\nu_{coll}\tau_{osc} \gtrapprox 1$, particles do not complete full cycles because of collisions and the system is kept in the linear regime. More detailed discussions in Ref. [15] and [18].

- **Validity of the linearization:** in Sec. 1.2.3 we illustrated how the transition from linear to non-linear damping occurs for the case of a simple model assuming lightly damped solutions. For the VP system of Eqs. (1.1) and (1.2), the validity of the linearization, consisting in setting the term $E\partial f_{e,1}/\partial v$ to 0, is a thornier issue. Backus [19] was the first one to raise the issue and provided an upper time limit after which the non-linear effect may arise. However, Villani demonstrated that Landau damping can survive non-linearly, and the long time behaviour of the LVP system can be a good approximation of the long-time behavior of the (non-linear) VP system [14].

- **Initial conditions and non-Landau solutions:** in his original paper [9], Landau showed that, under specific analyticity assumptions on the initial condition $f_1(t = 0)$, the electric field always undergoes damping.[11] The validity of the assumption is debatable and non-Landau solutions arising when considering different $f_1(t = 0)$ have been numerically shown in Ref. [20].

- **Role of charge:** evidence was provided, both experimentally [21] and theoretically [22], that Landau damping is not a pure plasma phenomenon, but a phenomenon that can occur in all gases. The physical mechanism behind Landau damping was shown to be independent of charge, and the conventional picture of Landau damping, involving the resonant conversion of wave energy into particle kinetic energy by electrostatic interaction, has been questioned. An alternative picture based on thermal spread and phase mixing, valid for both plasmas and neutral gases, was suggested by Stubbe in Ref. [16].

- **N-body mechanics:** Landau damping is a typical kinetic effect, that emerges by describing the plasma system by means of an almost everywhere continuous distribution function. However, Escandé showed that the linear damping effect can be recovered through a discrete N-body system description [23]. The fundamental role played by resonant particles is reaffirmed.

- **Non-Maxwellian distributions $f_0(v)$:** Landau limited his consideration to a Maxwellian equilibrium distribution function $f_0(v)$. Unfortunately, physics provides several examples where the equilibrium distribution function is not Maxwellian: for instance, κ distributions and distributions with compact velocity support, such as Slowing-Down and relativistic distributions. How Landau damping is influenced by these kind of distribution functions will be the central topic of the present thesis.

1.3 Part I Outline

In the current study, our primary emphasis lies on the final aspect discussed in the preceding section: Non-Maxwellian distributions and specifically compact support distribution functions. In Chapter 4 we will provide a comprehensive examination of compact support distribution functions, initially in general terms and then specifically focusing on the Slowing-Down case. The examination will include a novel approach to treating such distributions using sigmoid functions.

The framework of this novel approach is based on Landau's treatment of the LVP system. Therefore, on our path towards Chapter 4, we first present Landau's approach to the LVP system

[11] if f_0 is a Maxwellian distribution function.

and analyse the general properties of the system solutions (Chapter 2). This will comprise a discussion about the multiplicity of solutions.

To detail and exemplify such discussion about the number of solutions we consider two specific examples, κ distributions and Maxwellians (Chapter 3), that lead us to an analytical expressions for the Maxwellian multiple structure and a suggestion for a possible connection between Landau damping and particle correlation.

Chapter 2

Landau's Approach to the Linear Vlasov-Poisson System

In the present chapter we explore the Landau's approach to the linear Vlasov-Poisson (LVP) system. In Sec. 2.1 the concept of Landau integral is explained and the expression for the LVP dispersion relation is derived. In Sec. 2.2 the main properties of the solutions to the dispersion relation are then described. We follow closely Refs. [9] and [15] up to the last paragraph about damped solutions, where we introduce a general discussion about the number of solutions.

2.1 Landau's Original Derivation

The starting point of Landau's original derivation [9] is the Vlasov-Poisson system of Eqs. (1.1) and (1.2). By neglecting the term $\frac{e}{m_e}E\frac{\partial f_{e,1}}{\partial v}$ in Eq. (1.1),[1] we obtain the linear Vlasov-Poisson (LVP) system:

$$\frac{\partial f_{e,1}}{\partial t} + v\frac{\partial f_{e,1}}{\partial x} - \frac{e}{m_e}E\frac{\partial f_{e,0}}{\partial v} = 0, \tag{2.1}$$

$$\frac{\partial E}{\partial x} = -\frac{e}{\epsilon_0}\int \mathrm{d}v f_{e,1}. \tag{2.2}$$

According to Landau, the correct approach to solving the LVP system involves using a Fourier transform in the spatial domain and a Laplace transform in the time domain. The Laplace transform is the natural choice when one realizes that the double Fourier transform (applied by Vlasov in his original treatment of the problem [8]) leads to the ill-defined dispersion relation

$$\epsilon(\omega, k) = 1 + \frac{e^2}{k\epsilon_0 m_e}\int_{-\infty}^{\infty}\frac{\partial f_{e,0}(v)/\partial v}{\omega - kv}\mathrm{d}v = 0, \tag{2.3}$$

where the issue is raised by the integral divergence due to the $1/(\omega - kv)$ term.

At first glance, a way to fix this may consist in replacing the real variable $\omega \in \mathbb{R}$ with the complex variable $p \in \mathbb{C}$. Besides hinting at damped/unstable solutions, substituting ω with p induces a natural redefinition of the Fourier transform,

$$\mathscr{F}\{g(t)\}(\omega) = \int_{-\infty}^{\infty} e^{-i\omega t}g(t)\mathrm{d}t \to \int_{-\infty}^{\infty} e^{-ipt}g(t)\mathrm{d}t \to \mathscr{L}\{g(t)\}(ip) = \int_{0}^{\infty} e^{-ipt}g(t)\mathrm{d}t, \tag{2.4}$$

[1] For damped solutions (Landau damping) the linearization can be justified with the results from Ref. [14], as commented on in Sec. 1.2.4. Alternatively, we can follow Ref. [24] and set $|\gamma\tau_{osc}| \gg 1$ as the condition for the linearization, where γ is the damping coefficient and $\tau = \sqrt{m_e/(ekE)}$. For stable and unstable solutions ($\gamma \geq 0$) we simply assume that a time interval for which $|\partial f_{e,1}/\partial v| \ll |\partial f_{e,0}/\partial v|$ exists.

that corresponds to the Laplace transform (the integration domain reduction to $[0, \infty]$ improves the convergence properties of this 'complex Fourier transform').

Despite being well defined when $\Im(p) \neq 0$, the dielectric tensor $\epsilon(p, k)$ remains discontinuous when $\Im(p) \to 0^{\pm}$ (consider for instance $f_0 = 1/(1 + v^2)$) and undefined on the real axis $\Im(p) = 0$. However, as we are going to discuss below, the Laplace transform and the associated integration techniques are the key to properly redefine $\epsilon(\omega, k)$ and to solve the LVP problem in a mathematically consistent manner.

Let's then start off by applying a space Fourier transform and a time Laplace transform to Eqs. (2.1) and 1.2 [2]:

$$-\tilde{f}_{e,1}(t = 0, k, v) - ip\tilde{f}_{e,1}(p, k, v) + ikv\tilde{f}_{e,1}(k, p, v) - \frac{e}{m_e}\tilde{E}(p, k)\frac{\partial f_{e,0}}{\partial v} = 0, \tag{2.5}$$

$$ik\tilde{E}(p, k) = -\frac{e}{\epsilon_0}\int_{-\infty}^{\infty} \tilde{f}_{e,1}(k, p, v)\mathrm{d}v. \tag{2.6}$$

Rearranging Eq. (2.5) yields

$$(ip - ikv)\tilde{f}_{e,1}(p, k, v) = \frac{e}{m_e}\tilde{E}(p, k)\frac{\partial f_{e,0}(v)}{\partial v} - \tilde{f}_{e,1}(t = 0, k, v). \tag{2.7}$$

When $\Im p \neq 0$ Eq. (2.7) can be divided by $p - kv$, and the final expressions for $\tilde{E}(p, k)$ and $E(t, k)$ are obtained by inserting Eq. (2.7) into Eq. (2.6),

$$\tilde{E}(p, k) = \frac{\frac{e}{k\epsilon_0}\int_{-\infty}^{\infty}\frac{\tilde{f}_{e,1}(t=0,k,v)}{p-kv}\mathrm{d}v}{1 + \frac{e^2}{k\epsilon_0 m_e}\int_{-\infty}^{\infty}\frac{\partial f_{e,0}(v)/\partial v}{p-kv}\mathrm{d}v}, \quad \Im(p) \neq 0, \tag{2.8}$$

$$E(t, k) = \frac{1}{2\pi}\int_{i\sigma-\infty}^{i\sigma+\infty} e^{-ipt}\left[\frac{\frac{e}{k\epsilon_0}\int_{-\infty}^{\infty}\frac{\tilde{f}_{e,1}(t=0,k,v)}{p-kv}\mathrm{d}v}{\epsilon(p, k)}\right]dp. \tag{2.9}$$

Eq. (2.9) corresponds to the Laplace inversion formula and involves a complex integral over the horizontal line $p = i\sigma + t$ ($t \in [-\infty, \infty]$). By combining $\Im p \neq 0$ and the Laplace transform requirement that prescribes that the inversion integral contour must lay above all the singularities p_n of $\tilde{E}(p)$ (see Fig. 2.1), we obtain that σ is a real number such that $\sigma > \mathrm{Max}_n\{0, \Im(p_n)\}$.

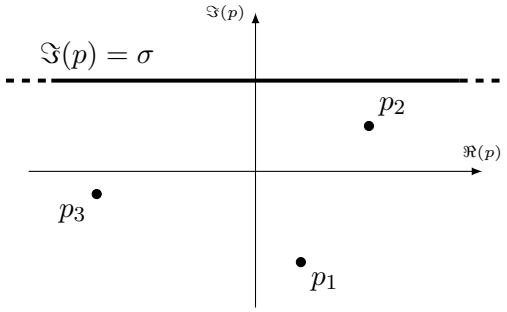

Figure 2.1: Contour for the inverse Laplace transform.

To get more insights on the solution and to facilitate potential numerical implementation, we aim at exploiting the residue theorem to express the electric field as a sum of wave modes. In

[2] *A priori* the LVP problem might have solutions which grow too rapidly to admit Laplace transform in time. The existence and uniqueness theorem for the initial value problem, proved in Ref. [19], excludes such pathological solutions.

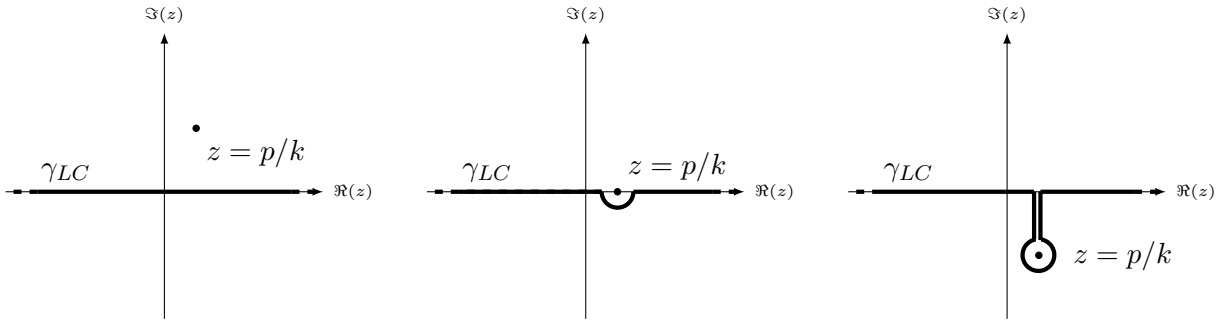

Figure 2.2: Illustration of the Landau contour. **Left** - $\Im(p/k) > 0$; **Center** - $\Im(p/k) = 0$; **Right** - $\Im(p/k) < 0$.

particular, complex analysis is used to analytically extend the integrand function of Eq. (2.9). The analytical continuation, by overcoming the issues of $\tilde{E}(p,k)$ (discontinuous when $\Im(p) \to 0$ and undefined on the real axis), is what allows the application of the residue theorem to Eq. (2.9) across the whole complex plane.

To explain the Landau analytical continuation, let's consider the function

$$F(p/k) = \int_C \frac{g(z)}{z - p/k} \mathrm{d}z, \tag{2.10}$$

defined as an integral on a generic contour C in the complex plane, with $g(z)$ as an entire function of z. The residue theorem states that the integral on a contour closed around a simple pole $z = p/k$ is equal to the residue of the integrand at the pole, namely

$$F_{closed}(p/k) = 2\pi i g(p/k). \tag{2.11}$$

We can then define a closed contour consisting of two sub-contours: a semicircle (SC) in the upper half plane (UHP) that lies above the pole and the Landau contour (LC), illustrated in Fig. 2.2. The definition is

$$F_{LC}(p/k) = \begin{cases} \int_{-\infty}^{\infty} \frac{g(v)}{v - p/k} \mathrm{d}v, & \Im(p/k) > 0, \\ \mathrm{P.V.} \int_{-\infty}^{\infty} \frac{g(v)}{v - p/k} \mathrm{d}v + \pi i g(p/k), & \Im(p/k) = 0, \\ \int_{-\infty}^{\infty} \frac{g(v)}{v - p/k} \mathrm{d}v + 2\pi i g(p/k), & \Im(p/k) < 0, \end{cases} \tag{2.12}$$

and we have

$$F_{LC}(p/k) = F_{SC}(p/k) + 2\pi i g(p/k). \tag{2.13}$$

Since the right hand side of Eq. (2.13) is an analytic function, it follows that the left hand side is also analytic. Hence, it has just been shown that given an entire function $g(z)$, the function

$$F(p/k) = \int_{-\infty}^{\infty} \frac{g(v)}{v - p/k} \mathrm{d}v, \tag{2.14}$$

which is analytic and well-defined in UHP ($\Im(p/k) > 0$), can be analytically extended throughout the entire complex plane by means of the definition provided in Eq. (2.12). Moreover, due to the general uniqueness property of analytical continuations, the defined continuation is also unique.

Returning to the integral of Eq. (2.9), under the assumption that $f_{e,1}(t=0,z)$ and $f_{e,0}(z)$ are entire functions, both the integrand numerator and denominator can be analytically extended across the whole complex plane. The redefined integrand, i.e.,

$$e^{-ipt}\frac{\frac{e}{k\epsilon_0}\int_{-\infty}^{\infty}\frac{\tilde{f}_{e,1}(t=0,k,v)}{p-kv}\mathrm{d}v}{1+\frac{e^2}{k\epsilon_0 m_e}\int_{-\infty}^{\infty}\frac{\partial f_{e,0}(v)/\partial v}{p-kv}\mathrm{d}v}, \tag{2.15}$$

is now a meromorphic function in the $p-$variable complex plane (i.e., its only singularities are poles). Consequently, the residue theorem can be applied on a contour comprising the aforementioned straight line $p = i\sigma + t$ and a semicircle with an infinite radius closing in the lower half plane (LHP). Since the contribution of the integral over the semicircle is zero, we can compute the integral as a sum of residues. Specifically, as both the integrand numerator and denominator are entire functions, the only singularities p_n correspond to the zeros of the integrand denominator $\epsilon(p,k)$[3] (also known as dielectric tensor),

$$2\pi E(t,k) = -2\pi i\sum_n \mathrm{Res}\left\{e^{-ip_n t}\tilde{E}(p_n,k)\right\},^4 \tag{2.16}$$

with $\epsilon(p,k)$ redefined as

$$\epsilon(p,k) = 1+\frac{e^2}{k\epsilon_0 m_e}\int_{LC}\frac{\partial f_{e,0}(v)/\partial v}{p-kv}\mathrm{d}v = 1-\frac{\omega_p^2}{k^2}\int_{LC}\frac{\partial f_0(v)/\partial v}{v-p/k}\mathrm{d}v, \tag{2.17}$$

with $f_{e,0}(v) = nf_0(v)$ and $\omega_p^2 = ne^2/m_e\epsilon_0$. By Taylor-expanding $\epsilon(p,k)$ around a pole p_n, for which $\epsilon(p_n,k)=0$,

$$\epsilon(p,k) = \epsilon(p_n,k)+\left.\frac{\partial\epsilon}{\partial p}\right|_{p_n}(p-p_n)+\mathcal{O}\{(p-p_n)^2\} = \left.\frac{\partial\epsilon}{\partial p}\right|_{p_n}(p-p_n)+\mathcal{O}\{(p-p_n)^2\}, \tag{2.18}$$

we can rewrite the solution $E(t,k)$ in its final form,

$$E(t,k) = 2\pi i\sum_n e^{-ip_n t}\frac{\frac{e}{k\epsilon_0}\int_{LC}\frac{\tilde{f}_{e,1}(t=0,k,v)}{p_n-kv}\mathrm{d}v}{\partial\epsilon/\partial p|_{p_n}}. \tag{2.19}$$

Final remarks regarding $f_{e,1}(t=0,z)$ and $f_{e,0}(z)$, as well as the assumptions made regarding their analyticity, are now in order. First of all, it is important to note that while these functions are originally defined as real variable functions $g(v\in\mathbb{R})$ — a definition sufficient for computing the integral in Eq. (2.9) — the $2\pi i g(z)$ term for the Landau continuation (Eq. (2.12)) requires their redefinition as complex variable functions. In the simplest scenario, this redefinition can be accomplished unambiguously by replacing the real variable $v\in\mathbb{R}$ with the complex variable $z\in\mathbb{C}$ (e.g., $e^{-v^2}\to e^{-z^2}$). However, there are some cases of physical significance (e.g., distribution function with compact velocity support) where the real variable function $f_{e,0}(v)$ is defined through the Heaviside function, and a unique complex redefinition cannot be established across the entire complex plane. These cases will be examined in detail in Chapter 4.

Returning to the simpler case of a unique complex variable definition, the original Landau's requirement regarding both $f_{e,1}(t=0,z)$ and $f_{e,0}(z)$ is their analyticity throughout the entire complex plane (i.e. entire functions). If the final solution is to be expressed as the sum of exponentials with frequencies exclusively given as roots of the dielectric tensor, the hypothesis for

[3]For the sake of simplicity, we assume that the numerator evaluated at p_n is never equal to zero

[4]the contour integral is clock-wise oriented, hence the minus sign

$f_{s,1}(t=0,z)$ cannot be abandoned. Abandoning this assumption would introduce singularities in the numerator of $\tilde{E}(p,k)$ due to the $2\pi i f_{e,1}(t=0,z)$ term in the analytical continuation. Consequently, the residue theorem would need to take these extra poles into account and Eq. (2.19) would have to be modified to take these poles into account. In the present work, we follow Landau and we will always keep $f_{s,1}(t=0,z)$ entire. For a discussion on 'non Landau solution' induced by disregarding this hypothesis, see Ref. [20].

On the other side, the hypothesis on $f_{e,0}(z)$ can be relaxed by requiring that the derivative $df_{e,0}(z)/\mathrm{d}z$ is meromorphic. As it will be shown in the next chapter, the singularities of $df_{e,0}(z)/\mathrm{d}z$, while not posing any issues for the residue theorem (an isolated singularity at the denominator of $\tilde{E}(p,k)$ translates to an analyticity point of $\tilde{E}(p,k)$ itself), are of significant importance. To some extent, they can be considered as the generators of the roots of the dielectric tensor. Notable examples of such meromorphic distributions include κ distributions $f_0(v/a) \propto (1+v/\kappa)^{-k-1}$, which find application especially in astrophysical plasmas.

Mathematically rigorous treatments of the LVP system can be found in Refs. [14] and [19]. These treatments examine the behaviour of the LVP solution as $t \to \infty$, under assumptions on $f_{e,1}(t=0,z)$ and $f_{e,0}(z)$ that are more general than Landau's original ones.

In the present work we specifically focus on relaxing Landau's assumption for $f_{e,0}(v)$. While the long time behavior — represented by the dispersion relation solution with the smallest damping — has been already addressed in the literature, our focus extends to the whole interval $t \in [0,\infty]$. To achieve this, we dive deeper into the complex plane, exploring the multiple solutions that the LVP system can generally admit.

2.2 General Properties of the Solutions

Let us summarize the key results from the previous section. Assuming that $\tilde{f}_{e,1}(t=0,k,v)$ is an entire function and $f_0(v)$ is meromorphic, we can express the electric field as follows:

$$E(t,k) = -2\pi i \sum_n e^{-ip_n t} A(p_n,k). \tag{2.20}$$

Here, the roots p_n are solutions to the dispersion relation, given by

$$\epsilon(p,k) = 1 - \frac{\omega_p^2}{k^2} Z\left(\frac{p}{k}, \frac{\partial f_0}{\partial v}\right) = 0, \tag{2.21}$$

where we introduce the generalized plasma dispersion function $Z(z,F)$ (GPDF),

$$Z(z,F) = \int_{LC} \frac{F(v)}{v-z}\mathrm{d}v = \begin{cases} \int_{-\infty}^{\infty} \frac{F(v)}{v-z}\mathrm{d}v, & \Im(z) > 0, \\ \mathrm{P.V.}\int_{-\infty}^{\infty} \frac{F(v)}{v-z}\mathrm{d}v + i\pi F(z), & \Im(z) = 0, \\ \int_{-\infty}^{\infty} \frac{F(v)}{v-z}\mathrm{d}v + 2i\pi F(z), & \Im(z) < 0, \end{cases} \tag{2.22}$$

and we notice that $Z(z,\partial f/\partial v) = dZ(z,f(v))/\mathrm{d}z$.

We now aim to examine the characteristics of the complex roots p_n, which we express as $p_n = \omega_n + i\gamma_n$. Here, ω_n and γ_n represent the oscillation frequency and the damping/growth rate, respectively.

Unstable Solutions, $\gamma > 0$

A straightforward derivation from Ref. [15] reveals that when the distribution function $f_0(v)$ has only one maximum at v_m, the system admits no unstable solutions ($\gamma > 0$). To show this,

let us consider the dispersion relation (Eq. (2.21)) in the UHP, with $z = p/k$,

$$k^2 = \omega_p^2 \int_{-\infty}^{\infty} \frac{\partial f_0/\partial v}{v - z} \mathrm{d}v, \tag{2.23}$$

and let us rationalize it by expressing $z = z_r + iz_i$,

$$k^2 = \omega_p^2 \int_{-\infty}^{\infty} \frac{\partial f_0/\partial v}{(v - z_r)^2 + z_i^2} (v - z_r) \mathrm{d}v + i2\pi\omega_p^2 \int_{-\infty}^{\infty} \frac{\partial f_0/\partial v}{(v - z_r)^2 + z_i^2} z_i \mathrm{d}v. \tag{2.24}$$

By summing the real part of Eq. (2.24) to the imaginary part of the same equation multiplied by $(z_r - v_m)/z_i$, we arrive at

$$k^2 = \omega_p^2 \int_{-\infty}^{\infty} \frac{\partial f_0/\partial v}{(v - z_r)^2 + z_i^2} (v - v_m) \mathrm{d}v. \tag{2.25}$$

Crucially, Eq. (2.25) cannot be positive because of the product $(v - v_m)\partial f_0/\partial v$ being non-positive. It is important to note that the converse is generally not true, meaning that there exist stable distribution functions ($\gamma_n \leq 0, \forall n$) that possess more than one maximum. For further details on the stability of solutions in the context of the LVP problem, refer to Stix and to the Penrose criterion. In our discussion, our primary focus will be on distributions that exclusively admit stable or damped modes ($\gamma \leq 0$). In cases of growing modes, we only note that the linear model assumption will eventually break down, giving way to nonlinear effects (e.g, saturation).

Stable and Undamped Solutions, $\gamma = 0$

Let us now turn our attention to the dispersion relation along the real axis, where $z_i = 0$, and seek out stable oscillations. In this scenario, the dispersion relation takes the form

$$k^2 = \omega_p^2 \, \mathrm{P.V.} \int_{-\infty}^{\infty} \frac{\partial f_0(v)/\partial v}{v - z_r} \mathrm{d}v + i\pi\omega_p^2 \frac{\partial f_0}{\partial v}(z_r). \tag{2.26}$$

A necessary condition for this relation to hold is that $\frac{\partial f_0}{\partial v}(z_r) = 0$. To fulfill this requirement, the distribution function $f_0(v)$ must admit one or more stationary points, where $\frac{\partial f_0}{\partial v}(v) = 0$. Given our assumption of meromorphicity for f_0, stationary points can only be isolated (i.e, no other stationary points are present in an arbitrarily small neighbourhood). In general, for a point v_m with $\frac{\partial f_0}{\partial v}(v_m) = 0$, setting $z_r = v_m$ directly yields $\omega_m = k_m v_m$, where k_m is determined by setting the real part of Eq. (2.26) to zero:

$$k_m^2 = \omega_p^2 \, \mathrm{P.V.} \int_{-\infty}^{\infty} \frac{\partial f_0(v)/\partial v}{v - v_m} \mathrm{d}v. \tag{2.27}$$

In our specific case of interest, namely distribution functions with a single maximum, $v_m = 0$ is the only stationary point, and we quickly recognize that no solutions are admitted. This is because the right-hand side of Eq. (2.27) results negative in this specific case.

Another way to obtain stable solutions consists in relaxing the assumption regarding the analyticity of f_0. We will consider this case in more detail in Chapter 4.

Solutions in the Limit $k \to 0$

The solutions to the LVP problem in the limit of small k are discussed and derived in basically every elementary treatment of Landau damping (e.g., [6]). Here, we only recall the final results.

In particular, for a generic meromorphic function, the following solution emerges in the limit of small k and under the assumption of small damping $|\gamma| \ll \omega$,

$$\omega^2 = \omega_p^2 \left(1 + 3k^2\lambda_D^2\right), \tag{2.28a}$$

$$\gamma = \frac{\pi}{2}\frac{\omega^3}{k^2}\frac{\partial f_0}{\partial v}\bigg|_{v=\omega/k}. \tag{2.28b}$$

A few observations are now appropriate. Firstly, the conventional interpretation of Landau damping in terms of the derivative $\partial f_0(v)/\partial v$ is quickly gained from Eq. (2.28b). When the derivative is negative, there are more particles gaining energy than particles losing it, the distribution gains energy, and the wave is damped. Conversely, when the derivative is positive, there are fewer particles gaining energy than particles losing it, the distribution loses energy and the wave grows.

Furthermore, under a zero-order approximation, we recover plasma oscillations with frequency $\omega^2 = \omega_p^2$. The physical interpretation remains straightforward by examining the phase space diagram of Fig. 1.3. As k approaches zero, particle orbits get flatter, resulting in smaller changes in velocity (δv) over the same spatial displacement (δx). Consequently, less energy is transferred between particles. In the limit, particles follow straight trajectories with no energy transfer, leading to stable E oscillations without damping. To this end, notice the dependency of γ on k through $\partial f_0(v)/\partial v$ evaluated at ω/k, which exerts a stronger influence compared to the quadratic k^2 dependence. This is why γ generally decreases with decreasing k.

Damped Solutions, $\gamma < 0$

We have shown that all solutions $p_n = \omega_n + i\gamma_n$ of the dispersion relation (2.21), assuming an entire or meromorphic distribution function with a single maximum, reside in the half plane $\gamma < 0$. In other words, the electric field amplitude decreases in time at a rate determined by $\{\gamma_n\}$, exhibiting damping. Here, we delve into the behavior of the dispersion relation in the lower-half-plane (LHP),

$$k^2 = \omega_p^2 \int_{-\infty}^{\infty} \frac{\partial f_0(v)/\partial v}{v - z}\mathrm{d}v + 2i\pi\omega_p^2 \frac{\partial f_0}{\partial v}(z), \tag{2.29}$$

and provide some general insights into the number of solutions.

We start off by examining the dispersion relation Eq. (2.29) in the limit $k \to \infty$. In this limit, we can neglect the integral term, since it is a bounded function of z. This allows us to rewrite Eq. (2.22) as[5]

$$\frac{k^2}{\omega_p^2} = Z(z, f'(z)) \approx 2i\pi f_0'(z). \tag{2.30}$$

As k can be arbitrarily large, the previous equality can be satisfied only if $Z(z, f'(z))$ can also be made arbitrarily large. In other words, z must belong to a sufficiently small neighborhood of a singularity point of $f_0'(z)$. Let us then assume that z belongs to such a small neighborhood of z_0, a singularity point of order n in the LHP. By representing $z - z_0$ as $Re^{i\theta}$, we can approximate $f_0'(z)$ as

$$f_0'(z) \approx \frac{C(z_0)e^{i\alpha(z_0)}}{R^n e^{in\theta}}, \tag{2.31}$$

where $A(z_0)e^{i\alpha(z_0)}$ is the expansion coefficient of the Laurent series term of order n. We can then decompose the right-hand side of Eq. (2.30) into its real and imaginary parts,

$$k^2 = \frac{\omega_p^2 2\pi C(z_0)}{R^n}\left[-\sin(\alpha - n\theta) + i\cos(\alpha - n\theta)\right] = A + iB. \tag{2.32}$$

[5]To improve clarity of notation, we denote the analytical continuation of $\partial f_0(v)/\partial v$ as $f_0'(z)$.

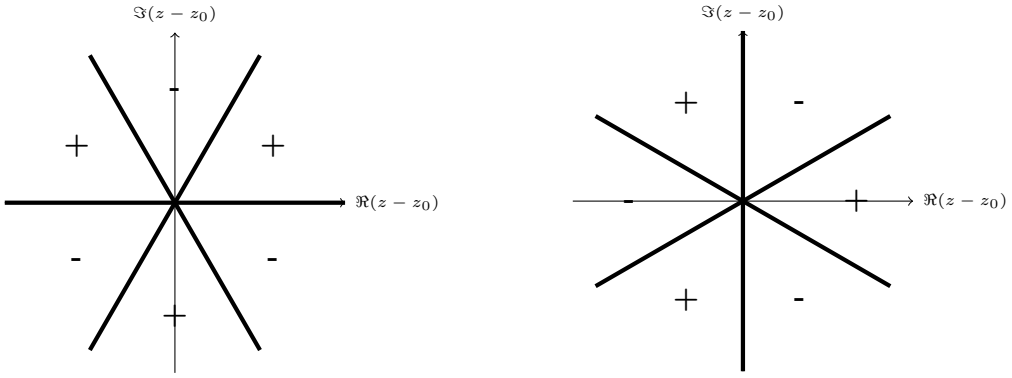

Figure 2.3: Inequalities for right-hand side of Eq. (2.32). **Left** - Real part, A; **Right** - Imaginary part, B. z_0 is a singularity point of order $n = 3$, α is set to zero.

and the following inequalities determine the signs of the real (A) and imaginary part (B) of the right-hand side of Eq. (2.32)

$$\begin{aligned} A > 0 &\iff \frac{\alpha}{n} + \frac{2\pi m}{n} < \theta < \frac{\alpha + \pi}{n} + \frac{2\pi m}{n}, \\ B > 0 &\iff \frac{\alpha - \pi/2}{n} + \frac{2\pi m}{n} < \theta < \frac{\alpha + \pi/2}{n} + \frac{2\pi m}{n}. \end{aligned} \tag{2.33}$$

Both the real and imaginary parts of right-hand-side of Eq. (2.32) are then characterized, around a singularity, by $2n$ regions of opposite sign (Fig. 2.3). The solutions are determined by the intersection of the curves $B = 0$ and $A = k^2$. In the next section we will observe how the curves $B = 0$ are straight lines, while the curves $A = k^2$ are lobe shaped. We expect a solution for each of the regions with positive real part, resulting in a total of n solutions, corresponding to the order of the singularity. In the approximation of large k, we get

$$\begin{cases} k^2 = \frac{\pi\omega_p^2 C}{R^n} \to R_n = \sqrt[n]{\frac{\pi\omega_p^2 C}{k^2}}, \\ 2m\pi = \frac{\pi}{2} + \alpha - n\theta \to \theta_{n,m} = -\frac{2m\pi}{n} + \frac{\pi/2+\alpha}{n}, \end{cases} \tag{2.34}$$

so that, for a given n, the approximate solutions z_n can be expressed as $z_0 + R_n e^{i\theta_{n,m}}$. The periodicity of the term $\frac{2m\pi}{n}$ sets to n the number of solutions, corresponding to the order of the considered singularity of $f_0'(z)$. We then conclude that, as $k \to \infty$, each singularity z_s in the LHP, of order n_s, is generating n_s roots p_s of the dispersion relation from Eq. (2.21). Moreover, such set of poles is distributed symmetrically around the discontinuity.

As k decreases, we expect that the contribution of the integral term to $Z(z, f')$ becomes less and less negligible, and that the symmetry observed previously gets lost. Specifically, we expect that the asymmetry will mainly affect $Z(z, f')$ at low $\Im z$ values (i.e., large damping), where the integral contribution is larger, and that in the limit $k \to 0$ the $k^2/\omega_p^2 = \Re Z$ and the $\Im Z = 0$ curves flatten along the real axis, so that the $\omega = \pm\omega_p$ solution is retrieved.

In the next chapter, we will adopt two distribution functions, Maxwellian and κ distributions, to verify the properties of the present section.

In conclusion, let us mention that, according to Eq. (2.19), the long-time evolution of the electric field $E(t)$ is dominated by the pole with the highest value of γ. Consequently, additional poles would be needed only when a more accurate description of the electric field is desired at short times. One could thus argue that studying such multi-pole structures is of scarce importance. Nevertheless, for reasons that will become clear later, we find a discussion about such strongly damped modes interesting and worthy of consideration.

Chapter 3

Maxwellian and κ Distributions

We test and illustrate the properties described in the previous chapter for two classes of distribution functions, κs (Sec. 3.1) and Maxwellians (Sec. 3.2). In subsection 3.2.1 we propose an analytical formula for the description of the Maxwellian multi-poles structure. In Sec. 3.3 we show how the Maxwellian structure of solutions arises from the structure of κ distributions in the limit $\kappa \to \infty$. In the same section we also indicate a possible new line of investigation, based on particle correlation, to extract a deeper physical meaning from Landau damping.

3.0.1 Variables Renormalization

Before delving into the core of this section, we normalize variables in order to work with dimensionless quantities. It is natural to use the plasma frequency $\omega_p = \sqrt{ne^2/\epsilon_0 m}$ to normalize the complex frequency p. Furthermore, since the distribution functions are generally defined in terms of some characteristic velocity v_t, we define $\lambda_D = v_t/(\sqrt{2}\omega_p)$ as the length scale for normalizing the wave vector k. So, we set

$$p' = \frac{p}{\omega_p}; \quad k' = k\lambda_D; \quad z' = \frac{p'}{k'} = \frac{\sqrt{2}}{v_t}\frac{p}{k}, \tag{3.1}$$

and the dielectric tensor, orginally expressed as $\epsilon(p,k) = 1 - \omega_p^2/k^2 Z(z, f')$, can be rewritten as

$$\epsilon(p',k') = 1 - \frac{v_t^2}{2k'^2}\int_{LC} \frac{\partial f_0/\partial v}{v - \frac{v_t}{\sqrt{2}}\frac{p'}{k'}}\mathrm{d}v. \tag{3.2}$$

In the upcoming sections, we will mainly solve and visualize $\epsilon(p',k')$ by keeping k' fixed, and by representing it as a function of z,

$$\epsilon_{k'}(z) = 1 - \frac{v_t^2}{2k'^2}\int_{LC} \frac{\partial f_0/\partial v}{v - z}\mathrm{d}v. \tag{3.3}$$

3.1 κ Distributions

Our first test case focuses on κ distributions, defined by

$$f_\kappa(v) = A_\kappa \left(1 + \frac{v^2}{\kappa v_t^2}\right)^{-\kappa}, \tag{3.4}$$

with A_κ given as

$$A_\kappa = \frac{1}{v_t}\frac{1}{\sqrt{\pi\kappa}}\frac{\Gamma(\kappa)}{\Gamma(\kappa - 1/2)}. \tag{3.5}$$

Here, v_t is a generic characteristic velocity, and $\kappa \in \mathbb{N}$ is the distribution parameter.

κ distributions are crucial for interpreting certain experimental results in plasma astrophysics, especially when describing high-energy particle populations with non-Maxwellian tails. They usually manifest themselves when the timescales of the phenomenon under study are shorter than those of binary collisions, such as in low-density plasmas or the interstellar medium. As collision frequencies increase, particle-particle correlation is destroyed and κ distributions converge toward a Maxwellian distribution. We refer to Ref. [25] for an extensive and in-depth examination of κ distributions.

From the definition (3.4), we can calculate the derivative $f'_\kappa(v)$,

$$f'_\kappa(v) = 2A_\kappa \frac{2}{\kappa v_t^2}(1 + \frac{v^2}{\kappa v_t^2})^{-\kappa-1}, \tag{3.6}$$

and we can define the GPDF, $Z(z, f)$, and its derivative, for κ distributions as:

$$Z_\kappa(z) = Z(z, f_\kappa(v)), \quad Z'_\kappa(z) = Z(z, f'_\kappa(v)). \tag{3.7}$$

$Z'_\kappa(z)$ can be computed analytically for each integer value of κ. For example, for $\kappa = 1$ we have

$$Z'_\kappa(z) = \frac{1}{(z + iv_t)^2}. \tag{3.8}$$

However, no general formula for varying values of κ exists, and analytical expressions become impractically long as κ increases. Consequently, we will resort to the one-solve-all numerical scheme of Xie [5], that allows to compute $Z(z, f)$ for any distribution function f. Detailed explanations of this numerical scheme will be offered in chapter 5.

In Figs. 3.1 and 3.3, the real and imaginary part of $Z'_{\kappa=2}$ are shown at different wave vector k' values ($k' = 0.1, 10$).[1] In Figs. 3.2 and 3.4, we show the absolute value of the dielectric tensor

$$\epsilon_{k'}(z) = 1 - \frac{v_t^2}{2k'} Z'_\kappa(z, f'), \tag{3.9}$$

and the approximated solutions given by Eq. (2.34).

Before inspecting the plots just mentioned, it is worth emphasizing how and why we typically plot, here and in the next chapter, the real (or imaginary) part of $Z(z, f')$ and the absolute value of the associated dielectric tensor $|\epsilon_{k'}(z)| = |1 - v_t^2 Z(z, f')/(2k')|$. First, we plot them by means of color-plots at fixed k', where the real axis corresponds to $\Re(z) = v_t\omega/(\sqrt{2}k')$, i.e., to the oscillation real frequency ω', and the imaginary axis corresponds to $\Im(z) = v_t\gamma'/(\sqrt{2}k')$, i.e., to the damping coefficient γ'. The magnitude of the plotted quantity is instead represented by the color. The importance of $|\epsilon_{k'}(z)| = |1 - v_t^2 Z(z, f')/(2k')|$ is that its zeros, showing up as blue spots, correspond to the roots of the dispersion relation (2.21), i.e., to the complex frequency solutions of the LVP problem. On the other hand, plotting $Z(z, f')$ is useful to illustrate how the roots are generated according to the discussion of the last paragraph of Sec. 2.2.

If we now focus on the aforementioned plots for κ distributions (Figs. 3.1, 3.2, 3.3, 3.4), the following key observations can be made:

- By examining Eq. (3.6), we note that f'_κ exhibits a single singularity in the LHP at $z_0 = -i\sqrt{\kappa v_t^2}$, and its order is $n = \kappa + 1$.

[1] Since $Z(z, f')$ does not explicitly depend on k', one might wonder why the plots vary at different k'. The reason is simply that the color range was modified in order to make the comparison to Fig. 2.3 more evident.

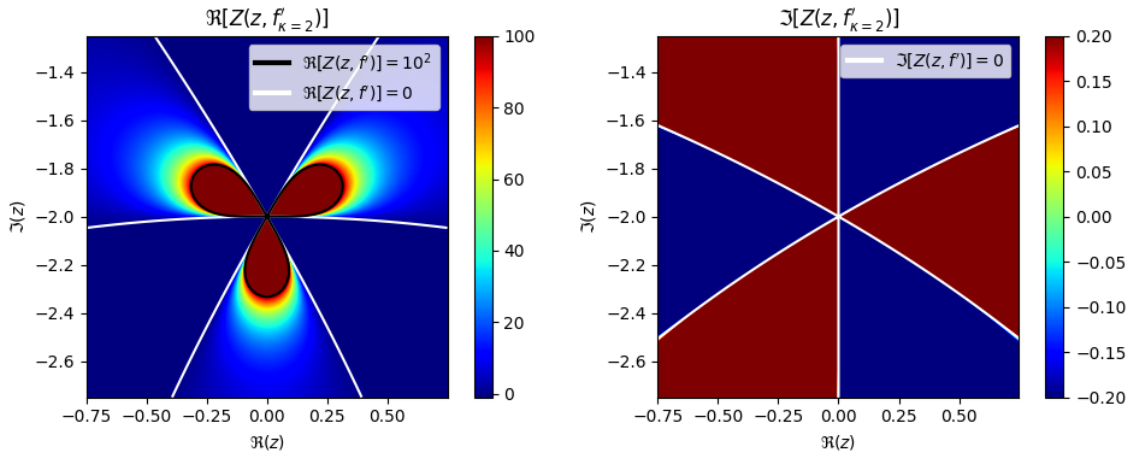

Figure 3.1: Real (**Left**) and imaginary (**Right**) part of $Z'_{\kappa=2}(z)$. The level curves $\Re(Z'_{\kappa=2}(z)) = \{0, 10^2\}$ and $\Im(Z'_{\kappa=2}(z)) = 0$ are also represented.

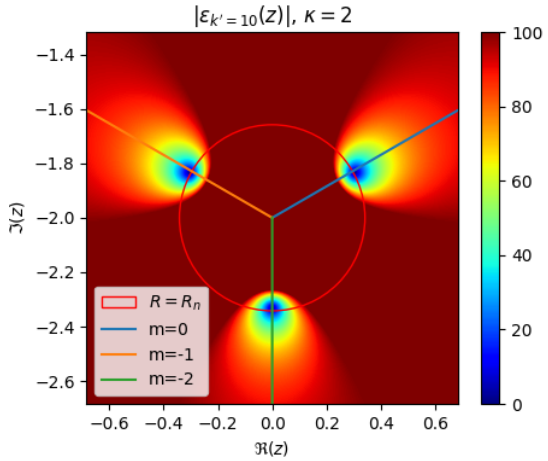

Figure 3.2: Absolute value of the dielectic tensor $\epsilon_{k'=10}(z) = 1 - Z'_{\kappa=2}(z)/k'^2$. The intersection between the red radius and the half-lines $m = i$ gives the approximate location of the poles according to Eq. (2.34).

- At large k' (Figs. 3.1 and 3.2), the symmetric structure predicted in Sec. 2.2 is confirmed. $2n$ regions with alternating sign appear in both the real and imaginary part of $Z'_{\kappa=2}$, and the $k + 1 = 3$ solutions are distributed symmetrically around z_0. The agreement between the zeros of $\epsilon_{k'}(z)$ and the analytical expressions for z_n in Eq. (2.34) is evident.
- At small k' (Figs. 3.3 and 3.4), the lobe-shaped curves $\Re[Z'_\kappa] = k'^2$ and the straight lines $\Im[Z'_\kappa] = 0$ lose the symmetric structure observed at large k'. In particular, as predicted, the curves at smaller $|\Im(z)|$ are more affected, and they become flatter along the real axis. The intersection of these 'real line' curves is responsible for the $\omega^2 = \omega_p^2$ solution as $k' \to 0$. The approximate solutions of Eq. (2.34) are clearly inaccurate.
- At intermediate k' values ($k' = 1$, shown later for different κ values in Fig. 3.7), the pole structure is intermediate between the highly symmetrical scenario for $k' \to \infty$ and the asymmetrical situation for $k' \to 0$.

It's worth noting that we have focused on integer values of κ. This choice is due to the complications arising when defining $f_\kappa(z)$ from $f_\kappa(v)$ when κ is real. This leads to non-isolated

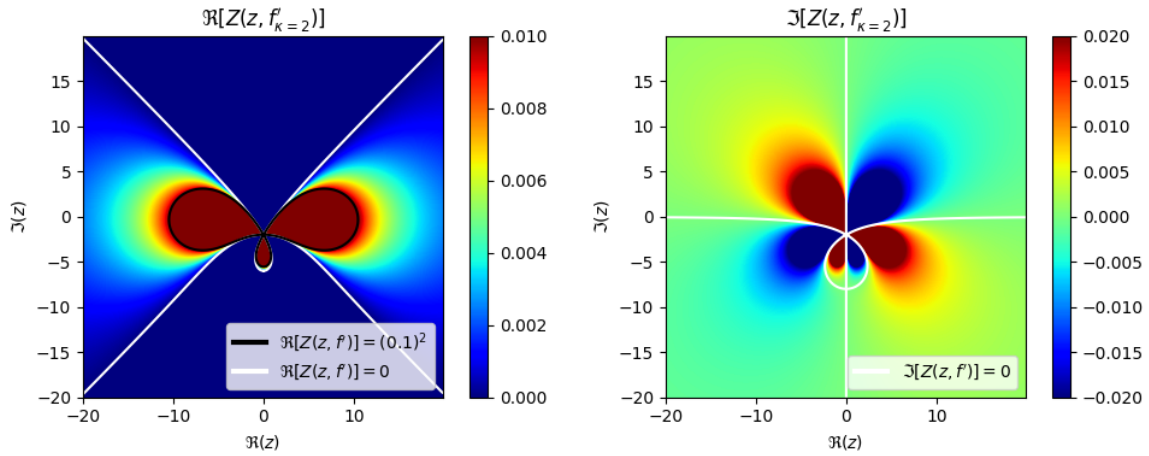

Figure 3.3: Real (**Left**) and imaginary (**Right**) part of $Z'_{\kappa=2}(z)$. The level curves $\Re(Z'_{\kappa=2}(z)) = \{0, 0.1^2\}$ and $\Im(Z'_{\kappa=2}(z)) = 0$ are also represented.

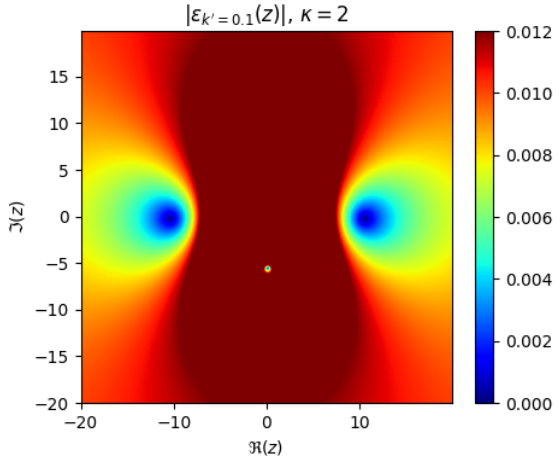

Figure 3.4: Absolute value of the dielectic tensor $\epsilon_{k'=0.1}(z) = 1 - Z'_{\kappa=2}(z)/k'^2$.

singularities, rendering $f_\kappa(z)$ non-meromorphic and precluding the application of the original Landau treatment. The following chapter will dive into the intricacies of this problem.

3.2 Maxwellian Distribution

The second test case examines the Maxwellian distribution function, which is the well-known equilibrium state for ideal gases and plasmas. It is defined as:

$$f_M(v) = \frac{1}{\sqrt{\pi v_t^2}} e^{-\frac{v^2}{v_t^2}}, \tag{3.10}$$

where v_t represents the thermal velocity. Analogous to the κ distribution case, we define the GPDF and its derivative for Maxwellian distribution functions as:

$$Z_M(z) = Z(z, f_M), \quad Z'_M(z) = Z(z, f'_M). \tag{3.11}$$

Despite not admitting analytical expressions, Z_M and Z'_M can be computed by exploiting the Faddeeva function,

$$Z_{Fad}(z) = e^{-z^2}\,\mathrm{erfc}(-iz) = \frac{v_t}{i\sqrt{\pi}} Z_M(v_t z), \tag{3.12}$$

$$Z'_{Fad}(z) = \frac{2i}{\sqrt{\pi}} - 2z Z_{Fad}(z) = \frac{v_t}{i\sqrt{\pi}} Z'_M(v_t z), \tag{3.13}$$

The availability of the Faddeeva function in standard libraries, such as SciPy in Python, makes it possible to calculate Z_M and Z'_M with a high degree of precision. The proof of $Z_{Fad}(z) = \frac{v_t}{i\sqrt{\pi}} Z_M(v_t z)$ is given in the appendix of the present chapter.

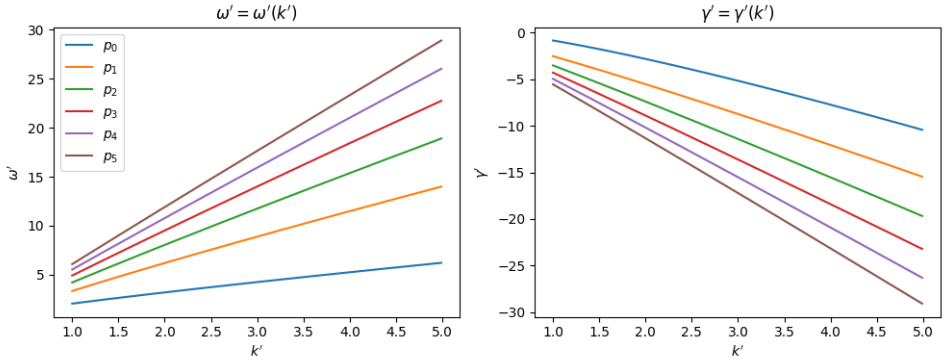

Figure 3.5: Dispersion relation $p' = p'(k')$ for the six Maxwellian poles with smallest damping.

In Fig. 3.6, the roots of the dispersion relation $\epsilon_{k'=1}(z) = 0$ are shown. In Fig. 3.5, the dependency $\omega = \omega(k)$ for the first six Maxwellian poles is displayed in the range $k' = [1, 5]$.

3.2.1 Maxwellian Multi-poles

In the limit of large wave numbers k, the pole structure for the Maxwellian distribution can be described analytically. Starting from the dispersion relation in the LHP in the limit of large k, we get

$$k^2 - \frac{v_t^2}{2}\int_{-\infty}^{\infty} \frac{F'_M(v)}{v - z} - v_t^2 \pi i F'_M(z) = 0 \rightarrow k^2 - v_t^2 \pi i F'_M(z) = 0. \tag{3.14}$$

Plugging in the Maxwellian distribution function yields

$$k^2 - v_t^2 \pi i \left[\frac{-2z}{\sqrt{\pi} v_t^3} e^{-z^2/v_t^2}\right] = 0 \rightarrow k^2 + 2i\sqrt{\pi}\frac{z}{v_t} e^{-z^2/v_t^2} = 0, \tag{3.15}$$

and by expressing z in polar form,

$$k^2 = -2i\sqrt{\pi}\frac{R e^{i\theta}}{v_t} \exp\left(-\frac{R^2\cos 2\theta}{v_t^2}\right) \exp\left(-i\frac{R^2 \sin 2\theta}{v_t^2}\right). \tag{3.16}$$

We calculate the absolute value and the phase of the last expression and we obtain a system of two equations in the unknown variables R and θ,

$$\begin{cases} k^2 = 2\sqrt{\pi}\frac{R}{v_t} \exp\left(-\frac{R^2\cos 2\theta}{v_t^2}\right), \\ 2\pi m = \frac{3\pi}{2} + \theta - \frac{R^2 \sin 2\theta}{v_t^2}. \end{cases} \tag{3.17}$$

In the limit of large R/v_t, the first equation of the system becomes

$$k^2 = 2\sqrt{\pi}\frac{R}{v_t}\exp\left(-\frac{R^2\cos 2\theta}{v_t^2}\right) \propto \delta(2\theta - \pi/2 - \pi n) \tag{3.18}$$

and implies that $\theta = \frac{\pi}{4} + \frac{\pi}{2}n$. As we are considering only the LHP, the solutions for θ are $\theta = \left\{-\frac{\pi}{4}, -\frac{3}{4}\pi\right\}$ (with $n = -1, -2$), and by substituting these values into the second equation of the system (3.17), we determine

$$2\pi m + \frac{3\pi}{4} = \frac{R^2}{v_t^2} \rightarrow \frac{R}{v_t} = \sqrt{\pm 2\pi m + \frac{3\pi}{4}}, \tag{3.19}$$

where the plus sign and minus sign correspond, respectively, to $\theta = -\frac{\pi}{4}$ and $\theta = -\frac{3}{4}$. It is clear that, due to the assumption of large R/v_t needed for Eq. (3.18), the solution for R/v_t becomes more accurate as m grows. The correctness of Eq. (3.19) in the limit $R \rightarrow \infty$ is depicted in Fig. 3.6.

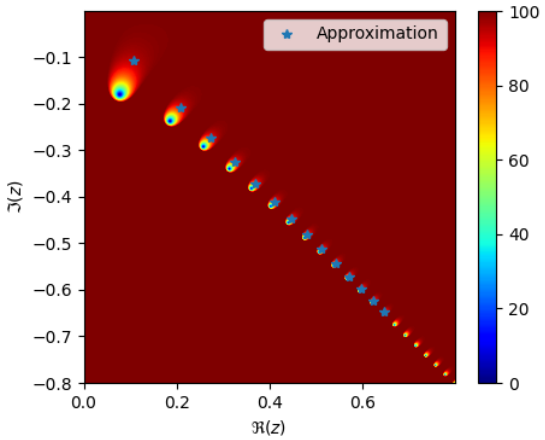

Figure 3.6: Maxwellian multi-poles: solutions of the dispersion relation $k'^2 - v_t^2 Z_M(z) = 0$, with thermal velocity $v_t = 0.1$, and wave vector $k' = 10$. The analytical expression of Eq. (3.19) is also represented.

3.3 From κ Distributions to Maxwellian Distributions

The typical feature of the Maxwellian case is that the dispersion relation admits an infinite number of roots. Previously, we observed that the mathematical origin of the multi-poles structure is related to the LHP singularities of $f_0'(z)$. According to this simple picture, the Maxwellian multi-poles can be straightforwardly explained by considering the limit

$$f_\kappa(z) = A_\kappa\left(1 + \frac{v^2}{\kappa v_t^2}\right)^{-\kappa} \xrightarrow{\kappa\rightarrow\infty} f_M = \frac{1}{\sqrt{\pi}v_t}e^{-v^2/v_t^2}. \tag{3.20}$$

With increasing κ, the number of roots for the dielectric tensor $1 - v_t^2 Z(z, f_\kappa')$ rises, the singularity moves deeper into the LHP. Additionally, an higher similarity with the Maxwellian distribution structures is spotted. Such a limit, depicted in Fig. 3.7 leads us to interpret the Maxwellian multi-poles as the $\kappa + 1$ poles arising from a κ distribution with $\kappa \rightarrow \infty$, with a single singularity at $z_0 = -i\sqrt{\kappa v_t^2}$, center of the lobe-shaped structure, shifted at $-i\infty$.

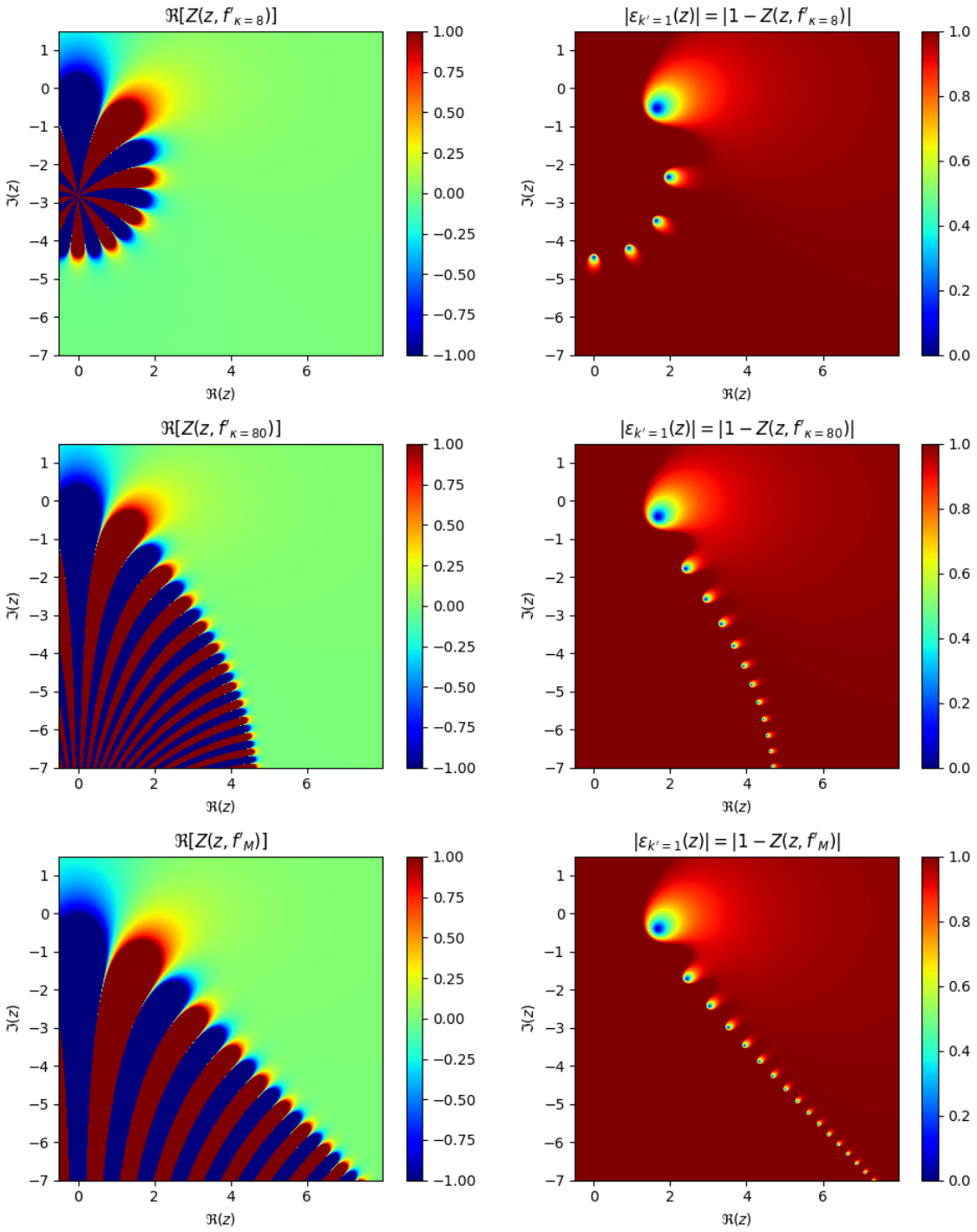

Figure 3.7: κ distributions approaching a Maxwellian: from top to bottom, real part of $Z(z, f')$ (**Left**) and absolute value of $\epsilon_{k'=1}(z) = 1 - Z(z, f')$ (**Right**), with $f = f_{\kappa=8}, f_{\kappa=80}, f_M$. $v_{th} = \sqrt{2}$ and $k' = 1$.

As we have already pointed out, it is evident that the multi-pole structure is of limited utility for the pure goal of describing the evolution of the electric field $E(t)$. Nonetheless, we believe that a deeper investigation of this structure may be valuable. Our belief stems from the following consideration.

As illustrated in Fig. 1, Kappa and Maxwellian feature a similar overall shape — the main

difference residing in the high-energy tails of κ distributions — but a different number of poles. It has been demonstrated in previous research ([26],[27]) that the κ parameter is related to the degree of correlation between particles in the κ distribution function. Specifically, the correlation decreases as κ grows, and it ultimately approaches zero as κ tends to the Maxwellian $\kappa \to \infty$ limit. Given that the number of poles corresponds to $\kappa + 1$, one might conjecture that the number of poles is linked to the level of correlation within the system. Such a hypothesis would imply:

- Distributions with stronger correlation may have fewer available poles, reflecting the reduced 'freedom of movement' of the system.
- Distributions with weaker correlation may exhibit more available modes (even approaching infinity in the Maxwellian limit $\kappa \to 0$), reflecting the enhanced 'freedom of movement'.

As appealing as these ideas may be, it is obvious that they require further investigation and, at this stage, they still represent a mere theoretical pondering. While the smallest damping solution for κ distribution has already been connected to the correlation property in the context of non-extensive statistics ([28] and [29]), the complete pole structure has never been described, as far as the author knows, in terms of correlation.

So far, we have only taken into account the scenarios with $f_0(v)$ being either meromorphic or entire. In the next chapter we will instead analyse distribution functions that are neither meromorphic nor entire and that pose a uniqueness issue in the LHP description.

Extra A: Proving $Z_{Fad}(z) = \frac{v_t}{i\sqrt{\pi}} Z_M(v_t z)$

We start by noticing that the function $M(z) = \frac{1}{\sqrt{\pi}} \int_{LC} \frac{e^{-t^2}}{t-z} \mathrm{d}t$, commonly known as plasma dispersion function [5], is related to $Z_M(z)$ through the identity

$$M(z) = \frac{1}{\sqrt{\pi}} \int_{LC} \frac{e^{-t^2}}{t-z} \mathrm{d}t = \frac{1}{\sqrt{\pi}} \int_{LC} \frac{e^{-v^2/v_t^2}}{v - v_t z} \mathrm{d}v = v_t \int_{LC} \frac{f_M(v)}{v - v_t z} \mathrm{d}v = v_t Z(v_t z, f_M), \tag{3.21}$$

that allows to rewrite $Z_{Fad}(z) = \frac{v_t}{i\sqrt{\pi}} Z_M(v_t z)$ in the simpler form:

$$Z_{Fad}(z) = \frac{1}{i\sqrt{\pi}} M(z). \tag{3.22}$$

- $\Im(z) > 0$:

$$\begin{aligned}
M(z) =& \frac{1}{\sqrt{\pi}} \int_{-\infty}^{\infty} \frac{e^{-v^2}}{v - z} \mathrm{d}v = \frac{-1}{\sqrt{\pi}} \int_{-\infty}^{\infty} e^{-v^2} \left[-2i \int_0^{\infty} e^{2i(z-v)t} \mathrm{d}t \right] \mathrm{d}v \\
=& \frac{2i}{\sqrt{\pi}} \int_0^{\infty} \left[\int_{-\infty}^{\infty} e^{-v^2} e^{2i(z-v)t} \mathrm{d}v \right] \mathrm{d}t = \frac{2i}{\sqrt{\pi}} \int_0^{\infty} e^{2izt} \left[\int_{-\infty}^{\infty} e^{-v^2 - 2ivt} \mathrm{d}v \right] \mathrm{d}t \\
=& \frac{2i}{\sqrt{\pi}} \int_0^{\infty} e^{2izt} \left[\int_{-\infty}^{\infty} e^{-(v+it)^2 - t^2} \mathrm{d}v \right] \mathrm{d}t = \frac{2i}{\sqrt{\pi}} \int_0^{\infty} e^{2izt - t^2} \left[\sqrt{\pi} \right] \mathrm{d}t \\
=& \frac{2}{i} \int_0^{\infty} e^{-(t-iz)^2 - z^2} \mathrm{d}t = 2i\, e^{-z^2} \int_0^{\infty} e^{-(t-iz)^2} \mathrm{d}t \\
=& 2i\, e^{-z^2} \int_{0-iz}^{\infty - iz} e^{-t^2} \mathrm{d}t \ \textit{(residue theorem)} \\
=& 2i\, e^{-z^2} \left[\int_0^{\infty} e^{-t^2} \mathrm{d}t + \int_{-iz}^{0} e^{-t^2} \mathrm{d}t \right] = 2i\, e^{-z^2} \left[\frac{\sqrt{\pi}}{2} \mathrm{d}t - \int_0^{-iz} e^{-t^2} \mathrm{d}t \right] \\
=& i\sqrt{\pi}\, e^{-z^2} \left[1 - \frac{2}{\sqrt{\pi}} \int_0^{-iz} e^{-t^2} \mathrm{d}t \right] = i\sqrt{\pi}\, e^{-z^2} \left[1 - \mathrm{erf}(-iz) \right] \\
=& i\sqrt{\pi}\, e^{-z^2} \left[1 + \mathrm{erf}(iz) \right] = i\sqrt{\pi}\, e^{-z^2} \, \mathrm{erfc}(-iz) \\
=& i\sqrt{\pi}\, Z_{Fad}(z).
\end{aligned} \tag{3.23}$$

- $\Im(z) < 0$:

$$\begin{aligned}
M(z) =& \frac{1}{\sqrt{\pi}} \int_{-\infty}^{\infty} \frac{e^{-v^2}}{v - z} \mathrm{d}v + 2i\sqrt{\pi}\, e^{-z^2} \\
=& \left[\frac{1}{\sqrt{\pi}} \int_{-\infty}^{\infty} \frac{e^{-v^2}}{v - z^*} \mathrm{d}v \right]^* + 2i\sqrt{\pi}\, e^{-z^2} \\
=& \left[i\sqrt{\pi}\, Z_{Fad}(z^*) \right]^* + 2i\sqrt{\pi}\, e^{-z^2} \\
=& - i\sqrt{\pi}\, Z_{Fad}(-z) + 2i\sqrt{\pi}\, e^{-z^2} \\
=& - i\sqrt{\pi} \left[-Z_{Fad}(z) + 2\, e^{-z^2} \right] + 2i\sqrt{\pi}\, e^{-z^2} \\
=& i\sqrt{\pi}\, Z_{Fad}(z),
\end{aligned} \tag{3.24}$$

where the property $[Z_{Fad}(z^*)]^* = Z_{Fad}(-z) = 2\, e^{-z^2} - Z_{Fad}(z)$ has been used.

- $\Im(z) = 0$:

$$
\begin{aligned}
M(z) =& \frac{1}{\sqrt{\pi}} PV \int_{-\infty}^{\infty} \frac{e^{-v^2}}{v-z} \mathrm{d}v + i\sqrt{\pi}\, e^{-z^2} \\
=& \frac{1}{\sqrt{\pi}} \lim_{\epsilon \to 0} \left[\int_{-\infty}^{z-\epsilon} \frac{e^{-v^2}}{v-z} \mathrm{d}v + \int_{z+\epsilon}^{\infty} \frac{e^{-v^2}}{v-z} \mathrm{d}v \right] + i\sqrt{\pi}\, e^{-z^2} \\
=& \frac{1}{2} \lim_{\epsilon \to 0} \left[\frac{1}{\sqrt{\pi}} \int_{-\infty+i\epsilon}^{\infty+i\epsilon} \frac{e^{-v^2}}{v-z} \mathrm{d}v + \frac{1}{\sqrt{\pi}} \int_{-\infty-i\epsilon}^{\infty-i\epsilon} \frac{e^{-v^2}}{v-z} \mathrm{d}v \right] + i\sqrt{\pi}\, e^{-z^2} \\
=& \frac{i\sqrt{\pi}}{2} \lim_{\epsilon \to 0} \left[Z_{Fad}(z+i\epsilon) + Z_{Fad}(z-i\epsilon) - 2\, e^{-z^2} \right] + i\sqrt{\pi}\, e^{-z^2} \\
=& i\sqrt{\pi}\, Z_{Fad}(z).
\end{aligned}
\tag{3.25}
$$

Chapter 4

Distribution Functions with Non-Unique Analytical Continuation

We now dive into a different class of distribution functions $f_0(v)$ whose complex plane definition $f_0(z)$ is ambiguous, posing a uniqueness issue within Landau's approach to the LVP system. After a brief introductory overview (Sec. 4.1), we first examine the general case of distribution functions with compact support, commonly referred to as cut-off distributions (Sec. 4.2). After presenting some general properties, previously discussed in Ref.[30], we confirm by means of a straightforward numerical integration the equivalence of various descriptions found in literature. In Sec. 4.3 a novel approach to address cut-off distributions is introduced. Specifically, we propose the application of a sigmoid function to smooth out the distribution. Sec. 4.4 focuses on the specific example of the Slowing-Down distribution and offers a possible definition for a 'smooth' Slowing-Down. Lastly, we shortly touch upon the case of κ distributions with non-integer κ (Sec.4.5).

4.1 Introduction

In Chapter 2 we introduced the generalized plasma dispersion function $Z(z, F)$ for the generic function $F(v)$. As per Eq. 2.22, the lower half-plane (LHP) definition involves the term $2\pi i F(z)$, that necessitates the redefinition of $F(v)$ as a complex variable function. In some cases this redefinition becomes problematic, for instance when the Heaviside step function $H(v)$ is part of the definition of $F(v)$. This problem is not a mere mathematical intricacy, but represents an interesting and actual problem in connection to common and useful distribution functions such as incomplete distributions, Slowing-Down, κ distributions with non-integer κ, and relativistic distributions.[1]

In the literature, these 'troublesome' distributions are acknowledged in various publications. Backus [19] sidesteps the lower half-plane definition by exclusively considering the long time limit. Twiss [31] and Godfrey [32] (in the relativistic setting), Weitzner [30] and Hudson [33] (for the classical LVP system) faced the $F(z)$ definition and realized that non-isolated discontinuities cannot be avoided. They then demonstrated that the electric field solution must include an additional slowly decaying contribution, obtained through integrals over contours surrounding the F(z) discontinuities. Although these references employ distinct techniques to define $F(z)$, and locate the discontinuities differently in the complex plane, the residue theorem ensures that the electric field solution does not depend on the specific description chosen. From a practical

[1] In the relativistic setting, the LVP has to be reformulated, but the problem under discussion is still present.

perspective the equivalence in terms of the electric field solution could potentially conclude the present chapter after the general properties of Sec. 4.2.

However, we find the multiplicity of possible LHP description puzzling: the unique electric field solution is associated to an infinity of possible mathematical definitions in the lower half plane. This chapter, therefore, stems from the attempt of understanding how distinct LHP descriptions arise. Beyond a generic quest for the 'deeper physical meaning' of LHP descriptions, the present investigation originates from a concrete physical ground, related to Energetic particle driven Geodesic Acoustic Modes (EGAMs). We will clarify how our discussion is related to EGAMs at the end of the next section.

4.2 Distribution Functions with Compact Support

In this section, we address the specific issue posed by distribution functions $f_0(v)$ with compact support, commonly referred to as cut-off distributions.[2] These distributions are formally defined as

$$f_0(v) = \begin{cases} F_0(v) & \text{if } |v| \leq v_c, \\ 0 & \text{otherwise,} \end{cases} \tag{4.1}$$

and they can be conveniently expressed in terms of the Heaviside function $H(v)$ as

$$f_0(v) = F_0(v) H_d(v, v_c) = F_0(v) \left[H(v + v_c) - H(v - v_c) \right]. \tag{4.2}$$

Here, we introduce $H_d(v, v_c)$ as the symmetric 'window' function, represented as the difference between two Heaviside functions. For the purposes of this chapter, we assume that $F_0(v)$ is a symmetric real-valued function with a single maximum and a unique definition in the lower half-plane. The derivative $f_0'(v)$ is then given by

$$f_0'(v) = F_0'(v) H_d(v, v_c) + F_0(v) \left[\delta(v + v_c) - \delta(v + v_c) \right]. \tag{4.3}$$

As the Heaviside function $H(v)$ cannot be extended analytically across the whole complex plane, defining the $2\pi i f'(z)$ term for $Z(z, f_0')$ turns out being troublesome, and the limitation of the original Landau's treatment for cut-off distributions becomes evident.

Cut-off distributions can be used to describe relativistic distributions, that do not admit velocity larger than the speed of light, and incomplete distributions.[3] The slowing-Down distribution can be considered as a cut-off distribution as well, but since the definition of $F_0(v)$ determines an additional difficulty in that case, it will be treated separately.

4.2.1 Upper Half-Plane

By considering the definition for the generalized plasma dispersion function $Z(z, f)$, we immediately realize that the UHP definition remains consistent with cut-off distributions. Plugging Eq. (4.3) into Eq. (2.22), we obtain

$$\begin{aligned} Z_{UHP}(z, f_0') &= \int_{-\infty}^{\infty} \frac{f_0'(v)}{v - z} \mathrm{d}v \\ &= \int_{-\infty}^{\infty} \frac{F_0'(v) H_d(v, v_c)}{v - z} \mathrm{d}v + F_0(v_c) \left[\frac{1}{-v_c - z} - \frac{1}{v_c - z} \right] \\ &= \int_{-v_c}^{v_c} \frac{F_0'(v)}{v - z} \mathrm{d}v + F_0(v_c) \frac{2v_c}{z^2 - v_c^2}, \end{aligned} \tag{4.4}$$

[4]

[2] For simplicity, we assume symmetric support $[-v_c, v_c]$. Asymmetric boundaries (and the case of one boundary set to infinity) do not substantially alter the analysis.

[3] Incomplete distributions are generally defined on a semi-open support, but as pointed out in the previous footnote this does not imply substantial differences.

and the dispersion relation in the UHP becomes

$$\frac{k^2}{\omega_p^2} = \int_{-v_c}^{v_c} \frac{F_0'(v)}{v-z}\mathrm{d}v + F_0(v_c)\frac{2v_c}{z^2-v_c^2}. \tag{4.5}$$

In cases where F_0 has a single maximum, we can apply similar arguments as in Sec. 2.2 to prove that the linear Vlasov-Poisson system does not admit unstable solutions with $\gamma > 0$ when the equilibrium distribution function $f_0(v)$ has compact support.

4.2.2 Real Axis

Along the real axis, the GPDF can be consistently defined as

$$Z_R(z, f_0') = \mathrm{P.V.}\int_{-v_c}^{v_c} \frac{F_0'(v)}{v-z}\mathrm{d}v + F_0(v_c)\frac{2v_c}{z^2-v_c^2} + \pi i F_0'(v) H_d(v, v_c). \tag{4.6}$$

The dispersion relation directly follows as:

$$\frac{k^2}{\omega_p^2} = \mathrm{P.V.}\int_{-v_c}^{v_c} \frac{F_0'(v)}{v-z}\mathrm{d}v + F_0(v_c)\frac{2v_c}{z^2-v_c^2} + \pi i F_0'(v) H_d(v, v_c), \tag{4.7}$$

As $H_d(v, v_c)$ only vanishes outside the interval $[-v_c, v_c]$, a stable solution $z_r = \omega_r/k_r$ exists only if $|z_r| > v_c$. In this case, Eq. (4.7) becomes

$$\frac{k^2}{\omega_p^2} = \int_{-v_c}^{v_c} \frac{F_0'(v)}{v-z_r}\mathrm{d}v + F_0(v_c)\frac{2v_c}{z_r^2-v_c^2} \tag{4.8}$$

If we define $Z(z_r)$ as the right-hand side of the previous equality, its derivative can be computed, showing that $Z(z_r)$ is monotonously decreasing (increasing) for $z_r > v_c$ ($z_r < v_c$). Consequently, we deduce that

$$Z(\pm\infty) = 0 < Z(z_r) < Z(v_c), \tag{4.9}$$

and a stable solution exists only for small values of k^2, satisfying

$$0 < k^2 < \omega_p^2 F(v_c) \tag{4.10}$$

In general, our focus is on cases where $F_0(v_c) \neq 0$, implying $F(v_c) = \infty$. In such cases, a stable solution will always exist for any value k.

Such a stable solution remains consistent with the interpretation that singularities generate solutions. In this case, the derivative singularity point $z = \pm v_c$ is responsible for the stable solution.

The physical interpretation is also straightforward: compact support implies that no particles at velocities larger than v_c are present. Hence, when the wave phase velocity is greater than v_c there is no resonating particle, and the wave propagates without damping.

The stable solution can be described analytically in both limits, as $k \to 0$ and $k \to \infty$. The former limit is the same as in Eq. (2.28a), while the latter is described by the following

calculation:[5]

$$\begin{aligned} k^2 &= \omega_p^2 \left[\int_{-v_c}^{v_c} \frac{F_0'(v)}{v-z} + F_0(v_c) \frac{2v_c}{z^2 - v_c^2} \right] \\ &\approx \omega_p^2 F_0(v_c) \frac{2v_c}{z^2 - v_c^2} \\ &\approx \omega_p^2 F_0(v_c) \frac{2v_c}{2v_c\epsilon} (1 - \frac{\epsilon}{2v_c}) \\ &\approx \omega_p^2 \frac{F_0(v_c)}{\epsilon}, \end{aligned} \tag{4.11}$$

Thus,

$$(\frac{\omega}{k} - v_c) = \omega_p^2 F_0(v_c)/k^2. \tag{4.12}$$

As the right hand-side of the last equality tends to 0 as $k \to \infty$, the left hand-side must vanish accordingly. Therefore, we conclude that in the limit $k \to \infty$, the electric field phase velocity ω/k approaches the cut-off velocity v_c.

4.2.3 Lower Half-Plane

In the LHP, the formal definition for cut-off distributions is

$$Z_{LHP}(z, f_0') = \int_{-\infty}^{\infty} \frac{F_0'(v) H_d(v, v_c)}{v - z} \mathrm{d}v + 2\pi i F_0'(z) H_d(z, v_c) + F_0(v_c) \frac{2v_c}{z^2 - v_c^2}. \tag{4.13}$$

While $F_0'(z)$ is generally well defined, $H_d(z - v_c)$ is not. Since there is no unique way to define $H_d(z, v_c)$, we examine three different possible definitions, among infinitely many, for the 'window' function:

$$\begin{aligned} H_{d,0}(z, v_c) &= 0, \\ H_{d,1}(z, v_c) &= H(v_c - |\Re(z)|), \\ H_{d,2}(z, v_c) &= 1. \end{aligned} \tag{4.14}$$

This leads to three different definitions for $Z(z, f_0')$ in the LHP:

$$\begin{aligned} Z_{0,LHP}(z, f_0') &= \int_{-v_c}^{v_c} \frac{F_0'(v)}{v - z} \mathrm{d}v + F_0(v_c) \frac{2v_c}{z^2 - v_c^2}, \\ Z_{1,LHP}(z, f_0') &= \int_{-v_c}^{v_c} \frac{F_0'(v)}{v - z} \mathrm{d}v + 2\pi i F_0'(z) H(v_c - |\Re(z)|) + F_0(v_c) \frac{2v_c}{z^2 - v_c^2}, \\ Z_{2,LHP}(z, f_0') &= \int_{-v_c}^{v_c} \frac{F_0'(v)}{v - z} \mathrm{d}v + 2\pi i F_0'(z) + F_0(v_c) \frac{2v_c}{z^2 - v_c^2}. \end{aligned} \tag{4.15}$$

It is important to note that the family of $Z_i(z, f_0')$, where $i = 0, 1, 2$, are neither entire nor meromorphic functions. Specifically, $Z_0(z, f_0')$ is discontinuous on the real axis at $|\Re(z)| > v_c$, $Z_1(z, f_0')$ is discontinuous on the LHP lines $|\Re(z)| = v_c$, and $Z_2(z, f_0')$ is discontinuous on the real axis at $|\Re(z)| < v_c$ (as can be seen in Fig. 8.1).

The following key problem then arises: while the UHP and real axis descriptions are not affected and remain unique, the LHP description depends on the specific complex extension chosen for $H_{d,i}(z)$. Different dielectric tensors $\epsilon = k'^2 - Z_i(z, k')$, with distinct roots, follow.

[5] the calculation is based on the hypothesis that the delta correction term diverges faster than the integral term. We set $\varepsilon = \omega/k - v_c$ as expansion parameter.

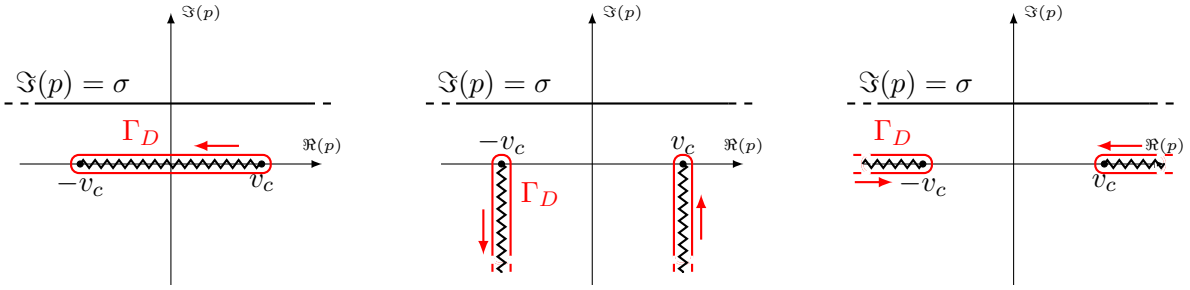

Figure 4.1: From left to right, the discontinuities generated by the different definitions for the 'window' function, $H_{d,0}$, $H_{d,1}$, and $H_{d,2}$, and the associated contour Γ_D needed for the 'generalized' residue theorem.

If we were to follow Landau's approach blindly and summed over the pole residues to describe the electric field evolution, we would obtain different solutions. Therefore, a generalization of Landau's method is required.

In the original approach, the electric field solution was given as

$$E(t,k) = \frac{1}{2\pi}\int_{i\sigma-\infty}^{i\sigma+\infty} e^{-ipt}\tilde{E}(p,k)\mathrm{d}p. \tag{4.16}$$

Under the assumption of entire or meromorphic $\tilde{E}(p,k)$, we applied the residue theorem on the contour made of the horizontal line $\Im(p) = \sigma$ and a LHP semicircle with an infinite radius. In the case of cut-off distributions, the key point is to observe that extending the window function $H_d(z)$ into the LHP leads to non-isolated points of discontinuity (branch cuts) for $Z(z, f_0')$ and $E(p,k)$.

To still apply the residue theorem to Eq. (4.16), the original contour must be modified by adding a contour Γ_D that circumvents the discontinuities (see Fig. 4.1). The generalized version of Eq. (2.16) becomes

$$E(t,k) = \frac{1}{2\pi}\int_{i\sigma-\infty}^{i\sigma+\infty} e^{-ipt}\tilde{E}(p,k)\mathrm{d}p = -i\sum_n \mathrm{Res}\left\{e^{-ip_n t}\tilde{E}(p_n,k)\right\} - \frac{1}{2\pi}\int_{\Gamma_D} e^{-ipt}\tilde{E}(p,k)\mathrm{d}p.^{6} \tag{4.17}$$

In general, it can be shown that the integral over Γ_D is non-zero and decays not slower than $1/t$ [33]. As a result, in case of cut-off distributions, the final electric field cannot be expressed solely in terms of residues, and an extra integral contribution must be taken into account. As a final comment, we mention that:

- Except for allowing more convenient analytical expressions, the three chosen definitions for $H_d(z)$ are arbitrary choices among an infinite set of other possibilities. The contour dividing the '0' region from the '1' region can be shaped arbitrarily, provided it connects $z = -v_c$ and $z = v_c$. A simple alternative example for $H_d(z)$ is $H_{d,4} = H(v_c - |z|)$, where the 1-region corresponds to a semicircle with radius v_c in the LHP.

- Although we limited, for clarity, the present discussion to symmetric cut-off distributions, the arguments presented here hold true, with slight modifications, for every case where the distribution function f_0 does not admit a unique complex definition $f_0(z)$. The recipe remains the same: introduce an arbitrary LHP definition apply the residue theorem within a contour that circumvents the branch cut discontinuities.

[6] Where, as in the original case, the integral over the infinite radius semicircle vanishes.

A Privileged Definition for $H_d(z, v_c)$

Even though we argued, and we will illustrate further, that the different complex extensions for $H_d(z, v_c)$ are mathematically equivalent and lead to the same solution for the electric field, there is one definition that can be considered privileged, as it is the one that is compatible with the standard Landau damping interpretation as a resonance effect. According to this interpretation, Landau damping occurs because of the interaction between the electric field wave and the resonant particles with velocity $v \approx \omega/k$. As a consequence, for a cut-off distribution we would expect that, as already shown, a stable solution is not only possible in a region without particles (i.e., $|\omega/k| > v_c$), but also that a damped solution is not possible in the same region without particles. In other terms, we would expect a stable solution if and only if $|\omega/k| > v_c$. $H_{d,2}$ can be shown to be the only definition compatible with such condition for any value of k. Fig. 4.2 shows the dispersion relation in the case of a cut-off $\kappa = 1$ distribution, extended with $H_{d,2}$. The fact that stable solutions exist if and only if $\omega/k > v_c$ can be easily observed.

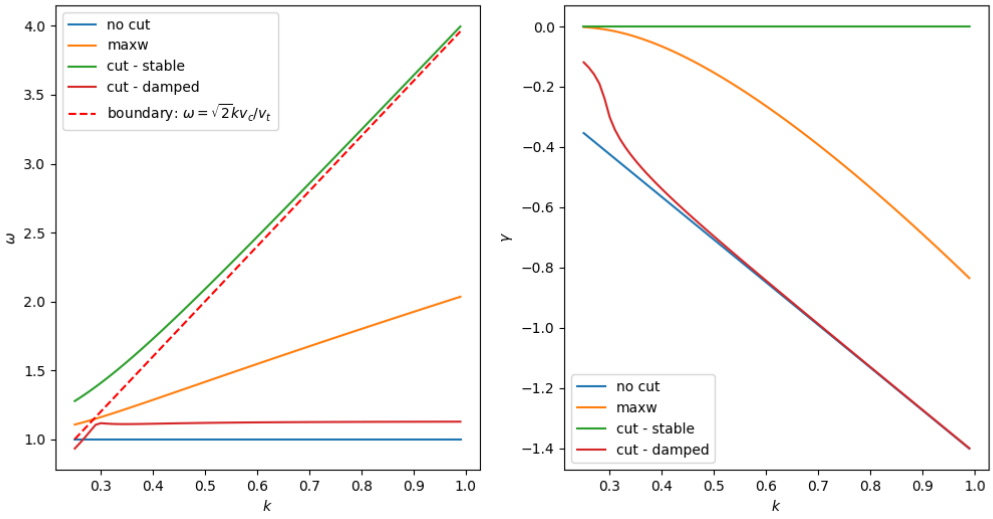

Figure 4.2: Dispersion relation for $\kappa = 1$ case with $v_c = 4$, $v_t = 2$ and $H(z, v_c) = H_{d,2}(z, v_c)$.

In summary, if other H_d definitions are just a mathematical redundancy or bearer of a different physical meaning is yet a mystery, but we can argue that $H_{d,2}$ appears as the only one compatible with the wave-resonance particles interaction picture. Nevertheless, in the following sections, we keep investigating on the different definitions for the LHP.

4.2.4 Different LHP Definitions: Checking the Results with a κ Distribution

To assess the mathematical equivalence of different LHP definitions, we examine a cut-off $\kappa = 1$ distribution function, defined as

$$f_{\kappa=1}(v) = \frac{N}{\sqrt{\pi} v_t} \frac{1}{(1 + \frac{v^2}{v_t^2})} H_d(v, v_c) = F_{\kappa=1}(v) H_d(v, v_c) \tag{4.18}$$

By using the three different definitions for H_d and Z_i from Eqs. (4.14) and (4.15), we define $Z_0(z, f'_{\kappa=1})$, $Z_1(z, f'_{\kappa=1})$ and $Z_2(z, f'_{\kappa=1})$. These three functions share the same definition in the UHP and along the real axis (see Eqs. (4.4) and (4.6)), while they have three different

definitions in the LHP, in accordance with Eq. 4.15. Additionally, we define three corresponding (renormalized) dieletric tensors $\epsilon_{i,k'}(z) = k'^2 - v_t^2 Z_i(z)/2$, with $i = 0, 1, 2$.

In Figs. 4.3 and 4.4, the imaginary part of $Z_i(z)$ and the absolute value of $\epsilon(z, k')$ are displayed. The chosen parameters are: $v_t = \sqrt{2}$, $v_c = 1$, $k' = 1$. It is worth noting the different locations of discontinuities and the varying pole structures. Moreover, the four-lobed structure described in a previous chapter is also visible (in this case $2n = 4$, with $n = \kappa + 1$). We refer to Sec. 3.1, for comparison with the no-cut κ case.

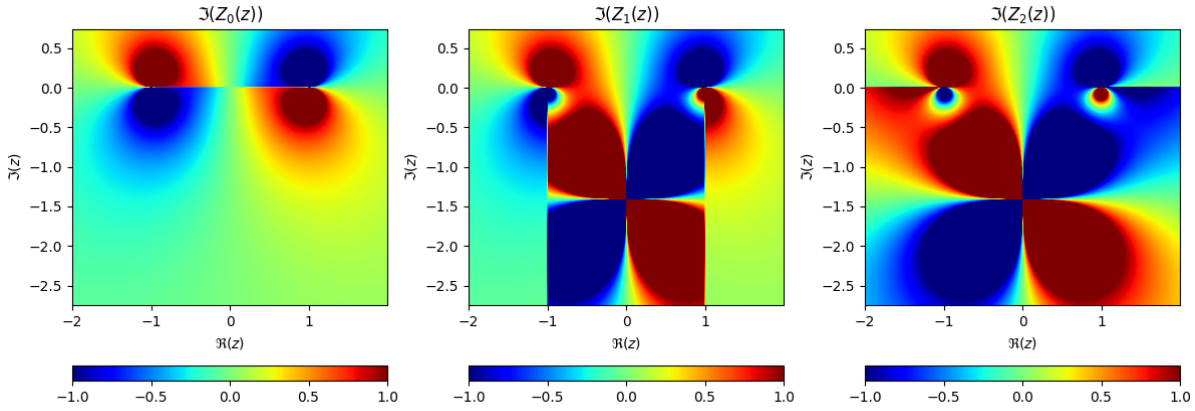

Figure 4.3: κ distr. with cut at $v_c = 1$. From left to right, imaginary part of $Z_0(z)$, $Z_1(z)$, and $Z_2(z)$.

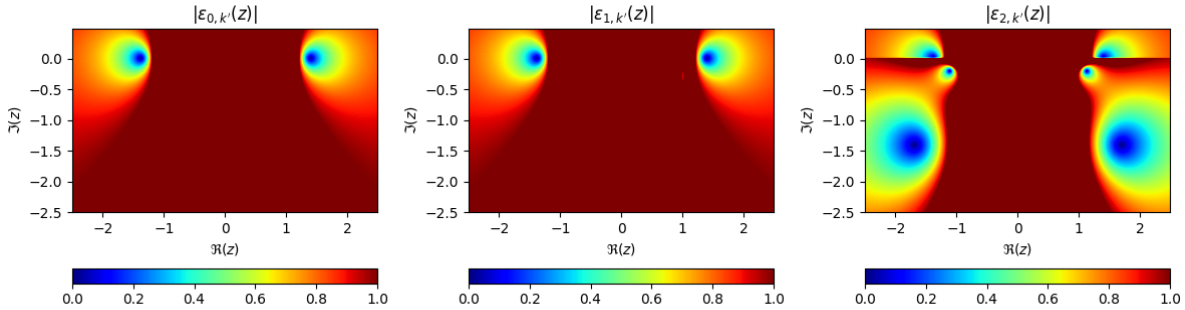

Figure 4.4: κ distr. with cut at $v_c = 1$. From left to right, absolute value of $\epsilon_{0,k'}(z)$, $\epsilon_{1,k'}(z)$, and $\epsilon_{2,k'}(z)$. The zeros of the plots (blue spots) represent the roots of the dispersion relation.

Now, we aim to verify that, by properly accounting for the discontinuity integral, the electric field evolution does not depend on the specific choice for $H_{d,i}$. This verification is essentially a mere application of standard complex variable integration techniques. For each $H_{d,i}$ and $Z_i(z, f'_{\kappa=1})$, we intend to compute the electric field $E_i(t, k)$ as per Eq. (2.9),

$$E_i(t,k) = \int_{i\sigma-\infty}^{i\sigma+\infty} e^{-ipt} \left[\frac{(p-1j)^{-4}}{1 - Z_i(p, f'_{\kappa=1})} \right] \mathrm{d}p. \tag{4.19}$$

To simplify the calculations, we have omitted the constants in front of the integral and assumed that the numerator integral in Eq. (2.8) is $(p - 1j)^{-4}$. This choice for the numerator allows us to avoid the additional computational burden arising from the numerator integral. Whether this choice is valid for the Vlasov Poisson system and the assumptions we made on $f_1(t = 0)$ is

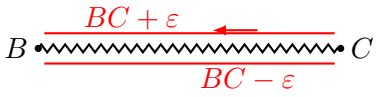

Figure 4.5: Decomposition of the Γ_D contour around the discontinuity BC, needed for the integral of Eq. (4.20). We assume that the integrand is integrable around B and C, so that the contributions from the 'short edges' of Γ_D can be made arbitrarily small, and thus neglected.

not our primary concern; we are neglecting the role of the initial perturbation $f_1(t=0)$ and we are only interested in the distinct behaviours induced by the different denominators $1 - Z_i(p)$. However, since $(p-1j)^{-4}$ has a singularity at $p = 1j$, we must select σ from the interval $(0, 1)$, so that we can apply the residue theorem without taking into account such a singularity.

We then compute $E(t,k)$ using two methods:

1. We integrate along the horizontal line with $\Im(p) = \sigma$, directly using Eq. (4.19). The electric field computed using this approach is represented by the green lines in Figs. 4.6. Since the integration is performed at $\sigma > 0$, in the UHP, where $Z_i(z)$ share the same definition, this method of computing $E(t,k)$ does not depend on the chosen index i.

2. we apply the 'generalized' residue theorem, as explained, taking into account the residues sum as well as the additional integration along Γ_D. The residue term is accounted for through Eq. 2.16, by replacing the numerator with the aforementioned numerator function $1/(p-1j)^4$ and by properly computing the derivative of the dielectric function.[7] The poles p_n are determined 'graphically', by varying the axis and color ranges of Fig. 4.4 until the position of the pole (blue spot) can be inferred with a precision of at least 1%.

   On the other side, for a given discontinuity line BC, we decompose the contour Γ_D around BC as the union of two segments $(BC+\varepsilon) \cup (BC-\varepsilon)$ (see Fig.4.5). We then compute the discontinuity integral as follows:

$$\begin{aligned}\int_{\Gamma_D} e^{-ipt}\left[\frac{(p-1j)^{-4}}{1-g(p)}\right]\mathrm{d}p &= \int_{BC+\varepsilon} e^{-ipt}\left[\frac{(p-1j)^{-4}}{1-Z_i(p,f'_{\kappa=1})}\right]\mathrm{d}p - \int_{BC-\varepsilon} e^{-ipt}\left[\frac{(p-1j)^{-4}}{1-Z_i(p,f'_{\kappa=1})}\right]\mathrm{d}p \\ &= \int_{BC} e^{-ipt}(p-1j)^{-4}\left[\frac{1}{1-Z_i(p+\varepsilon,f'_{\kappa=1})} - \frac{1}{1-Z_i(p,f'_{\kappa=1})}\right]\mathrm{d}p,\end{aligned} \tag{4.20}$$

   where we exploit the fact that the integrand, without the denominator, is a continuous function of p. We can neglect the corner integrals, since they can be made arbitrarily small by reducing ε.

The results are shown in Fig. 4.6 for each choice of $Z_i(z)$. The total electric field, whether obtained through integration or through the 'generalized' Landau approach, match. The significant difference lies in the relative contribution of residues and discontinuity integrals, that depend on the chosen index i. For instance, at long times, the residues contribution is dominant for $E_0(t)$ and $E_1(t)$, but goes to zero for $E_2(t)$.

In summary, we have thus verified that regardless of the different possible definitions in the lower half plane, the final solution remains unaffected, provided a generalized Landau's approach is followed. Nevertheless, it is crucial to note that such a generalized approach appears impractical. The main purpose of Landau's approach is to avoid the direct computation of the

[7] We evaluate the derivative $\left.\frac{d\epsilon}{\mathrm{d}p}\right|_{p_n}$ as the finite difference $\frac{\epsilon(p_n+\varepsilon)-\epsilon(p_n)}{\varepsilon}$, with $\varepsilon = 0.00001$.

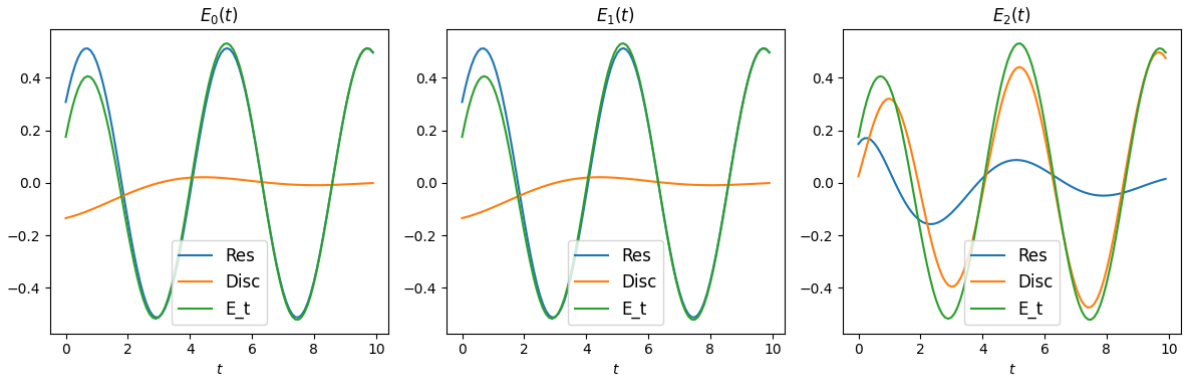

Figure 4.6: Electric field evolution for the three different definitions of $Z_i(z, f_0')$. The relative contributions of residues and discontinuity integrals is highlighted.

integral along $\Im(z) = \sigma$ (as in Eq. (4.16)), by using a more convenient and agile sum of residues. But for cut-off distributions, it has been found that the same integral along $\Im(z) = \sigma$ cannot be simplified into a mere sum of residues, and an additional integral is necessary (Eq. (4.20)). Therefore, such a trade-off of one integral for another does not appear as a convenient approach.

Two Possible Approaches

After analyzing the outcomes of the preceding section, two viable approaches emerge for dealing with the cut-off distribution scenario:

- **Long Time Limit Approach:** It is a common practice in the Landau damping literature to concentrate solely on the electric field long-time behavior. In practical terms, this consists in seeking only the solution with the least damping, which, in the case of cut-off distributions, corresponds to a stable solution with no damping. Consequently, if $f_0(v)$ is a cut-off distribution, the overall linear Vlasov-Poisson problem can be simplified to exclusively solving the real axis dispersion relation (Eq. (4.7)). This approach essentially disregards the entire description in the LHP and any associated discontinuity issues.

- **Full Time Description Approach:** The previous section revealed that a unique physical evolution of the electric field can be represented through multiple equivalent but distinct mathematical descriptions. Deeply unsettled by this observation, we persist in investigating the LHP description, aiming to extract further insights from the discontinuity integral and the overall LHP representation.

We opt for the second approach. Our strategy involves utilizing sigmoid functions to smooth-out and approximate cut-off distribution functions.

Lastly, we mention that on a deeper level, the investigation of the upcoming section is motivated by the pole extraction mechanism involving GAMs and EGAMs, and by the similar formulation for the LVP dispersion relation and the gyrokinetic dispersion relation of Chapter 7. We will provide more context in Chapter 6.1. For the time being, we only mention that a linear mechanism that can extract and destabilize poles from the LHP by bringing them into the UHP has been described [34]. If such a mechanism exists, we then wonder how the same mechanism could hold if the LHP admits different pole structures, that depend on the arbitrary choice of the LHP description. Tackling the problem in the specific context of GAMs and EGAMs is left for future work. At the moment we limit ourselves to the simpler LVP system.

4.3 Step Function Approximation via Sigmoid Functions

The crucial point of the previous section was that various LHP descriptions are possible when dealing with cut-off distribution functions, $f_0(v)$. However, we recall that for the original Landau's treatment, only apt for entire or meromorphic functions, the LHP description is unique. We then aim to define a sequence of meromorphic functions that converge to a cut-off distribution, and examine how the transition from unique to non-unique LHP descriptions occurs. In practical terms, we smooth out the discontinuous cut-off distributions by using sigmoid functions, and we investigate how the generalized plasma dispersion function and the electric field solution are affected by such smoothing out process.

It is noteworthy that smoothing cut-off distribution functions is not only interesting, in more abstract terms, as a means to examine the non-uniqueness of the LHP description for ill-defined cases. It is also significant because, on a more practical level, it produces smooth distribution functions that are more realistic than sharp edges cut-off distributions. The greater realism is simply due to the fact that collision processes tend to naturally mitigate sharp edges present in the distribution function.

We start by considering a general sequence of functions, $g_\alpha(v)$ that converge to $g_0(v)$ as $\alpha \to 0$, and the corresponding sequence of GPDF, $Z(z, g'_\alpha)$.

In the UHP, we have

$$\lim_{\alpha\to 0} Z_{UHP}(z, g'_\alpha) = \left[\int_{-\infty}^{\infty} \frac{g'_\alpha(v)}{v-z}\mathrm{d}v\right], \tag{4.21}$$

while in the LHP, we have

$$\lim_{\alpha\to 0} Z_{LHP}(z, g'_\alpha) = \left[\int_{-\infty}^{\infty} \frac{g'_\alpha(v)}{v-z}\mathrm{d}v + 2\pi i g'_\alpha(z)\right]. \tag{4.22}$$

It can be demonstrated, via the dominated convergence theorem, that $\lim_{\alpha\to 0} Z_{UHP}(z, f'_\alpha) = Z_{UHP}(z, f)$. With some additional steps, it is then possible to prove that the electric field solution, given as an integral in the UHP (see Eq. (2.19)), is well-behaved in the limit $\alpha \to 0$. In other words, the electric field resulting from the linear VP system with $f_0(v) = g_\alpha$ converges to the electric field resulting from the linear VP system with $f_0(v) = g_0(v)$. As trivial as it might seem, confirming the electric field convergence is important because, as we are about to see, the GDPF exhibits a peculiar behavior in the LHP.

Now, let us focus on GPDF in the lower half plane. The left term is the same as in the UHP definition, and it can be shown to converge harmlessly to

$$\int_{-\infty}^{\infty} \frac{g'_0(v)}{v-z}\mathrm{d}v. \tag{4.23}$$

However, the peculiar behaviour arises in the LHP through the term $2\pi i g'_\alpha(z)$. To illustrate this, we consider a cut-off distribution $g_0 = G_0 H_d(v, v_c)$, and we smooth it out by replacing the 'window' function $H_d(v, v_c)$ with the product of two sigmoid functions $\sigma_\alpha(v)$:

$$g_\alpha(v) = \sigma_\alpha(v + v_c) \cdot g_0(v) \cdot \sigma_\alpha(-v + v_c), \tag{4.24}$$

Two specific sigmoid approximations are examined: the erf sigmoid $\sigma_{erf,\alpha}$ and the logistic sigmoid $\sigma_{log,\alpha}$:

$$\sigma_{\mathrm{erf},\alpha}(v) = \frac{1 + \mathrm{erf}(v/\alpha)}{2} \to H(v) = \begin{cases} 1 & v > 0, \\ 1/2 & v = 0, \\ 0 & v < 0, \end{cases} \tag{4.25}$$

$$\sigma_{\log,\alpha}(v) = \frac{1}{1+e^{-v/\alpha}} \to H(v) = \begin{cases} 1 & v > 0, \\ 1/2 & v = 0, \\ 0 & v < 0. \end{cases} \tag{4.26}$$

As shown in Fig. 4.7, on the real axis both σ_{erf} and σ_{log} converge point-wise to the step function.

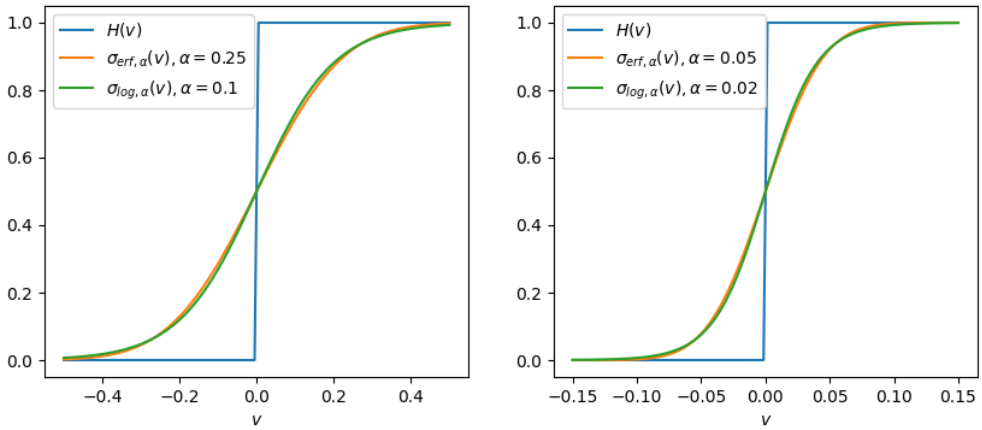

Figure 4.7: Step function approximation via sigmoid functions, σ_{erf} and σ_{log}, for different α parameters.

To study the behaviour in the complex plane, we start by defining $\sigma(z)$ by simply replacing the real variable v with the complex variable z. For the logistic sigmoid, we decompose $\sigma_{\alpha,log}(z = x + iy)$ into its real and imaginary part:

$$\frac{1}{1+e^{-z/\alpha}} = \frac{1+e^{-x/\alpha}\cos(\frac{y}{\alpha})}{\left[1+e^{-x/\alpha}\cos(\frac{y}{\alpha})\right]^2 + \left[e^{-x/\alpha}\sin(\frac{y}{\alpha})\right]^2} + i\frac{e^{-x/\alpha}\sin(\frac{y}{\alpha})}{\left[1+e^{-x/\alpha}\cos(\frac{y}{\alpha})\right]^2 + \left[e^{-x/\alpha}\sin(\frac{y}{\alpha})\right]^2} \tag{4.27}$$

In the limit $\alpha \to 0$ we obtain

$$\lim_{\alpha\to 0}\left[\frac{1}{1+e^{-z/\alpha}}\right] = \begin{cases} 1+i0 & x > 0 \\ 0+i0 & x < 0 \\ \frac{1}{2}+i0 & x = 0 \end{cases} \tag{4.28}$$

$\sigma_{\alpha,log}$ is then converging point-wise to the function $H(\Re(z))$. It is important to mention that the convergence is not uniform. In fact, when $y = -\pi\alpha - 2\pi m\alpha$, Taylor-expanding around $x = 0$ yields

$$\lim_{x\to 0}\left[\frac{1}{1+\exp(-x/\alpha + i\pi^{\pm})}\right] = \infty \mp i\infty. \tag{4.29}$$

In the erf sigmoid case, we decompose $\sigma_{log,\alpha}$ into a sum of two terms:

$$\begin{aligned} \frac{\sqrt{\pi}}{2}\operatorname{erf}(z/\alpha) &= \int_0^{z/\alpha} e^{-t^2}\mathrm{d}t = \int_0^{x/\alpha} e^{-t^2}\mathrm{d}t + i\int_{x/\alpha}^{x/\alpha+iy/\alpha} e^{-t^2}\mathrm{d}t \\ &= \int_0^{x/\alpha} e^{-t^2}\mathrm{d}t + i\int_0^{y/\alpha} e^{-(x+is)^2}\mathrm{d}s \\ &= \int_0^{x/\alpha} e^{-t^2}\mathrm{d}t + i\int_0^{y/\alpha} e^{-(x/\alpha)^2+s^2}e^{-2ixs/\alpha}\mathrm{d}s, \end{aligned} \tag{4.30}$$

and in the limit we have

$$\begin{aligned}\lim_{\alpha\to 0}\frac{\sqrt{\pi}}{2}|\operatorname{erf}(z/\alpha)| &\leq \lim_{\alpha\to 0}\left[\left|\int_0^{x/\alpha} e^{-t^2}\mathrm{d}t\right| + \left|\int_0^{y/\alpha} e^{-(x/\alpha)^2+s^2}e^{-2ixs/\alpha}\mathrm{d}s\right|\right] \\ &= \frac{\sqrt{\pi}}{2} + \lim_{\alpha\to 0}\left|\int_0^{y/\alpha} e^{-(x/\alpha)^2+s^2}\mathrm{d}s\right| \\ &\leq \frac{\sqrt{\pi}}{2} + \lim_{\alpha\to 0}\frac{|y|}{\alpha}e^{-(x^2-y^2)/\alpha}\end{aligned} \tag{4.31}$$

So, considering Eq. (4.31) and analysing the sign of the integral $|\int_0^{x/\alpha} e^{-t^2}|$, yields that, in the region $\Re(z)^2 - \Im(z)^2 > 0$, $\sigma_{\alpha,erf}(z)$ converges to 1 if $\Re(z) > 0$ and to 0 if $\Re(z) < 0$. Outside the region $\Re(z)^2 - \Im(z)^2 > 0$ no convergence is guaranteed.

The comparison between the erf and logistic sigmoid is plotted in Fig. 4.8.

So, the key observation is the following. If we consider two 'smooth' cut-off distributions:

$$g_{\alpha,erf}(z) = \sigma_{\alpha,erf}(z + v_c)\cdot F_0(z)\cdot\sigma_{\alpha,erf}(-z + v_c), \tag{4.32}$$

and

$$g_{\alpha.log}(z) = \sigma_{\alpha,log}(z + v_c)\cdot F_0(z)\cdot\sigma_{\alpha,log}(-z + v_c), \tag{4.33}$$

they converge to the same cut-off distribution $g_0 = F_0 H_d(v, v_c)$ on the real axis and the corresponding electric field evolution will be the same. Nevertheless, the behaviour of $g_{\alpha,erf}(z)$ and $g_{\alpha,log}(z)$, and the corresponding dielectric tensors and $\tilde{E}(p,k)$, is utterly different. We are then led to the following conclusion: the non-uniquess of the LHP description for cut-off distributions is emerging from the different possibilities we have to smooth out a step function, and from the fact that analytic functions that share the same limit on the real axis do not necessarily share the same limit in the whole complex plane.

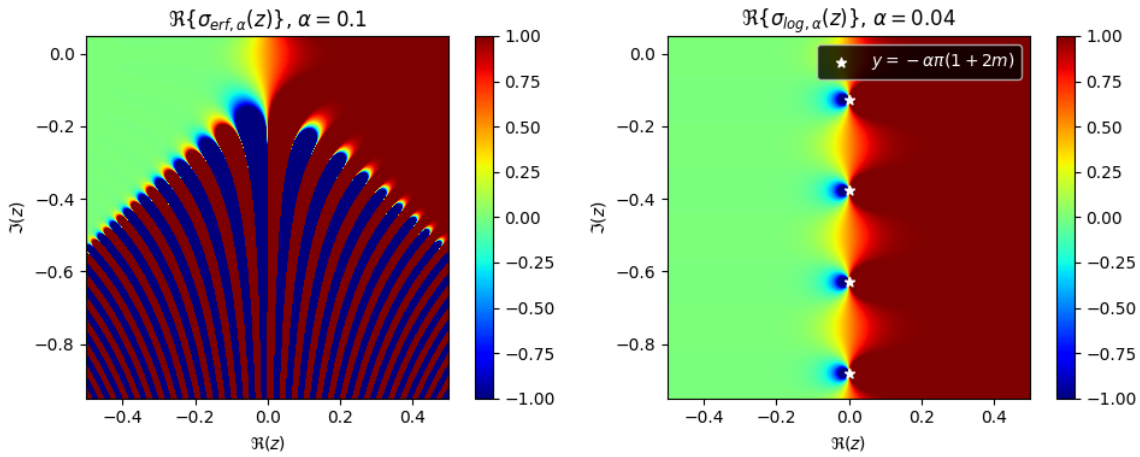

Figure 4.8: Representation of the complex valued sigmoid functions $\sigma_{\mathrm{erf}}(z)$ and $\sigma_{log}(z)$. The singularity points $Im(z) = -\alpha\pi(1+2m)$ are also shown.

4.3.1 Different Pole Structures (a Collection of Magnificent Plots)

To support the statement that different LHP descriptions for the cut-off distribution case are generated though different approximations of the step function, we now narrow our discussion

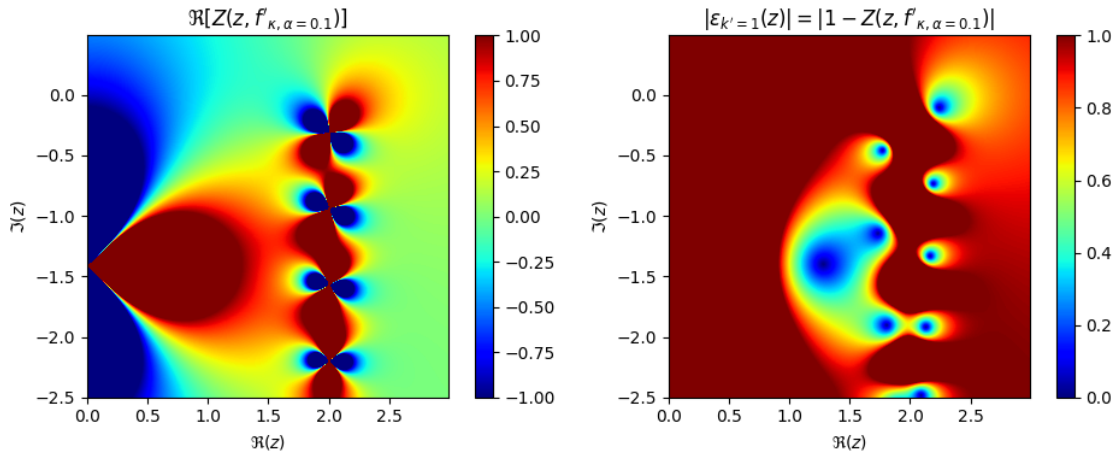

Figure 4.9: 'Strong smoothing': real part of $Z(z, f'_{\kappa=1,\alpha=0.1})$ and absolute value of $\epsilon_{k'}(z)$.

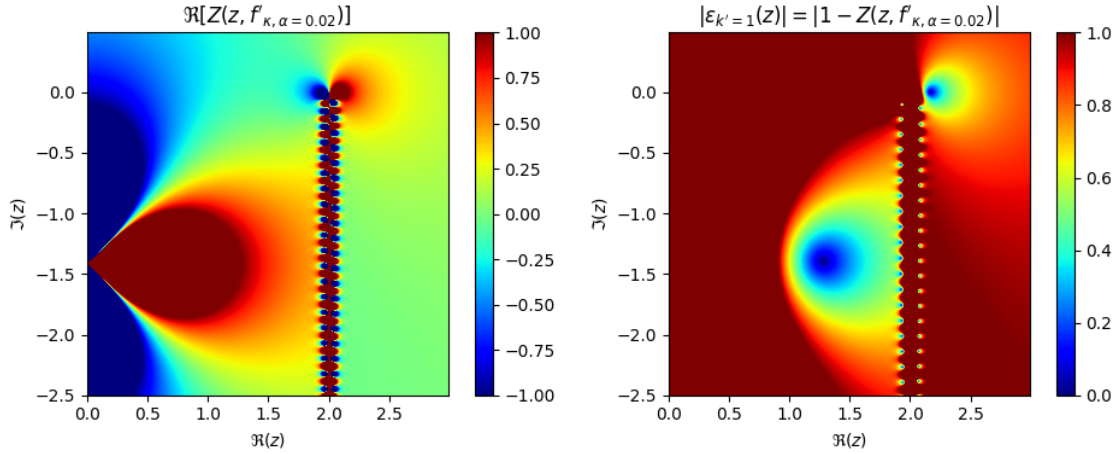

Figure 4.10: 'Weak smoothing': real part of $Z(z, f'_{\kappa=1,\alpha=0.02})$ and absolute value of $\epsilon_{k'}(z)$.

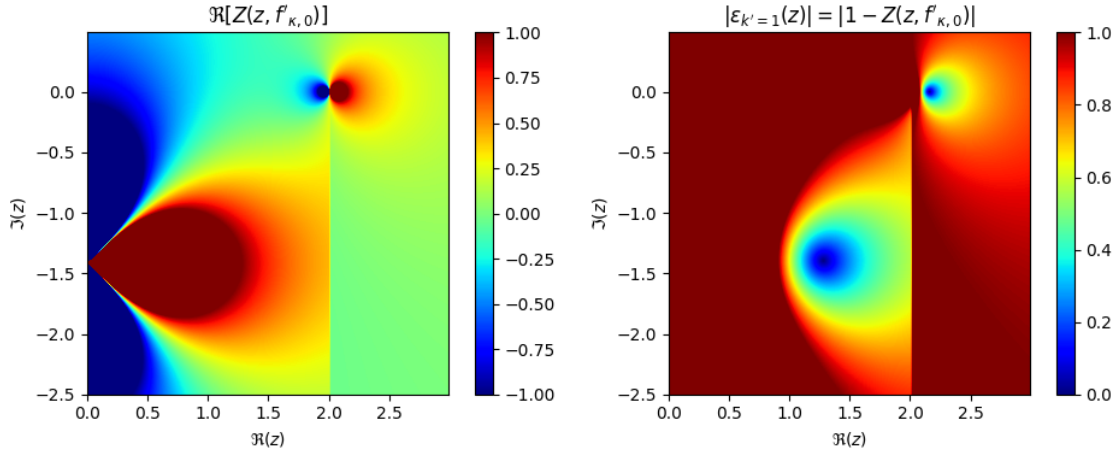

Figure 4.11: 'No smoothing': real part of $Z(z, f'_{\kappa=1,0})$ and absolute value of $\epsilon_{k'}(z)$.

to a specific scenario. In this case, we assume that the equilibrium distribution function $f_0(v)$ is a $\kappa = 1$ cut-off distribution, smoothed out by two logistic sigmoids:

$$f_{\kappa,\alpha}(z) = N(\alpha)\sigma_{log,\alpha}\left(z + v_c\right)\frac{1}{v^2 + v_t^2}\sigma_{log,\alpha}\left(-z + v_c\right), \tag{4.34}$$

where $N(\alpha)$ corresponds to the normalization constant, and the following parameters have been chosen: $k' = 1$, $v_c = 2$, $v_t = \sqrt{2}$. In Figs. 4.9 and 4.10 we can observe the real part of $Z(z, f'_{\kappa=1,\alpha=0.1})$ and $Z(z, f'_{\kappa=1,\alpha=0.02})$, along with the absolute value of the associated dielectric tensor $\epsilon_{k'}(z)$. In Fig. 4.11, the real part of $Z(z, f'_{\kappa=1,0})$, and the corresponding dielectric tensor, are plotted for the discontinuous case, with

$$f_{\kappa=1,0}(z) = N\frac{1}{v^2 + v_t^2}H(v_c - |\Re(z)|). \tag{4.35}$$

We can make the following observations regarding the pole structure.

- In all the Z plots (left plots in the previous page), we can still recognize the lobe structure of the no-cut $\kappa = 1$ distribution, along with the associated pole, which is the left-most pole in the the dielectric tensor plots (right plots).
- The complex plane singularities of the sigmoid function derivative ($\Im(z) = -\alpha\pi(1 + 2m)$) generate an infinite number of poles in the vicinity of $\Re(z) = v_c$, with two poles for each singularity (as we discussed earlier, the number of poles is equal to the singularity order, two in this case). As α decreases such poles get denser and closer to $\Re(z) = v_c$.
- Among the sigmoid poles, there is one with the smallest damping and the highest frequency, which behaves differently from the others and resembles the stable pole of the $f_{\kappa=1,0}(z)$ case, shown in Fig. 4.11.

We then arrive to the following conclusion: as $\alpha \to 0$, the smooth cut-off distribution LHP description tends to the LHP description where the 'window' function $H_d(v, v_c)$ is extended into the complex plane as $H_{d,2} = H(v_c - |\Re(v)|)$. In particular, among the infinite number of poles associated to the sigmoid function, the one with smallest damping corresponds, in the limit, to the stable pole of the cut-off distribution case; and the other sigmoid poles, by becoming denser and closer to $\Re(z) = v_c$, are instead generating the line discontinuity that characterizes $H_{d,2} = H(v_c - |\Re(v)|)$.

Furthermore, we notice that the pole structure induced by the logistic smoothing of the cut-off, keeps the compatibility with the resonant particles-wave interaction interpretation. The new poles are in fact emerging exclusively for waves that resonate in the region of the 'smoothing', namely $\omega/k \approx v_c$. The same cannot be said, for instance, for the erf sigmoid case, briefly displayed in Extra B. In this case, the 'smoothing-generated' poles approximately lie on two lines stemming from $z = v_c$ and at approximately $-3\pi/4$ and $-\pi/4$ angles, hence implying that damped poles exist with $\omega/k \gg v_c$.

Numerical Computation of the Plots of Figs. 4.9, 4.10 and 4.11: While the discontinuous case with H_d admits analytical formulas (see the Extra at the end of the chapter), the case with sigmoid cut-off does not. We thus deploy Xie's algorythm [5] in full glory to numerically compute $Z(z, f'_{\kappa=1,\alpha=0.1})$ and $Z(z, f'_{\kappa=1,\alpha=0.02})$. An explanation of the algorythm will follow in Chapter 5

However, an observation is here important. When examining the definition of $\sigma_{\alpha,log}$, we notice that the exponential term $\exp v/\alpha$ is computationally 'dangerous'. In the sense that,

outside some safe range around $v = 0$, it assumes very large values and leads to numerical overflow. To circumvent these overflow issues, we simplify the derivative f' as follows:

$$f'_{\kappa,\alpha} = \begin{cases} \sigma_{log,\alpha}(z + v_c) \cdot F'_0(z) + \sigma'_{log,\alpha}(z + v_c) \cdot F_0(z), & \text{if } -v_c - x < \Re(z) < 0, \\ \sigma_{log,\alpha}(-z + v_c) \cdot F'_0(z) + \sigma'_{log,\alpha}(-z + v_c) \cdot F_0(z), & \text{if } 0 < \Re(z) < v_c + x, \end{cases} \tag{4.36}$$

where x is an arbitrarily chosen parameter that prevents overflow. For $\alpha = 0.02$, we set $x = 3$. Such an approximation is only possible because of the symmetry of $\sigma_{log,\alpha}(z)$, that outside some range around the center, does not depend on the imaginary part, i.e. $\sigma_{log,\alpha}(z) = \sigma_{log,\alpha}(\Re(z))$. Dealing with overflow problems in the erf sigmoid case would be more complicated, which is why we generally opt to utilize the logistic sigmoid.

Some plots for the erf sigmoid case, illustrating overflow regions, are given in section Extra B at the end of this chapter.

4.3.2 Reconstructing the Electric Field

As a last point of the present section, we carry out a simple verification of our previous considerations. In particular, we compute the electric field evolution for the case $f_0 = f_{\alpha,\kappa}$ with the same methods presented in Subsection 4.2.4. So, on one side, we compute E by direct integration on $\Im(p) = \sigma$. On the other side, we compute E by applying the residue theorem. In this case, as $f_0 = f_{\alpha,\kappa}$ is meromorphic, no Γ_D contributions need to be taken into account. We consider the case $\kappa = 1$, $\alpha = 0.02$, $k' = 1$, $v_t = \sqrt{2}$, $v_c = 2$, and the poles to account for have already been shown in Fig. 4.10. Such a calculation is nothing more than a verification of the residue theorem, but it bears a very important practical result: the discontinuity lines of the cut-off case have been replaced by poles through sigmoid-smoothing. This directly implies that the contribution of such discontinuities to the electric field can be now expressed in terms of a convenient sum over residues, instead of a computationally heavier integration.

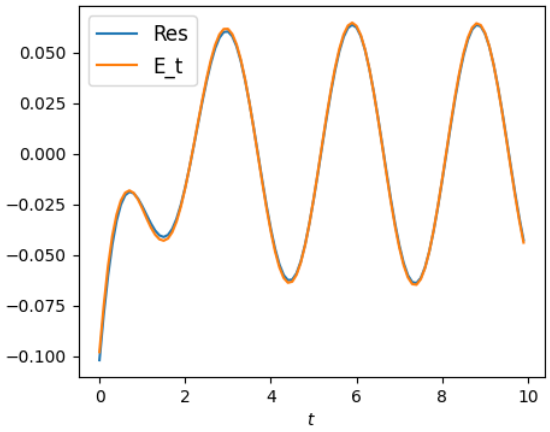

Figure 4.12: Electric field solution with $f_0 = f_{\kappa=1,\alpha=0.02}$, computed using direct integration, 'E_t', and the residue theorem, 'Res'.

4.4 Slowing Down

We now explore for the first time the specific example that has motivated the present work: the Slowing-Down distribution function. In the context of ignited fusion plasmas, fusion born

alpha particles, are usually not Maxwellian because of their high birth energies compared to the background. Instead, the Slowing Down distribution function is typically employed.

For the 1D Vlasov Poisson problem, we adopt the 1D definition from [5],

$$f_{SD} = N(v_t, v_c)\frac{1}{|v|^3 + v_t^3}H_d(v, v_c), \tag{4.37}$$

where v_t represent the crossover velocity, v_c stands for the cut-off velocity, and $N(v_t, v_c)$ is the normalization constant, which depends on the chosen v_t and v_c.

The distribution is called 'Slowing-Down', because it describes the drag of the background electrons and ions on the DT-fusion born αs. It is derived from the Fokker-Planck equation under the assumption that D (deuterium) and T (tritium) have the same energy T_i and that the energy spectrum is approximately Maxwellian [3].

4.4.1 Pole Structure

We now employ the arguments from the previous sections to analyse the structure of the Slowing-Down GPDF, $Z_{SD}(z) = Z(z, f'_{SD})$. Right from the start, we observe the compact support of this function. By defining $F_{SD}(v) = N(v_t, v_c)\frac{1}{|v|^3+v_t^3}$, we draw upon Eqs. (4.4),(4.6) and (4.15), and we formally define $Z(z, f'_{SD})$ as

$$Z_{SD}(z) = \begin{cases} F_{SD}(v_c)\dfrac{2v_c}{z^2 - v_c^2} + \displaystyle\int_{-\infty}^{\infty} \frac{F'_{SD}(v)H_d(v, v_c)}{v - z}\mathrm{d}v, & \text{if } \Im(z) > 0, \\ F_{SD}(v_c)\dfrac{2v_c}{z^2 - v_c^2} + \mathrm{P.V.}\displaystyle\int_{-\infty}^{\infty} \frac{F'_0(v)H_d(v, v_c)}{v - z}\mathrm{d}v + i\pi F'_{SD}(v)H_d(v, v_c), & \text{if } \Im(z) = 0, \\ F_{SD}(v_c)\dfrac{2v_c}{z^2 - v_c^2} + \displaystyle\int_{-\infty}^{\infty} \frac{F'_{SD}(v)H_d(v, v_c)}{v - z}\mathrm{d}v + 2i\pi F'_{SD}(z)H_d(z, v_c), & \text{if } \Im(z) < 0. \end{cases} \tag{4.38}$$

Once again, the definition issues arise in the LHP with the term $2i\pi F'_{SD}(z)H_d(z, v_c)$. Due to its tight connection with the logistic sigmoid, as shown in the previous section, we choose $H_d(z, v_c) = H_{d,2}(z, v_c) = H(v_c - \Re(z))$. Consequently, $Z_{SD}(z)$ is discontinuous at $|\Re(z)| = v_c$ ($\Im(z) < 0$).

Is that it? Can we proceed exactly as the cut-off distribution case previously analysed? Unfortunately, no, because in this case $F'_{SD}(z)$ is not well defined either. $F'_{SD}(v)$ is given, for real v, as

$$F'_{SD}(v) = N\frac{-3|v|^2\mathrm{sign}(v)}{(|v|^3 + v_t^3)^2}. \tag{4.39}$$

At first glance, one might be tempted to replace $|v|$ with the absolute value $|z|$. However, functions of $|z|$ are nowhere analytical. $Z_{SD}(|z|)$ would be non analytical in the entire LHP, thereby preventing the application of the residue theorem in the LHP. A better choice is as follows:

$$F'_{SD}(z) = \begin{cases} N\dfrac{-3z^2}{(z^3 + v_t^3)^2}, & \text{if } \Re(z) \geq 0, \\ N\dfrac{3z^2}{(z^3 - v_t^3)^2}, & \text{if } \Re(z) < 0. \end{cases} \tag{4.40}$$

This definition introduces an additional discontinuity on the imaginary semiaxis at $\Re(z) = 0, \Im(z) < 0$. Such a choice is, of course, arbitrary, and the discontinuity could be positioned at a different angle in the LHP. The important element is that we need to integrate around such discontinuity when computing the electric field.

We are then ready to predict the structure of the poles:

- $0 < \Re(z) < v_c, \Im(z) < 0$: F'_{SD} has three singularities of order 2, $z_m = v_t e^{i\pi/3+2m\pi/3}$. Among these, only z_2 is located in the selected region. We then expect a 4 lobe structure centered on z_2. Such a structure will be then cut by the discontinuities at $\Re(z) = 0, v_c$. At large k, we will have 2 poles around z_2. As k decreases, the curves $k = Z_{SD}(z)$ move further from the singularity and may eventually be cut by the discontinuities, leading to the possible disappearance of such poles.
- $-v_c < \Re(z) < 0, \Im(z) < 0$: Because of symmetry, same as the case $0 < \Re(z) < v_c, \Im(z) < 0$.
- $|\Re(z)| > v_c$: two symmetric stable poles are present, because of the null gradient region at $|v| > v_c$.

Fig. 4.14 shows the real part of $Z_{SD}(z)$ and the absolute value of the corresponding $\epsilon_{k'}(z)$, for $k' = 1$, $v_c = 3$, and $v_t = \sqrt{2}$. As it can be seen, the discontinuity on the imaginary axis cuts the $Z_{SD} = 1$ curve and removes one of the two poles associated to the singularity z_2. Analytical expressions for Z_{SD} are available and given in Extra C.

Naturally, the dominant contribution at long times is always provided by the stable poles at $|\omega/k| > v_c$.

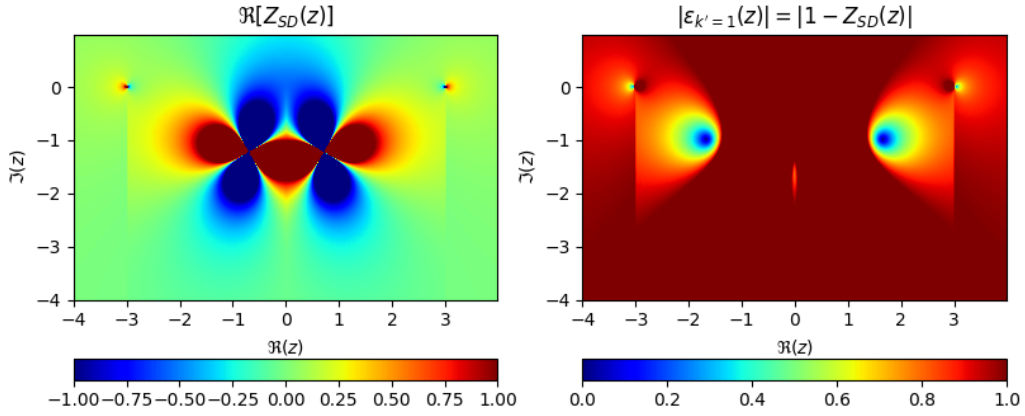

Figure 4.13: Real part of $Z_{SD}(z)$ and absolute value of the dielectric tensor $\epsilon_{k'}(z) = 1 - Z_{SD}$. Notice the LHP discontinuities at $\Re(z) = 0, \pm v_c$. $v_c = 3$

4.4.2 Smoothing out the Slowing-Down Distribution

In the preceding section, we showed how the integral around the discontinuity lines can be conveniently decomposed into a sum of sigmoid residues. Since the slowing-Down distribution includes the 'window' function H_d, it is obvious that we can proceed analogously as before to smooth out the edges of $f_{SD}(v)$. By means of two logistic sigmoids, the discontinuities at $\Re(z) = \pm v_c$ are eliminated. Such smoothing can be naturally interpreted as the edge-mitigating effect of collisions, and it is often already included in the Slowing-Down definition. However, because of previous observations, we adopt the logistic sigmoid instead of the erf sigmoid, that is instead typically adopted in the literature [35].

We now wonder about the other discontinuity, the one at $\Re(v) = 0$. Can we express it as a sum of poles? The answer is yes, and the following series of identities accomplishes the task:

$$|v| = v \cdot \text{sign}(v) = v \cdot [2H(v) - 1] \approx v \cdot [2\sigma_\beta(v) - 1] \tag{4.41}$$

As a result, the smoothed Slowing-Down can be expressed as

$$f_{SD,smooth} = N\sigma_\alpha(v - v_c) \cdot \left\{ [2\sigma_\beta(v) - 1]^3 + v_t^3 \right\}^{-1} \cdot \sigma_\alpha(-v + v_c) \tag{4.42}$$

While smoothing the $f_{SD}(v)$ edge at $v = \pm v_c$ has a direct physical interpretation, the discontinuity induced by $|v|$ is more subtle and yet mysterious. It does not manifest on the real axis, where the function is infinitely differentiable at $v = 0$, but only in the LHP. As far as the author knows, such a discontinuity has not been considered in the literature, and it thus requires further investigation. Moreover, while the α parameter for the $v = v_c$ smoothing could be easily determined through comparison with existing literature, the β parameter remains an unknown.

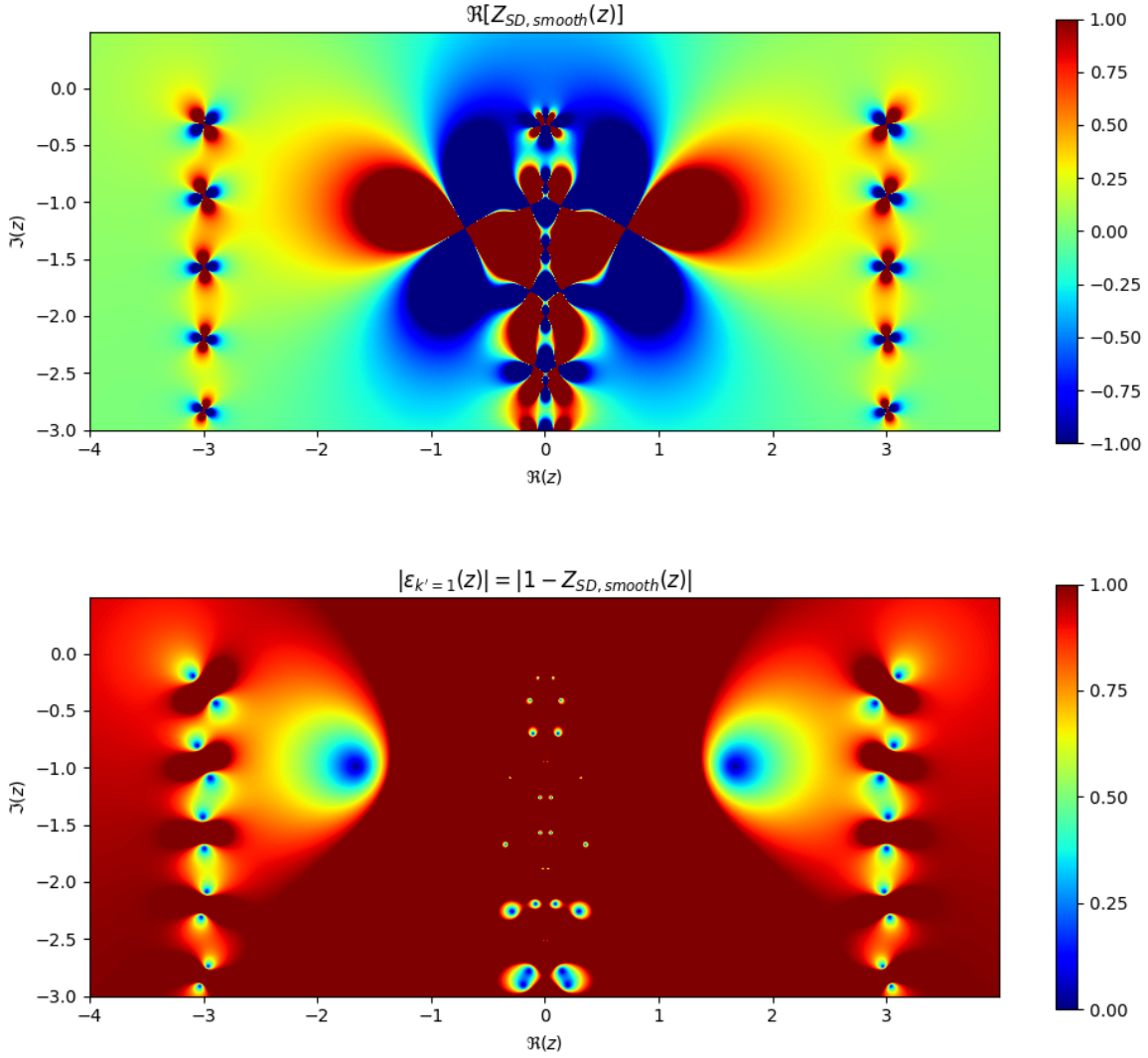

Figure 4.14: Real part of $Z_{SD,smooth}(z) = Z(z, f'_{SD,smooth})$ and absolute value of the dielectric tensor $\epsilon_{k'}(z) = 1 - Z_{SD,smooth}$. Compare to Fig. 4.14 and notice how the discontinuities have been replaced via logistic sigmoids by a continuous structure and a multiplicity of new poles.

In Figs. 4.14 we can observe $Z_{SD,smooth}(z) = Z(z, f'_{SD,smooth})$ and the associated dielectric tensor for the smoothed Slowing-Down. We set $k' = 1$, $\alpha = \beta = 0.1$, $v_c = 3$ and $v_t = \sqrt{2}$. Note the new poles resulting from the smoothing of the absolute value $|v|$. It is worth noticing

that the pole with smallest damping does not necessarily belong to the $\Re(Z) = v_c$ sigmoid poles, but it may belong to the $\Re(Z) = 0$ ones. Finally, in Fig. 4.15, we show the electric field reconstruction in the time interval $[10, 15]$. Given the similar damping coefficients, both the smallest damping poles, the two close to $\Re(z) = 0$ and the two close to $\Re(z) = \pm v_c$ are significantly contributing to the total electric field.

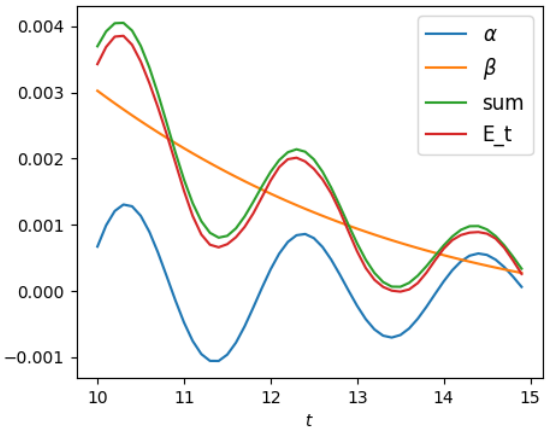

Figure 4.15: Electric field solution for the case $f_0(v) = f_{SD,smooth}(v)$. α represents the residue contribution from the two (symmetric) smallest damping poles close to $\Re(z) = \pm v_c$, α represents the residue contribution from the two (symmetric) smallest damping poles close to $\Re(z) = \pm 0$. 'sum' stands for the sum $\alpha + \beta$, and E_t corresponds to the electric field computed via direct integration.

4.5 κ Distributions with Non-Integer κ

As we have observed for the Slowing-Down case with $|v|$, discontinuities lines in the LHP description do not exclusively emerge when dealing with the Heaviside step function. Here, we briefly mention the case of κ distributions with a non-integer values of κ. The specific issue is tightly bound to a common aspect of complex non-integer powers, namely their multivaluedness, that requires the introduction of branch cuts.

A typical non-integer κ distribution features a branch cut discontinuity, as can be seen in Fig. 4.16, that we can conveniently locate on the imaginary axis, with $\Im(z) < \Im(z_\kappa)$, where z_κ is the singularity of the complex variable function $f'_\kappa(z)$. In our brief investigation, we did not discover a means to smooth out this discontinuity and replace it with a sum of poles. However, considering the general structure of the κ distribution dielectric tensor, Sec. 3.1, we expect that at least two poles at $Im(z) > \Im(z_\kappa)$ are present. Consequently, since we positioned the discontinuity at $\Im(z) < \Im(z_\kappa)$, we could imagine it to be the sum of contributions of poles with damping γ') , and their contribution at long times can be neglected in comparison to the poles at $Im(z) > \Im(z_\kappa)$.

As an additional point of interest, we mention that the number of poles in the non-integer κ case amounts to floor$[\kappa + 1]$.

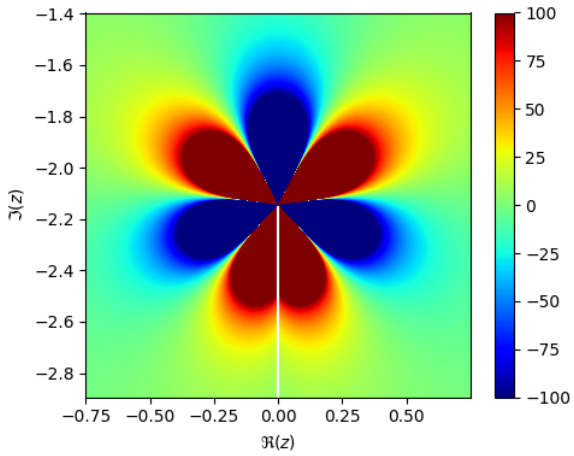

Figure 4.16: Real part of $Z(z, f'_{\kappa=2.4})$. The white line represents the discontinuity line $[-i\infty, -i\sqrt{\kappa v_t^2}]$.

Extra A: Analytical Expressions for Cut-Off $\kappa = 1$ Distribution

We here provide the analytical expressions for the three different analytical continuations of Eq. (4.18). Let us start by defining the function in the upper half plane. By simply plugging in $F_0 = N\frac{1}{(1+\frac{v^2}{v_t^2})^2}$ into Eq. (4.4), we get:

$$Z_{UHP}(z, f'_{\kappa=1}) = N \cdot \frac{2}{\pi(v_t^2+z^2)^2} \times \left(-\frac{v_c v_t(v_t^2+z^2)}{v_c^2+v_t^2} - (-v_t^2+z^2)\arctan\left(\frac{v_c}{v_t}\right) + v_t z(-\text{log\_func}(z, v_c))\right) \tag{4.43}$$

$$+ F_0(v_c)\frac{2v_c}{z^2-v_c^2} \tag{4.44}$$

where log_func(z, v_c) is defined as $\log(v_c - z) - \log(-v_c - z)$. To define Z in the remaining part of the complex plane, we can proceed in two ways, we either follow directly Eq. (2.22) or we focus on the log_func function and analyse its branch cuts. We will follow the first method for the slowing down, here we follow the second method. Let us then consider

$$\text{log\_func}(z, v_c) = \log(v_c - z) - \log(-v_c - z) \tag{4.45}$$

where $\log(x) = \log(|x|) + i\theta_x$ is the complex logarithm. When defining θ a specific branch cut must be chosen. The numpy function 'np.angle' returns a value in the range $[-\pi, \pi]$. According to this definition, it can be verified log_func will be discontinuous on the real axis in between $-v_c$ and v_c. Nothing forbids to choose other Riemann sheet for the logarithm. Let us take: $\log 1(x)$ such that $\theta_1 \in [-\pi/2, \pi/2]$ and $\log 2(x)$ such that $\theta_2 \in [0, 2\pi]$. And we than define:

$$\begin{aligned} \text{log\_func}_0(z, v_c) &= \log(v_c - z) - \log(-v_c - z) \\ \text{log\_func}_1(z, v_c) &= \log 1(v_c - z) - \log 1(-v_c - z) \\ \text{log\_func}_2(z, v_c) &= \log(v_c - z) - \log 2(-v_c - z) \end{aligned} \tag{4.46}$$

It is easy to verify that log_func$_1$ is discontinuous on the lines $\Re(z) = \pm v_c, \Im(z) < 0$, and log_func$_2$ on the real axis, at $|\Re(z)| > v_c$. By plugging in the different definitions for log_func$_i$, it is easy to verify that we get the analytical expression for Z_0, Z_1 and Z_2 from Eq. (4.15). Such an approach hence gives a further mathematical interpretation of the ambiguity of the LHP description in terms of branch cuts of the complex logarithm.

Extra B: Plots with Error Function Sigmoid

We provide the plots mentioned in Subsection 4.3.1 for the GPDF of $f'^{erf}_{\kappa=1,\alpha}$, where

$$f^{erf}_{\kappa,\alpha}(z) = N(\alpha)\sigma_{erf,\alpha}(z + v_c)\frac{1}{v^2+v_t^2}\sigma_{erf,\alpha}(-z + v_c). \tag{4.47}$$

In particular, in Fig. 4.17 we plot the real part of $Z(z, f'^{erf}_{\kappa=1,\alpha})$, for two different values of α. These values are chosen so that $\sigma_{erf,\alpha}(v)$ approximately matches $\sigma_{log,\alpha}(v)$ with the α values of Subsection 4.3.1, as shown in Fig. 4.7. We observe that, compared to the left plots of Figs. 4.9 and 4.10, the structure is significantly more complicated. Moreover, for the $\alpha = 0.05$ case overflow occurs and prevents the numerical scheme from returning values.

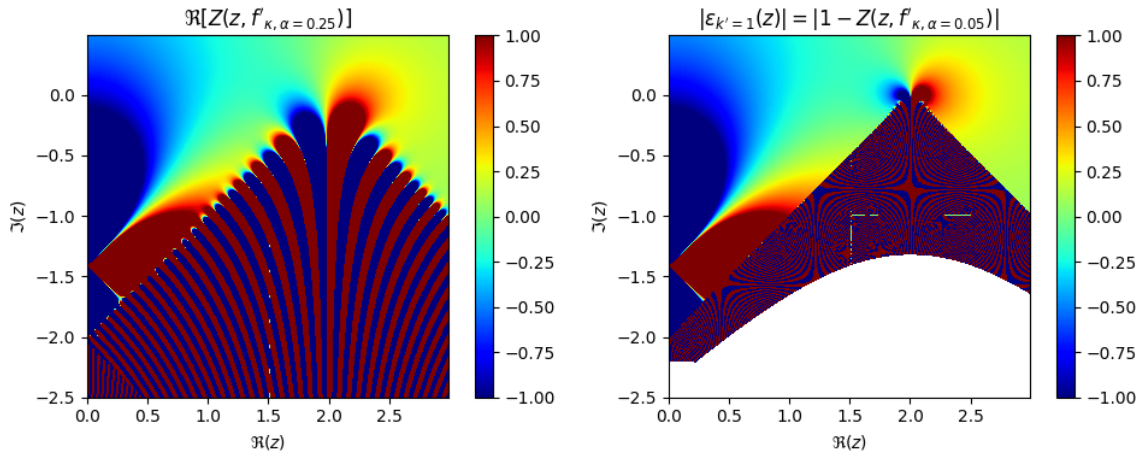

Figure 4.17: Real part of $Z(z, f'^{erf}_{\kappa=1,\alpha=0.25})$ and $Z(z, f'^{erf}_{\kappa=1,\alpha=0.05})$, where erf sigmoids are used. The white region corresponds the values of z for which overflow occurred.

Extra C: Analytical Expressions for Slowing-Down

The Slowing-Down distribution function is defined as

$$F_{SD}(v) = N \frac{1}{|v|^3 + v_t^3} H(v_c - |v|). \tag{4.48}$$

We also define

$$F_{SD,+}(v) = N \frac{1}{v^3 + v_t^3} H(v_c - |v|). \tag{4.49}$$

Normalization constant:

$$\begin{aligned}
\frac{1}{N} &= \int_{-\infty}^{\infty} F_{SD}(v)\mathrm{d}v \\
&= \int_{-v_c}^{0} \frac{1}{-v^3 + v_t^3}\mathrm{d}v + \int_{0}^{v_c} \frac{1}{v^3 + v_t^3}\mathrm{d}v \\
&= 2\int_{0}^{v_c} \frac{1}{v^3 + v_t^3}\mathrm{d}v \\
&= 2\int_{0}^{v_c} \frac{1}{(v + v_t)(v^2 - v_t v + v_t^2)}\mathrm{d}v \\
&= 2\int_{0}^{v_c} \left[\frac{A}{v + v_t} + \frac{Bv + C}{v^2 - v_t v + v_t^2}\right]\mathrm{d}v \\
&= \frac{2}{3v_t^2}\int_{0}^{v_c} \left[\frac{1}{v + v_t} + \frac{-v + 2v_t}{v^2 - v_t v + v_t^2}\right]\mathrm{d}v \\
&= \frac{2}{3v_t^2}\int_{0}^{v_c} \left[\frac{1}{v + v_t} - \frac{1}{2}\frac{2v - v_t}{v^2 - v_t v + v_t^2} + \frac{1}{2}\frac{3v_t}{v^2 - v_t v + v_t^2/4 + 3v_t^2/4}\right]\mathrm{d}v \\
&= \frac{2}{3v_t^2}\int_{0}^{v_c} \left[\frac{1}{v + v_t} - \frac{1}{2}\frac{2v - v_t}{v^2 - v_t v + v_t^2} + \frac{2}{v_t}\frac{1}{1 + \left(\frac{v - v_t/2}{\sqrt{3}v_t/2}\right)^2}\right] \\
&= \frac{2}{3v_t^2}\left[\ln(v + v_t) - \frac{1}{2}\ln(v^2 - v_t v + v_t^2) + \sqrt{3}\tan^{-1}\left(\frac{2v - v_t}{\sqrt{3}v_t}\right)\right]\Bigg|_0^{v_c}.
\end{aligned} \tag{4.50}$$

Generalized plasma dispersion function:

- Upper half-plane, $\Im(z) > 0$

$$Z(z, f'_{SD}) = \int_{-v_c}^{v_c} \frac{F'_{SD}(v)}{v - z} \mathrm{d}v + F_{SD}(v_c) \frac{2v_c}{z^2 - v_c^2}. \tag{4.51}$$

$$\begin{aligned} \int_{-v_c}^{v_c} \frac{F'_{SD}(v)}{v - z} \mathrm{d}v &= \int_0^{v_c} \frac{F'_{SD,+}(v)}{v - z} \mathrm{d}v + \int_0^{v_c} \frac{F'_{SD,+}(v)}{v + z} \mathrm{d}v \\ &= I(v_c, z) - I(0, z) + I(v_c, -z) - I(0, -z), \end{aligned} \tag{4.52}$$

where

$$I(v, z) = \int \frac{F'_{SD,+}(v)}{v - z} \mathrm{d}v = \frac{F_{SD,+}(v)}{v - z} + \frac{d}{dz} \int \frac{F_{SD,+}(v)}{v - z} \mathrm{d}v. \tag{4.53}$$

We then compute $U(v, z) = \int \frac{F_{SD,+}(v)}{v - z} \mathrm{d}v$

$$\begin{aligned} U(v, z) &= \int \frac{1}{(v^3 + v_t^3)(v - z)} \mathrm{d}v \\ &= \int \left[\frac{Av^2 + Bv + C}{v^3 + v_t^3} + \frac{D}{v - z} \right] \mathrm{d}v \\ &= -\frac{1}{v_t^3 + z^3} \int \left[\frac{v^2 + zv + z^2}{v^3 + v_t^3} - \frac{1}{v - z} \right] \mathrm{d}v \\ &= -\frac{1}{v_t^3 + z^3} \int \left[\frac{\alpha v + \beta}{v^2 - v_t v + v_t^2} + \frac{\gamma}{v + v_t} \right] \mathrm{d}v + \frac{\ln(v - z)}{v_t^3 + z^3} \\ &= -\frac{1}{v_t^3 + z^3} \int \left[\frac{\alpha(v - v_t/2)}{v^2 - v_t v + v_t^2} + \frac{\alpha v_t/2 + \beta}{v^2 - v_t v + v_t^2} \right] \mathrm{d}v + \frac{-\gamma \ln(v + v_t) + \ln(v - z)}{v_t^3 + z^3} \\ &= -\frac{1}{v_t^3 + z^3} \left[\frac{\alpha}{2} \ln(v^2 - v_t v + v_t^2) + (\frac{\alpha v_t}{2} + \beta) \frac{2}{\sqrt{3} v_t} \tan^{-1} \left(\frac{2v - v_t}{\sqrt{3} v_t} \right) \right. \\ &\qquad \left. + \gamma \ln(v + v_t) - \ln(v - z) \right], \end{aligned} \tag{4.54}$$

with $\alpha = \frac{1}{3v_t^2}(2v_t^2 + zv_t - z^2)$, $\beta = \frac{1}{3v_t}(-v_t^2 + zv_t + 2z^2)$, $\gamma = \frac{1}{3v_t^2}(v_t^2 - zv_t + z^2)$.

By taking the derivative of $U(v, z)$ w.r.t z, and by adding $F_{SD,+}(v)/(v - z)$, we obtain $I(v, z)$

$$\begin{aligned} I(v, z) = (&\frac{-6t^2(v^2 + vz + z^2)}{(t^3 + v^3)(z^3 + t^3)} + \frac{2\sqrt{3}(-t^2 + z^2) \arctan\left(\frac{-t/2 + v}{\sqrt{3}t/2}\right)}{(t^2 - tz + z^2)^2} + \frac{2 \log(t + v)}{(z + t)^2} \\ &- \frac{t^2 - 4tz + z^2}{(t^2 - tz + z^2)^2} - \frac{18t^2 z^2 \log(v - z)}{(z^3 + t^3)^2}) / (6t^2), \end{aligned} \tag{4.55}$$

so that the final expression is

$$Z_{UHP}(z, f'_{SD}) = I(v_c, z) - I(0, z) + I(v_c, -z) - I(0, -z) + F_{SD}(v_c) \frac{2v_c}{z^2 - v_c^2}. \tag{4.56}$$

- Lower half-plane: we choose the complex extension with a discontinuity on $\Re(z) = \pm v_c, \Im(z) < 0$. We then have:

$$Z_{LHP}(z) = [Z_{UHP}(z^*)]^* + 2\pi i F'_{SD} H(v_c - |\Re(v)|). \tag{4.57}$$

- Real axis: for the real axis we take $Z_{UHP}(v)$ when $v < 0$ and $Z_{LHP}(v)$ when $v > 0$. This choice is related to the definition of the NumPy function 'np.angle', that is called when evaluating complex logarithms.

Intermezzo

Chapter 5

Xie's Algorithm

In the previous chapters, we showed that determining the roots of the dispersion relation

$$\epsilon(p,k) = 1 - \frac{\omega_p^2}{k^2}\int_{LC}\frac{\partial f_0(v)/\partial v}{v-p/k}\mathrm{d}v = 0 \tag{2.21}$$

is the key point for the description of the linear Vlasov-Poisson dynamics. Typically, for a generic distribution function, the integral in the dispersion relation does not admit analytical expressions. Therefore, a numerical scheme for calculating the Landau integral is crucial. In this chapter, we revisit the one-solve-all approach from [5] and, after presenting and explaining the various steps of the numerical scheme, we expand on the original paper by carrying out an error analysis. The error analysis will lead us to outline a simple strategy to adopt when better accuracy is desired. We point out that Xie implemented the original numerical scheme in Matlab [36]. In the context of the present project, we implemented, tested, and analyzed the numerical scheme using the Python language.

5.1 The Algorithm

We begin by recalling the definition for the generalized plasma dispersion function (GPDF), defined as

$$Z(z,F) = \int_{LC}\frac{F(v)}{v-z}\mathrm{d}v = \begin{cases}\int_{-\infty}^{\infty}\frac{F(v)}{v-z}\mathrm{d}v, & \Im(z)>0,\\ \mathrm{P.V.}\int_{-\infty}^{\infty}\frac{F(v)}{v-z}\mathrm{d}v + i\pi F(z), & \Im(z)=0,\\ \int_{-\infty}^{\infty}\frac{F(v)}{v-z}\mathrm{d}v + 2i\pi F(z), & \Im(z)<0.\end{cases} \tag{2.22}$$

The aim of the numerical scheme is to compute $Z(z,F)$ for any input distribution function F.

From a practical standpoint, we are essentially dealing with an algorithm for computing the Hilbert transform of a generic function F, which is nothing more than a rescaled GPDF,

$$Z(z,F) = \pi HT(z,F). \tag{5.1}$$

5.1.1 One-solve-all Approach

Let us assume that the function F can be expressed as:

$$F(v) = W(v)\sum_{n=-\infty}^{\infty} a_n\rho_n(v),^{1} \tag{5.2}$$

[1] If the function is square-integrable, then the decomposition onto an orthogonal basis is justified through the Fourier theorem.

where $\{\rho_n(v)\}$ is an orthogonal basis set with weight function $W(v)$, satisfying the orthogonality relation

$$\int_{-\infty}^{\infty} W(v)\rho_n(v)\rho_m^*(v)\mathrm{d}v = A\delta_{m,n}, \tag{5.3}$$

and where the coefficients a_n are given by

$$a_n = \frac{1}{A}\int_{-\infty}^{\infty} F(v)\rho_n^*(v)\mathrm{d}v. \tag{5.4}$$

We choose the set of basis functions

$$\rho_n = \frac{(L+iv)^n}{(L-iv)^n}, \tag{5.5}$$

that, after the transformation $v = L\cdot tan(\theta/2)$, correspond to the exponential basis $\rho_n(v(\theta)) = e^{in\theta}$. Moreover, from the orthogonality relation (5.3) we find that $A = \pi/L$. With the definitions provided, we proceed by recasting GPDF in the UHP as

$$\begin{aligned} Z_{UHP}(z,F) &= \int_{-\infty}^{\infty}\frac{F\,(v)}{v-z}\mathrm{d}v = \int_{-\infty}^{\infty}\frac{W(v)\sum_{n=-\infty}^{\infty}a_n\rho_n(v)}{v-z}\mathrm{d}v \\ &= \sum_{n=-\infty}^{\infty} a_n\int_{-\infty}^{\infty}\frac{W(v)}{v-z}\frac{(L+iv)^n}{(L-iv)^n}\mathrm{d}v. \end{aligned} \tag{5.6}$$

Using residues and remembering $\Im(z) > 0$ yields (calculations below),

$$\int_{-\infty}^{\infty}\frac{W(v)}{v-z}\frac{(L+iv)^n}{(L-iv)^n}\mathrm{d}v = \begin{cases} \frac{i\pi}{L}\frac{1}{(L-iz)}, & n=0, \\ \frac{2i\pi}{L^2+z^2}\frac{(L+iz)^n}{(L-iz)^n}, & n>0, \\ 0, & n<0. \end{cases} \tag{5.7}$$

and the GDPF in the UHP can be expressed as

$$Z_{UHP}(z,F) = \frac{2i}{L^2+z^2}\sum_{n=1}^{\infty}a_n\frac{(L+iz)^n}{(L-iz)^n} + \frac{ia_0}{L(L-iz)}. \tag{5.8}$$

For the lower half-plane, we make use of Z_{UHP} itself to express Z_{LHP} through the following identity:

$$\begin{aligned} Z_{LHP}(z) &= \int_{-\infty}^{\infty}\frac{F(v)}{v-z}\mathrm{d}v + 2i\pi F(z) \\ &= \left[\int_{-\infty}^{\infty}\frac{F(v)}{v-z^*}\mathrm{d}v\right]^* + 2i\pi F(z) \\ &= [Z_{UHP}(z^*)]^* + 2i\pi F(z) \end{aligned} \tag{5.9}$$

Finally, for the real axis, we observe that the limit of Z_{UHP} as $\Im \to 0$ is well-defined, and we thus use the same expression for Z_{UHP} along the real axis. In summary, we have

$$Z(z,F) = \begin{cases} Z_{UHP}(z) = \frac{2i}{L^2+z^2}\sum_{n=1}^{\infty}a_n\frac{(L+iz)^n}{(L-iz)^n} + \frac{ia_0}{L(L-iz)}, & \Im(z)\geq 0, \\ [Z_{UHP}(z^*)]^* + 2i\pi F(z), & \Im(z) < 0. \end{cases} \tag{5.10}$$

Integrals of Eq. (5.7)**:** Three cases are distinguished:

- $n > 0$: two poles, $v = z$ (simple pole) in the UHP and $v = -iL$ (order $n+1$) in the LHP. Therefore, we close the real axis contour with an infinite radius semicircle in the UHP, and we apply the residue theorem:

$$\begin{aligned}\int_{-\infty}^{\infty} \frac{W(v)}{v-z}\frac{(L+iv)^n}{(L-iv)^n}\mathrm{d}v &= 2\pi i\ Res\{f(v=z)\} \\ &= 2\pi i \lim_{v\to z}\left[\frac{1}{L^2+v^2}\frac{(L+iv)^n}{(L-iv)^n}\right] \\ &= \frac{2\pi i}{L^2+z^2}\frac{(L+iz)^n}{(L-iz)^n}.\end{aligned} \tag{5.11}$$

- $n = 0$: three simple poles, $v = z$ and $v = iL$ in the UHP, $v = iL$ in the LHP. We then close the real axis contour with an infinite radius semicircle in the LHP, and we apply the residue theorem:

$$\begin{aligned}\int_{-\infty}^{\infty} \frac{W(v)}{v-z}\frac{(L+iv)^n}{(L-iv)^n}\mathrm{d}v &= 2\pi i\ Res\{f(v=-iL)\} \\ &= 2\pi i \lim_{v\to -iL}\left[\frac{1}{(v-z)(v-iL)}\right] \\ &= \frac{\pi i}{L}\frac{1}{(L-iz)}.\end{aligned} \tag{5.12}$$

- $n < 0$: two poles, $v = z$ (simple pole) and $v = iL$ (order $-n+1$), both in the UHP. Since no poles appear in the LHP, the residue theorem applied in the LHP directly implies that the integral (5.7) vanishes.

5.1.2 Implementation

Once Eq. (5.10) is given, the only complication left regards the computation of the coefficients a_n. The most practical way, exploiting the Fourier form of the introduced basis functions, makes use of the discrete Fourier transform. The functions `fft` and `fftshift` from the SciPy Discrete Fourier Transform package, and other `NumPy` standard functions are employed.

Let us consider Eq. (5.10) and let us plug in the function basis ρ_n,

$$a_n = \frac{L}{\pi}\int_{-\infty}^{\infty} F(v)\frac{(L-iv)^n}{(L+iv)^n}\mathrm{d}v. \tag{5.13}$$

We introduce the transformation $v = L\tan(\theta/2)$ to rewrite the integral as,

$$a_n = \frac{1}{2\pi}\int_{-\pi}^{\pi} F(v(\theta))(L^2+v(\theta)^2)e^{-in\theta}\mathrm{d}\theta, \tag{5.14}$$

and we then approximate it by means of the trapezoidal method. $2M$ sampling points $\theta_j = \pi j/M$ are selected, with j ranging from $-M$ to $M-1$:

$$a_n \sim A_n = \frac{1}{2M}\sum_{j=-M}^{M-1} F(v(\theta_j))(L^2+v(\theta_j)^2)e^{-in\theta_j}. \tag{5.15}$$

```
def GPDF(z,F,N,L):

    if L==None: L = np.sqrt(N/np.sqrt(2))

    M = 2*N
    M2 = 2*M
    k = np.arange(-M+1,M)
    theta = k*np.pi/M
    v = L*np.tan(theta/2)
    G = F(v)
    G[np.isnan(G)]=0

    W = (L**2+v**2)
    G = G*W
    G = np.insert(G,0,0)
    a = (fft(fftshift(G)))/M2
    a0 = a[0]
    a = np.flipud(a[1:N+1])

    idx1=z.imag != 0;
    z1 = ((z[idx1].imag)>0)*z[idx1]+((z[idx1].imag)<0)*np.conj(z[idx1])
    t = (L+1j*z1)/(L-1j*z1)
    p = np.polyval(a,t)

    # Evaluate GPDF

    h = 1j*(2*p/(L-1j*z1)**2+(a0/L)/(L-1j*z1))

    # convert upper half-plane results to lower half-plane
    Z[idx1] = np.pi*h*(z[idx1].imag>0)+
              +np.pi*(np.conj(h)+delt*2j*Fz(z[idx1]))*((z[idx1].imag)<0)

    return Z
```

Algorithm 1: The numerical GPDF

Evaluating $G(\theta) \equiv F(v(\theta))(L^2 + v(\theta)^2)$ at $\theta = -\pi$ gives rise to an uncertainty form $0 \times \infty$. We limit ourselves to well-behaved functions such that $G(\theta = -\pi) = 0$. However, to avoid calculator-risky multiplications between 0 and ∞, we evaluate $G(\theta)$ only for θ_j ranging from $-\pi + 1/M$ to $\pi - 1/M$ ($2M - 1$ points) and we later add $f(\theta = -\pi) = 0$ to the array $G(v(\theta_j))$ (line 16 in Algorithm 1).

We then exploit the periodicity of $v(\theta) = v(\theta + 2\pi)$ and $e^{in\theta} = e^{in\theta + 2in\pi}$ to recast the approximated coefficients as

$$\begin{aligned} A_n =& \frac{1}{2M} \sum_{j=-M}^{-1} f(v(\theta_j))(L^2 + v(\theta_j)^2) e^{-in\theta_j} + \frac{1}{2M} \sum_{j=0}^{M-1} f(v(\theta_j))(L^2 + v(\theta_j)^2) e^{-in\theta_j} \\ =& \frac{1}{2M} \sum_{j=0}^{M-1} f(v(\theta_j))(L^2 + v(\theta_j)^2) e^{-in\theta_j} + \frac{1}{2M} \sum_{j=M}^{2M-1} f(v(\theta_j))(L^2 + v(\theta_j)^2) e^{-in\theta_j} \end{aligned} \tag{5.16}$$

If G_j is the array given by the evaluation of $G(\theta)$ at $\{\theta_j = \pi j/M\}_{j=-M,\dots,M-1}$, $\texttt{fftshift}(FF_j)$ returns the function evaluations at $\{\theta_j = \pi j/M\}_{j=0,\dots,2M-1}$, and the last equality becomes:

$$\begin{aligned} A_n =& \frac{1}{2M} \sum_{j=0}^{2M-1} \texttt{fftshift}(G_j) e^{-in\theta_j} \\ =& \frac{1}{N} \sum_{j=0}^{N-1} \texttt{fftshift}(G_j) e^{-in2\pi j/N} \qquad \text{(SciPy notation, N=2M)} \\ =& \frac{1}{2M} \texttt{fft}\{\texttt{fftshift}(G_j)\} \end{aligned} \tag{5.17}$$

The algorithm finally returns the N coefficients A_n we are looking for, with $n = \{0, 1, ..., 2M-1\}$. Z_{UHP} will be then obtained by plugging in such coefficients into Eq. (5.10). At this stage, the function `np.polyval` will be used to evaluate the sum, and because of the definition of `np.polyval` itself in the SciPy library, an inversion through `np.flipud` in the element order of the array A_n with $n = \{1, ..., N-1\}$ has to be performed.

A Different Basis for the Real Axis

In the numerical scheme just introduced, a minor modification has been applied in comparison to the original scheme from [5]. Specifically, in contrast to our version of the scheme, where Z_{Real} and Z_{UHP} share the same definition, as per Eq. (5.10), the original paper introduces a separate basis set of functions for the real axis. This particular choice results in a different expression for the numerical GPDF when $\Im(z) = 0$. Through the error analysis of the next section, we will demonstrate that the choice made in the original paper is not justified.

5.1.3 Root Finder Algorithm

After establishing a method for computing the GPDF, the next step involves solving the dispersion relation, as per Eq. (2.21). In practice, when a fixed normalized wave vector k' is given, we look for the roots z_n of the dielectric tensor[2]. These roots z_n satisfy the equation

$$\epsilon(k', z_n) = k'^2 - \frac{v_t^2}{2} Z(z_n, f_0') = 0, \tag{5.18}$$

[2]For convenience, we use the normalized version of the dielectric tensor, introduced in Sec 3.0.1

where $f_0(v)$ represents the equilibrium distribution function. From the definition of z_n, $\frac{p'_n}{k'}\frac{v_t}{\sqrt{2}}$, we can easily calculate $p'_n = \omega'_n + i\gamma'_n$.

In the present work, we employed two distinct methods to determine the value of z_n: a graphical approach and a numerical one.

- **Graphical method**: We represent the absolute value of the dielectric tensor $\epsilon_{k'}(z)$ by using a colour plot, where the the magnitude of $|\epsilon(z)|$ is represented with a color scale. The roots are identified as distinct spots (blue in our case) on such a colour plot. By restricting the plotting region around the target root, and by adjusting the colour scale, we can pinpoint the values of z_n with sufficient precision. The use of an interactive plot, which allows us to place the cursor and obtain its coordinates on the plot, proves extremely helpful.

  While being painfully manual, this method ensures complete control over the specific root we wish to determine; and there is no danger that one root is mistaken for another.

- **Numerical method**: we utilize the SciPy function `optimize.root`, with $|\epsilon_{k'}(z)|$ as the input function. While this method is more automated, is has a significant limitation: it requires an initial guess. If our goal is to identify multiple roots — or one among many — we would need to be careful when providing the initial guess. Finding the right initial guess that leads to the desired solution is not trivial, and there is a tangible risk of identifying different poles as the same one.

Systematically finding the roots of the dispersion relation is not the primary focus of our current work. Aside from a few exceptions, we typically limit ourselves to showing plots of $|\epsilon_{k'}(z)|$. However, the root-finding process is definitely an important complementary aspect to this work, that requires further investigation and optimization. A possible approach to finding roots, based on drawing contours in the complex plane, is discussed in Ref. [4].

5.2 Error Analysis

In some cases, it is possible to compute the GPDF analytically or to express it using well-known functions. We exploit these cases as comparison terms to test the introduced numerical scheme. The error analysis aims to:

- Quantify the accuracy of the numerical scheme.
- Devise a simple strategy to improve accuracy.
- Justify the chosen real axis basis functions, which differ from those in the original scheme.

5.2.1 Maxwellian Distribution

As a first test case, we examine the Maxwellian distribution and the function $Z'_M(z) = Z(z, f'_M)$. Specifically, we compare the numerical computation, denoted as $Z_{M,Num}(z)$, with the reference result, $Z'_{M,Ref}$, computed in terms of the Faddeeva function (see Sec. 3.2 for details).

We quantify the error as:

$$\mathrm{err}_Z(z) = \frac{|Z'_{Ref}(z) - Z'_{Num}(z)|}{|Z'_{Ref}(z)|}. \tag{5.19}$$

The algorithm is very accurate in this case. Default parameters, such as $N = 32$ and $L = \sqrt{N/\sqrt{2}}$, ensure precision close to the computational precision, which is around 10^{-16} for

Python's '`float`' type. Fig. 5.1 shows the relative error $err_Z(z)$ along the real axis, for both the original scheme and our slightly modified version without the different basis for the real axis.

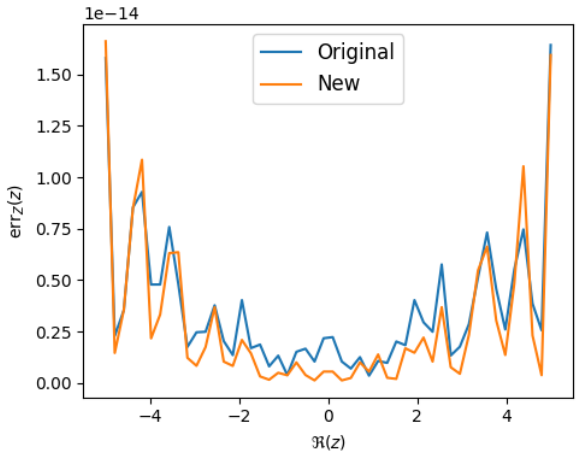

Figure 5.1: Relative error $err_Z(z)$ for the Maxwellian GPDF $Z'_M(z)$. No significative difference appears between the original and our modified (New) scheme. For the Maxwellian distribution used, $v_t = 1$.

5.2.2 κ Distribution

As a second test case, we consider the $\kappa = 1$ distribution, $f_{\kappa=1}(v)$. We numerically compute $Z'_1(z) = Z(k, f'_{\kappa=1})$ — denoting it as $Z'_{1,Num}$ — and compare it to the analytical expression

$$Z'_{\kappa,Ref}(z) = \frac{1}{(z + iv_t)^2}. \tag{5.20}$$

In this case, we solve the dispersion relation $|k'^2 - v_t^2 Z_\kappa(z)/2|$ to find the pole $\omega' + i\gamma'$, and we calculate the relative errors $\mathrm{err}_\omega(k')$ and $\mathrm{err}_\gamma(k')$:

$$\mathrm{err}_\omega(k') = \frac{|\omega'_{Num} - \omega'_{Ref}|}{\omega'_{Ref}}, \quad \mathrm{err}_\gamma(k') = \frac{|\gamma'_{Num} - \gamma'_{Ref}|}{\gamma'_{Ref}}. \tag{5.21}$$

As displayed in Fig. 5.2, the algorithm exhibits satisfactory accuracy for both ω' and γ'.

5.2.3 Cut-off κ Distribution

Lastly, we examine the cut-off $\kappa = 1$ distribution function, given by

$$f_{co}(v) = N(v_t, v_c) f_{\kappa=1}(v) H_d(v, v_c). \tag{5.22}$$

Again, we define $Z_{co,Num}(z)$ and $Z_{co,Ref}$ as the numerically and analytically computed $Z_{co}(z) = Z(z, f'_{co})$, respectively.[3]. In the present situation, the ambiguity in describing the LHP is not a concern, as the error is exclusively related to the integral term $\int f'_{co}/(v - z)\mathrm{d}v$ rather than the $2\pi i f'_{co}$ term. Furthermore, in the case of cut-off distributions, such integral term is singular on the real axis at $v = \pm v_c$. As a result, due to the divergence, the scheme becomes less accurate. In particular, the largest errors occur on the real axis, and these errors are significantly greater compared to the 'smooth' cases Maxwellian and $\kappa = 1$. Therefore, we

[3] Analytical formulas are given in Extra A of Chapter 4.

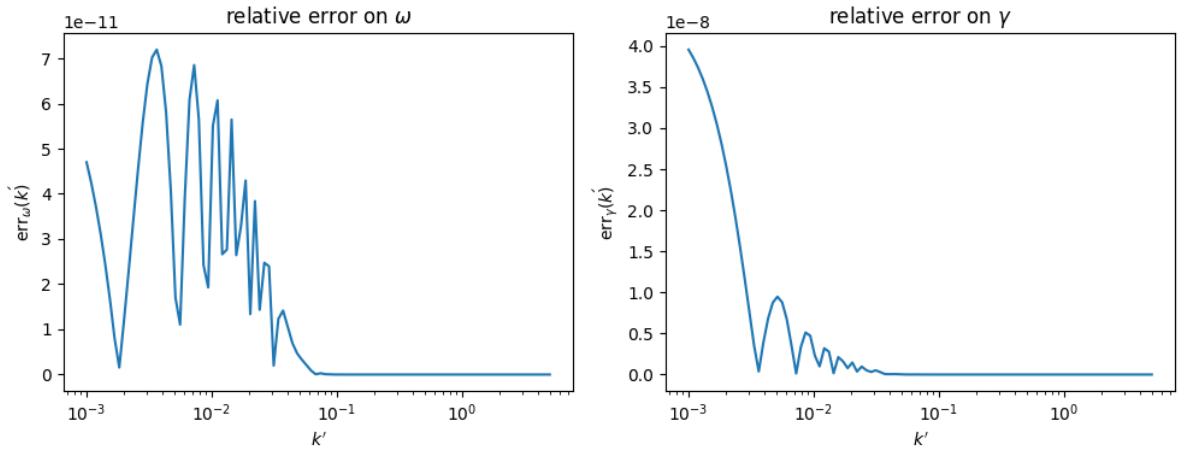

Figure 5.2: Relative error on ω' and γ', solution of the dispersion relation when $f_0 = f_{\kappa=1}$. The characteristic velocity v_t was set to $\sqrt{2}$.

focus our error analysis on the real axis, where the error is largest, and where no definition ambiguity exists.

To achieve satisfactory accuracy (typically we aim at relative errors on ω and γ smaller than 1/1000), we adjust the algorithm parameters L and N. Fig. 5.3 illustrates the sensitivity of the relative error, $err_{Z,co}(z) = |Z_{co,Num} - Z_{co,Ref}|/|Z_{co,Ref}|$, with respect to L and N. At fixed N (or L), the plotted relative error corresponds to the maximum value within a neighborhood of $z = v_c$. We observe that $err_{Z,co}(z)$ scales as $1/N$ and that the optimal L generally differs from the default value provided in the Xie's original algorithm.

In the same figure, the error sensibility for the original Xie's scheme is also displayed. Since the error determined by the original version tends to be larger than the error of the modified scheme, we argue that the use of a distinct basis for the real axis is not justified.

In our case ($v_t = \sqrt{2}$, and $v_c = 2$) the optimal L is around 3. It is important to note that the L parameter introduces a scale dependency into the scheme. Thus, the optimal L will depend, for instance, on the chosen velocity unit.

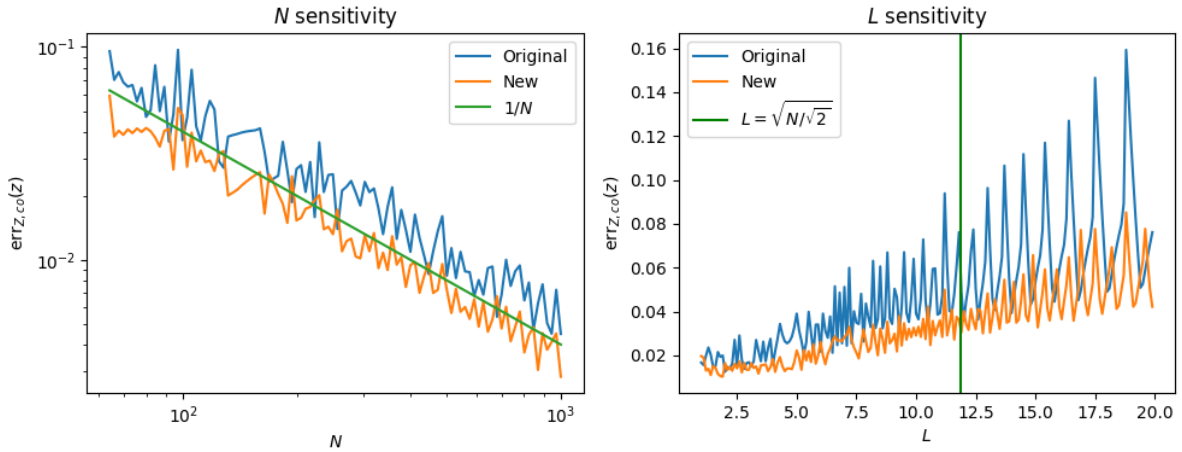

Figure 5.3: Sensitivity analysis for the cut-off κ distribution case ($v_t = \sqrt{2}$, $v_c = 2$). At fixed N (or L), the plotted error value corresponds to the maximum error in a neighborhood of v_c.

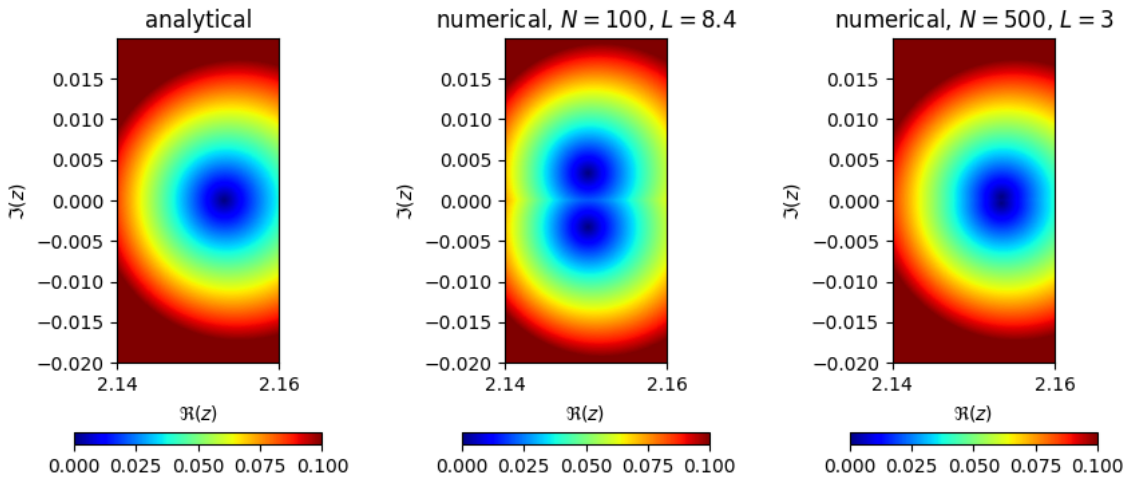

Figure 5.4: Representation of the 'rule of thumb' to improve the accuracy of the scheme.

The scheme's accuracy can be then enhanced through two methods: by increasing N or by varying L. However, unlike the option of increasing N, which prolong the computation time due to the calculation of more coefficients a_n, modifying the value of L does not incur longer computation times and is, therefore, a recommended approach.

Lastly, a useful and practical strategy to determine the values L and N for sufficient accuracy is suggested. Firstly, we observe that with default parameter values, and for the same cut-off $\kappa = 1$ distribution, two roots of the dielectric tensor $1 - Z_{co}(z))$ appear near the real axis. As we expect a single stable pole (corresponding to the stable pole of cut-off distributions), such double pole is evidently not physical and arises due to the numerical scheme's reduced accuracy along the real axis. Thus, our simple rule of thumb suggests that L and N suffice when the double pole disappears and we obtain a smooth-looking dielectric tensor $|\epsilon_{k'}(z)|$. In more accurate terms, L and N can be considered satisfactory when the separation between these 'numerical' poles is smaller than the desired level of accuracy. Fig. 5.4 depicts such double pole, and how it is eliminated through the optimization of L and N.

By slightly adjusting the parameters, satisfactory errors can be then achieved in the cut-off distribution case as well, as shown in Fig. 5.5. After solving the dispersion relation, we plot the damping coefficient γ' and the relative error $\mathrm{err}_{\omega'}(k')$ on ω' for the stable pole.[4]

[4]Since the reference value for a stable pole damping coefficient, γ', is zero, the relative error $\mathrm{err}_{\gamma'}$, as defined in Eq. (5.21), is here meaningless.

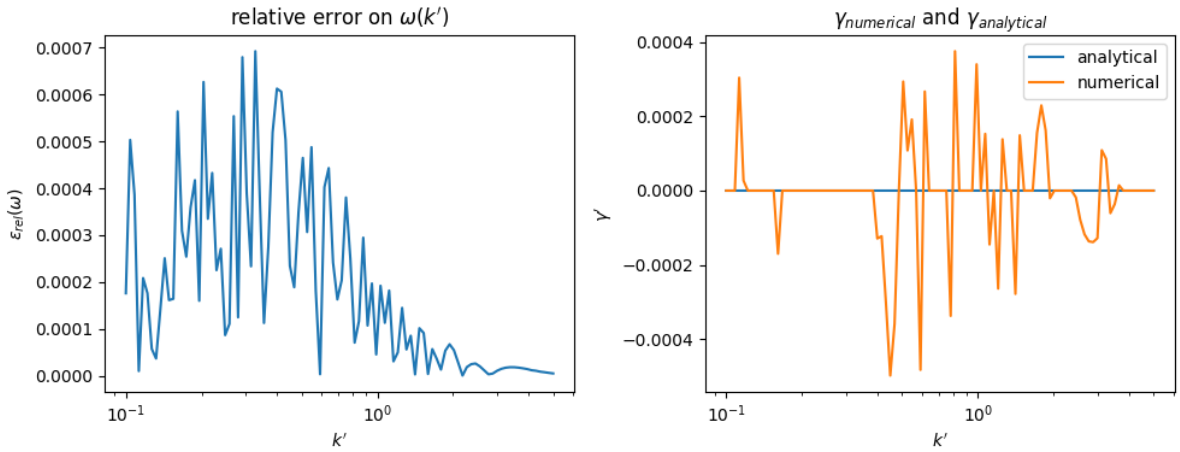

Figure 5.5: Error on ω' and γ' for the stable pole of the cut-off κ distribution. Chosen parameters: $v_t = \sqrt{2}$, $v_c = 2$. Since the reference value for γ' is zero, we plot the absolute value for γ'.

Part II

Application to the Fusion Relevant Theoretical Framework

Chapter 6

Energetic Particles (EPs) Physics: Introduction

After a long odyssey through the oceans of Landau damping, we finally reach the shore of the central task that motivated this master's thesis: the extension of the linear gyrokinetic dispersion relation for shear Alfvén waves to non-Maxwellian distribution functions. The present chapter aims at providing the necessary background, to reveal the meaning of the *'linear gyrokinetic dispersion relation for shear Alfvén waves'* and one possible scenario of application. We follow Ref [4].

6.1 EPs in Magnetically Confined Fusion Plasmas

Energetic Particles (EPs) are essential ingredients for magnetically confined fusion plasmas. Beyond the supra-thermal tails associated with external heating and current drive (neutral beam injection, electron and ion cyclotron resonance heating), the most notable example of EPs are α particles. αs are produced by the fusion reaction

$$ {}^{3}_{1}\mathrm{T} + {}^{2}_{1}\mathrm{D} \rightarrow \left({}^{4}_{2}\mathrm{He} + 3.5\mathrm{MeV}\right) + (n + 14.1\mathrm{MeV}) \tag{6.1} $$

and in the envisioned design for a fusion reactor they are supposed to be the main heating source for the background plasma. As fusion experiments approach ignition conditions, the plasma system will entail growing populations of αs and EPs, thereby raising interest regarding the stability and the efficiency of the EPs to background energy transfer process.

EPs transfer their energy to the background plasma mainly through collisions. Given the typically very long collision time between EPs and the plasma background, good confinement is imperative for the energy transfer. However, in certain cases excessive confinement time becomes undesirable; for instance helium ashes could accumulate in the core and dilute the D-T mixture, hence negatively affecting the performance of the plasma.

Studying the transport process is fundamental to understand whether EPs can deposit their energy in an efficient and stable way. EPs transport channels include classical and neo-classical transport, transport induced by the non-axisymmetry of the background magnetic field, turbulent transport, and resonant/non-resonant transport due to collective plasma waves and instabilities. In the core of a plasma, interactions of EPs with plasma waves and instabilities dominate the transport process.

Experimental and theoretical studies in tokamak plasmas have demonstrated a significant energy transfer from super-thermal particles to global Alfvén waves. This occurs when the periodic motion of energetic ions is in phase with the oscillation of weakly damped waves. As

a consequence, the energy stored in the EP's gradients can be transformed into wave energy: waves become unstable and grow, while EPs are transported from the hot core to the cold edge. Unstable modes triggered by EPs are noteworthy, as they might play a crucial role in stabilizing the turbulent behavior of a fusion plasma ([37], [34] and reference therein).

To describe the interaction of EPs and plasma waves, and more broadly the physics of EPs, hybrid MHD and kinetic models have been developed. Before describing such models, we briefly present the geometrical setting of the problem.

6.2 Tokamak Geometry

A tokamak is an experimental device designed for the magnetic confinement of low-density fusion plasmas. It features an axially symmetric toroidal magnetic field, comprising a toroidal field component B_t, generated by coils wound poloidally around the torus, and a poloidal field component B_θ, produced by the current flowing within the plasma. The superposition of B_θ and B_t shapes helical field lines, that suppress instabilities connected with a pure poloidal or pure toroidal configuration. The twist of the field lines as a function of the torus minor radius, $q(r)$, is defined as the ratio of the number of toroidal turns of a field line divided by the number of poloidal turns.

Depending on the ratio $v_\parallel/v_\perp$, charged particles may either be trapped on the low-field side of the tokamak, with $\theta_{min} < \theta < \theta_{max}$, or circulate with their poloidal angle θ increasing by 2π at every turn. This distinct particles behavior results from the fact that the absolute value of the magnetic field is not constant — $B_t \sim 1/R$, with R denoting the torus major radius — on a poloidal path around the plasma centre at $r = 0$. The trapped/passing distinction is based on the assumption of adiabaticity, i.e., the magnetic moment $\mu = mv_\perp^2/2B$ is an adiabatic invariant. In order for adiabaticity to hold, $r_g \ll |B/\nabla B|$ (gyro-radius much smaller than the gradient length of the background magnetic field), and $\dot{B}/B \ll \Omega_c$ (temporal variation of the magnetic field much smaller than the gyro-frequency), conditions that are easily fulfilled in the hot core of a tokamak plasma.

Energy conservation

$$const = E = \frac{1}{2}mv_\parallel^2 + \mu B \tag{6.2}$$

postulates that $v_\parallel$ has to be decrease in regions where B becomes larger. Accordingly, passing or transit particles maintain high parallel energy, ensuring $v_\parallel$ never reaches zero as B approaches its maximum on the particle trajectory. In contrast, particles with low parallel energy, whose $v_\parallel$ vanishes as B increases, experience periodic inversion in velocity direction, and remain trapped in the low B-field region.

For strongly passing and deeply trapped particles in a large aspect ratio $\epsilon = r/R$ tokamak with circular flux surfaces, the transit frequencies for passing (ω_p) and for trapped particles (ω_t) are given by

$$\omega_p \approx \frac{v_\parallel}{qR}, \quad \omega_t \approx \frac{v_\perp}{qR}\sqrt{\frac{r}{2R}}. \tag{6.3}$$

For thermal ions, these frequencies may often be too small to interact effectively with modes on the MHD scale. In an ITER-like scenario ($B = 5T, R = 6m, n_i = 5 \cdot 10^{19}/m^3$), the Alfvén frequency ($\omega_A = \sqrt{B^2/\mu_0 m_{DT} n_{DT}}/R \approx 10^6 s^{-1}$), used as a typical MHD modes timescale, is approximately $10^6 s^{-1}$, while the passing/trapped frequencies for thermal ions (15keV) are about one order of magnitude smaller ($4 \cdot 10^5 s^{-1}$ for trapped and $1 \cdot 10^5 s^{-1}$ for passing particles). But the situation changes when EPs are present, whose typical frequencies in the same scenario are approximately $4 \cdot 10^5 s^{-1}$ for trapped and $1 \cdot 10^5 s^{-1}$ for passing particles (for 660keV αs).

Additionally, ∇B and curvature drifts influence motion trajectories, causing the particles to deviate from their field line in both radial and perpendicular directions. The approximate width of such displacements for passing and trapped particles is expressed as

$$\rho_p \approx \frac{r}{R}\frac{v_\parallel}{\omega_{c\theta}}; \quad \rho_t \approx \frac{v_\parallel}{\omega_{c\theta}}; \quad \omega_{c\theta} = \frac{eB_\theta}{m}. \tag{6.4}$$

Furthermore, the circulating particle orbits and the turning points for trapped particles at $\theta_{min,max}$ exhibit a precessional motion (ω_{prec}) in the toroidal direction.

6.3 Models for EP Physics

This section offers a concise overview of the three models that can be applied to describe the physics of EPs: hybrid MHD, wave-kinetic theory and gyrokinetic theory. A closer look is taken into gyrokinetic theory, that corresponds to the framework of interest for the present work.

MHD (magnetohydrodynamics) is commonly the preferred model when studying large scale plasma stability phenomena. Its governing equations are derived from Vlasov equation by building moments over the velocity space, giving way to a fluid formulation. MHD is strictly justified only for plasmas dominated by collisions, where an isotropic pressure can be defined for each plasma 'fluid-element'. However, this postulate is never fulfilled in fusion plasmas, that exhibit strong anisotropy between the motion perpendicular and parallel to the magnetic field. While the Lorentz force effectively 'squeezes' particles together in the perpendicular direction, causing frequent collisions and enabling the concept of fluid elements, particles are free streaming in the parallel direction.

Consequently, ideal MHD can only be used when perpendicular dynamics is investigated. Nevertheless, it can be shown that for incompressible parallel modes with no pressure or density fluctuations, ideal MHD can be a valid model, even in the collisionless regime.

To include kinetic effects in the MHD frame, the pressure gradient ∇P is replaced by $\nabla(P + P_{hot})$ derived from kinetic equations. Such an approach, known as hybrid MHD, is only valid for small EP pressures.

To get more consistent equations, one has to resort to kinetic theory. Because of the complexity of the problem, achieving the full kinetic picture by solving the complete 6D Maxwell-Vlasov system in toroidal geometry is still not feasible. The system must be then simplified. Two possible approaches are: kinetic wave equations and gyrokinetics.

Kinetic wave equations are derived by linearizing Vlasov's equation, and describe the linear stability of waves with harmonic time dependence. The ansatz with harmonic time dependence allows formal integration over time and velocity space, and leads together with Maxwell's equations to a 'constitutive relation' (or a dielectric tensor) that describes the relation between current and electromagnetic fields. On the other side, gyrokinetics retains the full non-linearity of Vlasov equation, but reduces the dimensionality of the system from 6D to 5D. In other terms it decouples the fast gyromotion from the rest of the dynamics, allowing a description on time scales that are long compared to the gyromotion: $\epsilon = \omega/\Omega_{ci} \ll 1$.

The most rigorous approach to gyrokinetics involves the Langrangian/Hamiltionian field theory formulation. Following [38] and [35], we summarize the main steps towards the gyrokinetic equations.

- Lagrangian-perturbative formalism: The plasma species and fields are characterized by the total Lagrangian $L(\mathbf{x}, \mathbf{v})$, from which the Vlasov-Maxwell system can be derived by applying the variational principle:

$$\delta I = \delta \int L dt = 0. \tag{6.5}$$

The EM potentials are then split into an equilibrium and a perturbation component,

$$\phi = \phi_0 + \Delta\phi_1, \tag{6.6}$$

with Δ representing the ratio of the amplitudes of ϕ_0 and ϕ_1. This allows to rewrite the Lagrangian as the sum of an equilibrium and perturbation part, of the same order of Δ:

$$L(\mathbf{x}, \mathbf{v}) = L_0(\mathbf{x}, \mathbf{v}) + \Delta L_1(\mathbf{x}, \mathbf{v}),^{1} \tag{6.7}$$

- Guiding-center transformation: by exploiting $\epsilon = \rho/L_B$ as a smallness parameter (with ρ the gyroradius and $L_B = |\nabla B|/|B|$), the near-identity Lie transform

$$(\mathbf{x}, \mathbf{v}) \to (\mathbf{X}, U, \mu, \xi), \tag{6.8}$$

is applied. Up to first order of ϵ, we have: $\mathbf{X}$, position of the gyrocenter; U, parallel velocity; μ, magnetic moment; ξ, gyrophase. This transform allows the removal of the gyrophase dependency from the equilibrium Lagrangian:

$$\tilde{L}(\mathbf{X}, U, \mu, \xi) = \tilde{L}_0(\mathbf{X}, U, \mu) + \Delta\tilde{L}_1(\mathbf{X}, U, \mu, \xi). \tag{6.9}$$

- Gyrocenter transform: a canonical Lie transform is then employed,

$$(\mathbf{X}, U, \mu, \xi) \to (\bar{\mathbf{X}}, \bar{U}, \bar{\mu}, \bar{\xi}), \tag{6.10}$$

where the new gyrocenter coordinates $(\bar{\mathbf{X}}, \bar{U}, \bar{\mu}, \bar{\xi})$ are obtained by using the transform generating function. This transformation, carried out with Δ as the smallness parameter and by using the condition $\omega/\Omega_c \ll 1$ (ω_c is the cyclotron frequency), eliminates the gyrophase dependency from the perturbed Lagrangian:

$$\bar{L}(\bar{\mathbf{X}}, \bar{U}, \bar{\mu}, \bar{\xi}) = \bar{L}_0(\bar{\mathbf{X}}, \bar{U}, \bar{\mu}) + \Delta\bar{L}_1(\bar{\mathbf{X}}, \bar{U}, \bar{\mu}). \tag{6.11}$$

By applying the variational principle to the new, gyrophase independent Lagrangian, the gyrokinetic Maxwell-Vlasov system is derived. For explicit expressions, please refer to [38].

6.4 Shear Alfvén Linear Gyrokinetics

Although gyrokinetics reveals its full power for non-linear problems, the linearized version allows a systematic and elegant approach towards various stability considerations. For instance, linear gyrokinetics proves itself valuable because:

- If a mode spectrum is linearly stable, no transport is expected.
- Linear damping and growth are fundamental ingredients for quasi-linear theory [24], that is used as a reduced and sufficiently fast model to predict the transport of the background plasma.
- Subdominant linear modes can be excited non-linearly, and some linear properties can survive to some extent in the non-linear regime, especially in Alfvènic physics [39].

Based on the decomposition of the distribution function (for a generic species) into an equilibrium and a perturbed part,

$$F = F_0 + f, \tag{6.12}$$

linear gyrokinetics can be described by three equations: the linearized gyrokinetic Vlasov equation, the quasi-neutrality equation and the gyrokinetic moment equation [4].

[1] For illustrative purposes, we condense the Lagrangian perturbation $\Delta L_1 + \Delta^2 L_2$ from [38] into ΔL_1.

Linear Gyrokinetic Vlasov Equation: The linear gyrokinetic Vlasov equation, also known simply as gyrokinetic equation, is given as

$$\frac{\partial f}{\partial t} + \left(\bar{U}\mathbf{b} + \hat{\mathbf{v}}_d\right) \cdot \nabla f = \frac{\mathbf{b}}{eB} \cdot (\nabla F_0 \times \nabla H_1) + \frac{\partial F_0}{\partial E} \left(\bar{U}\mathbf{b} + \hat{\mathbf{v}}_d\right) \cdot \nabla H_1, \tag{6.13}$$

with

$$H_1 = eJ_0\left(\varrho k_\perp\right) \left(\phi(\mathbf{x}) - \frac{\bar{U}k_\parallel}{\omega}\psi(\mathbf{x})\right). \tag{6.14}$$

Here, f is the perturbed distribution function, F the equilibrium distribution. $\bar{U}$ is the parallel velocity in gyro-centre coordinates, $\mathbf{b}$ the unit vector in the direction of the magnetic field, $\hat{\mathbf{v}}_d = -\frac{\mathbf{b}}{eB} \times \left(m\bar{U}^2(\mathbf{b}\cdot\nabla)\mathbf{b} + \bar{\mu}\nabla B\right)$ is the drift velocity, and E the kinetic energy of particles. J_0 is the Bessel function of 0-th order. It takes into account the effect of finite Larmor radius and it is defined as an operator originating from gyro-averaging:

$$\frac{1}{2\pi}\int \mathrm{d}\xi e^{\pm\varrho\cdot\nabla} = \frac{1}{2\pi}\int \mathrm{d}\xi e^{\pm\varrho\nabla_\perp\cos\xi} = J_0\left(\frac{\varrho\nabla_\perp}{i}\right) = J_0\left(\varrho k_\perp\right), \tag{6.15}$$

with ϱ and ξ being the gyroradius and the gyrophase, respectively.

The perturbed potentials ϕ and ψ are defined via $\mathbf{E}_1(\mathbf{x}) = -\nabla\phi(\mathbf{x})$ and $A_\parallel(\mathbf{x}) = \left(\nabla\phi(x)\right)_\parallel/(i\omega)$. $A_\perp(\mathbf{x})$ is assumed to vanish, meaning that fluctuations in $\mathbf{B}_{1,\parallel}$ are neglected. This is consistent with the usual low-frequency ordering $\omega/\Omega_{ci} \ll 1$ and it means that compressional Alfvén waves are ordered out, thus retaining only shear Alfvén oscillations. The advantage of rewriting the equations in terms of ψ instead of $\mathbf{A}_\parallel$ is that it allows to split the linear gyrokinetic equations into an adiabatic part, dependent on $(\phi - \psi)$, and a non-adiabatic part. As the perturbed electric field is given as

$$E_{1\parallel} = -ik_\parallel(\phi - \psi), \tag{6.16}$$

the adiabatic part makes evident the connection to the ideal MHD limit. For stable Alfvén waves with negligible damping, no electric field is present and $\psi = \phi$, while at lower frequencies the Alfvén oscillation couples to electrostatic and acoustic waves and $\psi \neq \phi$.

Quasi-Neutrality Equation (QN): The quasi-neutrality equation corresponds to the linear gyrokinetic Poisson equation. By neglecting the polarisation terms coming from the back-transformation from the gyro-centre to particle coordinates [4], the QN equation can be expressed as

$$0 = \sum_a e_a n_{a1} = \sum_a e_a \int \mathrm{d}^2\mathbf{v}\left(J_0\left(\varrho\nabla_\perp\right) f\right)_a. \tag{6.17}$$

Here, the index a counts the particles species, n_{a1} stands for the perturbed density.

Gyrokinetic Moment Equation (GKM): The gyrokinetic moment equation completes the linear gyrokinetic system. It is derived by taking the 0-th order moment of the gyrokinetic equation and by using the linear Ampére and Poisson gyrokinetic equations. If we neglect β and 4-th order corrections [4], it is given as

$$\begin{aligned} &-\frac{\partial}{\partial t}\left[\nabla\frac{1}{v_A^2}\nabla_\perp\phi\right] + \mathbf{B}\cdot\nabla\frac{(\nabla\times\nabla\times A)_\parallel\cdot\mathbf{B}}{B^2} + \left(\mathbf{b}\times\nabla A_\parallel\right)\cdot\nabla\frac{\mu_0 j_{0\parallel}}{B} \\ &= -\sum_a \mu_0\int \mathrm{d}^2\mathbf{v}e_a\left(\hat{\mathbf{v}}_d\cdot\nabla J_0 f\right)_a + \sum_a \mathbf{b}\times\nabla\left(\frac{\beta_{a\perp}}{2\Omega_a}\right)\cdot\nabla\nabla_\perp^2\phi, \end{aligned} \tag{6.18}$$

where v_A is the Alfvén velocity, $\beta_{a\perp} = 2\mu_0 P_{a_\perp}/B^2$ is the perpendicular plasma β, and $j_{0,\parallel}$ is the parallel equilibrium current.

The first term represents the system inertia, while the second term the field line bending. Neglecting all other terms and using $\phi = \psi$ leads to the ideal shear Alfvén law: $\omega^2 = k_\parallel^2 v_A^2$.

The third term on the lhs and the first term on the rhs are essentially drive and/or damping terms due to current and pressure gradients.

The term $\sum_a \mathbf{b} \times \nabla \left(\frac{\beta_{a\perp}}{2\Omega_a}\right) \cdot \nabla \nabla_\perp^2 \phi$ can be rewritten for the background ions to be $\frac{i\omega_{pi}^*}{v_A^2} \nabla_\perp^2 \phi$ with $\omega_{pi}^* = \mathbf{b} \times \frac{\nabla(p_{i\perp})}{ieBn_i} \cdot \nabla$. It can be combined with the first term on the lhs to give the diamagnetic correction $\omega^2 \rightarrow \omega^2(1 - \omega_{pi}/\omega)$. The electron contribution vanishes due to the small electron mass, but there can be a contribution from the EPs, if their spatial pressure gradient is comparable to that of the background ions.

6.5 Turbulence, Geodesic Acoustic Modes (GAMs) and Energetic Particle Driven Geodesic Acoustic Modes (EGAMs)

In tokamak plasmas, turbulence is a widely observed phenomenon, fascinating but yet puzzling. Its onset can be interpreted as a growth-saturation cycle: a set of unstable modes (e.g., ITG ion temperature gradient) grow linearly as $exp(\gamma t)$ until they reach saturation via various mechanisms (e.g., non-linear spectral transfer or zonal flow excitation). The unstable mode stops growing, non-linear damping sets in and the mode is brought back into conditions for growth. Turbulence is a major hurdle on the road to burning plasma, as it involves high losses of energy, thus leading to a reduction in energy confinement time. Therefore, mitigation of turbulent transport is crucial for future fusion devices. A possible pathway towards turbulence mitigation is opened by some plasma modes, such as Geodesic Acoustic Modes (GAMs) and Energetic Particle driven Geodesic Acoustic Modes (EGAMs).

GAMs

Geodesic Acoustic Modes are axisymmetric plasma modes characterized by a radial electric field and a simple poloidal structure that couples the $m = 0$ and the $m = \pm 1$ components.[2] They originate from the field curvature component which is tangential to flux surfaces, and that is know as the geodesic curvature. Research has indicated that GAMs can be non-linearly excited by turbulence, offering a potential saturation mechanism for turbulence itself. However, linear damping occurs in thermal plasma, with the roots of the dispersion relation residing in the lower half plane. Consequently, the non-linear excitation of GAMs is challenging to control for an operator, making them not so promising for turbulence control.

EGAMs

On the other hand, Energetic Particle driven Geodesic Acoustic Modes (EGAMs) look more promising [34]. If a population of fast particles, distributed according to some specific distribution functions (e.g., bump on tail), is injected into the plasma, the GAMs dispersion relation is perturbed and one of its stable roots can move into the upper half-plane. An unstable mode, known as EGAM, is thus created and it can potentially provide a stabilization mechanism for turbulence. Since fast ions can be manipulated to some extent through Neutral Beam Injection (NBI) and Ion Cyclotron Resonance Heating (ICRH), the control of EGAMs by an operator may be more feasible compared to the control of traditional GAMs.

[2] where m refers to the poloidal mode number in the oscillation ansatz eq.

In the context of our work GAMs and EGAMs will provide a simplified scenario for testing and exploiting the generalized dispersion relation. Moreover, the GAMs to EGAMs excitation mechanism corresponds to the pole extraction mechanism mentioned in conclusion of Sec. 4.2.

6.6 Part II Outline

By combining the linear gyrokinetic equations and by incorporating a few additional simplifying assumptions, a very general dispersion relation for shear Alfvén waves can be derived. Besides proving valuable as a mean to understand the physics of linear gyrokinetics, it also paves the way for a semi-analytical approach to solving the linear gyrokinetic system.

The dispersion relation requires the evaluation of integrals of the form

$$\int \frac{f(v)}{v-z} dv. \tag{1}$$

Since such an integral can be straightforwardly evaluated, by means of the Faddeeva function, only when f is a Maxwellian distribution, the dispersion relation is typically formulated in the literature exclusively for Maxwellian distributions. However, Xie's numerical scheme, presented in Chapter 5, provides an efficient and elegant way of computing the integral (1) and opens up generalization horizons for the dispersion relation and we venture toward them.

In Chapter 7, after retracing the main steps of the original derivation [4], we operate a few modifications that enable us to express the dispersion relation for arbitrary distribution functions. This reformulation allows the straightforward integration of Xie's numerical scheme.

Unfortunately, introducing non-Maxwellian distributions raises some mathematical issues, yet unresolved, that we will explore in Chapter 8.

Finally, in Chapter 9, we present some preliminary results within the context of GAMs and we take a peek at the potentialities of the small framework developed — consisting in the integration of the generalized dispersion relation and Xie's algorithm. The systematic usage of the framework is left for future work.

Chapter 7

Generalized Linear Gyrokinetic Dispersion Relation

In this chapter we present the generalized linear gyrokinetic dispersion relation for shear Alfvén waves. In Sec. 7.1 we sketch part of the derivation by highlighting in Subsection 7.1.2 the crucial steps — constituting the main difference with respect to the reference derivation [4] — required for the generalization to arbitrary distribution functions. In Sec. 7.2 we verify the correctness of our new formulas via a comparison with the original expressions for the Maxwellian case.

7.1 Derivation

The full derivation of the dispersion relation is based on three main steps: recasting the QN equation, recasting the GKM equation, and combining the new forms of QN and GKM into a single expression from which the dispersion relation is obtained. Given the self-similarity of some passages, and to avoid burdening the exposition with excessive mathematical details, we explain here only the steps needed to define the $\tilde{D}$ term appearing in the final results. The rest is given in Extra A at the end of the present chapter. We remark that while the passages of Subsection 7.1.1 follow closely Ref. [4][1], Subsection 7.1.2 contains the main new steps needed for the dispersion relation generalization.

7.1.1 From QN equation to the Symmetric Kinetic Integral $\mathbf{S}_{p,m}$

For an ion-electron plasma[2], the following steps are followed:

• **Splitting-Off the adiabatic response in the QN Equation:** First, the following substitution is introduced:

$$f = h + H_1 \frac{\partial F_0}{\partial E} - \left[e \frac{\partial F_0}{\partial E} - \frac{c \nabla F_0}{i\omega B} \cdot (\mathbf{b} \times \nabla) \right] \psi, \tag{7.1}$$

and the gyrokinetic equation Eq. (6.13) is transformed into

$$\frac{\partial h}{\partial t} + \left(\bar{U} \mathbf{b} + \mathbf{v}_d \right) \cdot \nabla h = \left[\frac{c \mathbf{b}}{eB} \times \nabla F_0 \cdot \nabla - \frac{\partial F_0}{\partial E} \frac{\partial}{\partial t} \right] \left[(\phi - \psi) + \frac{\hat{\omega}_d}{\omega} \psi \right], \tag{7.2}$$

[1] The only tiny difference is that in our case we totally neglect, from the very early steps, finite Larmor radius effects by setting $J_0 = 1$ for every particle species. Especially for α particles this might not be very accurate. Verifying the correctness of this assumption, or generalizing the required correction terms to non-Maxwellian distribution, is left as future work.

[2] The generalization to a three species plasma is straightforward and the final results for the three species case are provided in Extra B.

with $\hat{\omega}_d$ defined as

$$\hat{\omega}_d = \frac{\mathbf{v}_d}{i} \cdot \nabla. \tag{7.3}$$

With the same substitution, and by neglecting terms proportional to $\nabla\psi$, the perturbed density $n_{a,1} = \int \mathrm{d}^3 v f_a$ is rewritten as:

$$n_{a,1} = \int \mathrm{d}^3 \boldsymbol{v} h_a + e_a \int \mathrm{d}^3 \boldsymbol{v} \frac{\partial F_{0,a}}{\partial E}(\phi - \psi). \tag{7.4}$$

Summing over ions and electrons yields

$$\begin{aligned} 0 = \frac{\sum_a e_a n_{a1}}{\epsilon_0} &= \frac{|e|}{\epsilon_0}(n_{i,1} - n_{e,1}) \\ &= \frac{|e|}{\epsilon_0}\left[\int \mathrm{d}^3 \boldsymbol{v}(h_i - h_e) + |e|(\phi - \psi)\left(-\frac{n_{i0}}{T_i} + -\frac{n_{e0}}{T_e}\right)\right] \\ &= \frac{e^2 n_0}{\epsilon_0 T_e}\left[\frac{T_e}{|e|n_0}\int \mathrm{d}^3 \boldsymbol{v}(h_i - h_e) + (\phi - \psi)\left(-\frac{T_e}{T_i} - 1\right)\right]. \end{aligned} \tag{7.5}$$

Here, we defined the temperature T_a as

$$T_a = -\frac{n_{a0}}{\int \frac{\partial F_{0,a}}{\partial E}\mathrm{d}^3 \boldsymbol{v}}, \tag{7.6}$$

QN is hence split into an adiabatic component, proportional to $(\phi - \psi)$, and a non-adiabatic component, related to $(h_e - h_i)$:

$$0 = \frac{T_e}{|e|n_0}\int \mathrm{d}^3 \boldsymbol{v}(h_e - h_i) + (\phi - \psi)\,(1 + \tau)\,, \tag{7.7}$$

with $\tau = T_e/T_i$.

We remark the introduction of the 'generalized' temperature in Eq. (7.6). The definition aligns with the conventional one — as $T_a = \int \mathrm{d}^3 v F_{0,a}(v) v^2$ — when F_0 represents a Maxwellian, but for other distributions this correspondence does not generally hold. The introduction of this definition serves practical purposes, primarily establishing a reference quantity from which we can derive renormalizing quantities, such as the thermal velocity $v_{th,a} = \sqrt{2T_a/m_a}$.

• **Oscillatory Ansatz:** An eigenvalue problem approach is chosen by applying the following *Ansätze* for the non-adiabatic distribution function h, and for the electromagnetic potentials, ψ and ϕ:

$$h = \hat{h}(\theta) e^{in\varphi - i\omega t}, \tag{7.8}$$

$$(\phi, \psi) = \sum_m e^{in\varphi - im\theta - i\omega t}(\phi_m(r), \psi_m(r)). \tag{7.9}$$

With the ansatz on ψ and ϕ we make contact with the tokamak geometry. Toroidal modes are completely decoupled because of toroidal symmetry and coupling due to the poloidal inhomogeneities is taken into account by keeping the summation over the poloidal mode number m.

Eq. (7.2) is then integrated over time along particle trajectories:

$$\begin{aligned} \hat{h} =& ie \sum_m \int_{-\infty}^{t} \mathrm{d}t' e^{i[n(\varphi' - \varphi) - m(\theta' - \theta) - \omega(t' - t)]} e^{-im\theta} \\ & \frac{\partial F_0}{\partial E}\left[\omega - \hat{\omega}_*\right]\left[\phi_m\left(r'\right) - \left(1 - \frac{\omega_d\left(r', \theta'\right)}{\omega}\right)\psi_m\left(r'\right)\right], \end{aligned} \tag{7.10}$$

with

$$\hat{\omega}_* = -\frac{b \times \nabla F_0}{ieB\frac{\partial F_0}{\partial E}} \cdot \nabla. \tag{7.11}$$

• **Non-Adiabatic Density Response:** Since we are interested in resonant processes where the periodic particle motion matches the phase velocity of a wave, we expand the phase factor $\exp\left(i\left[n\left(\varphi' - \varphi\right) - m\left(\theta' - \theta\right) - \omega\left(t' - t\right)\right]\right)$ from Eq. (7.10) in bounce/transit harmonics counted by the index k. The coefficients for this expansion $a_{m,k,\sigma}$, $a^G_{m,k,\sigma}$, $K_{m,p,k,\sigma}$ and $K^G_{m,p,k,\sigma}$ are given in the appendix of Ref. [4]. For obtaining the dispersion relation and for constructing the weak form of the system, one has to integrate over the whole plasma volume. This operation requires a trivial toroidal integration, a radial integration (carried out numerically) and a poloidal angle integration (or projection, index p) that is carried out analytically, leading to the following expression for the non-adiabatic density response:

$$\begin{array}{c}\left(\int_{-\pi}^{\pi}\frac{\mathrm{d}\theta}{2\pi}\mathcal{J}_\theta e^{ip\theta}\int J_0 h_a \mathrm{d}^3\mathbf{v}\right)^{circ} = -2\pi e_a \sum_m \int_0^\infty \mathrm{d}v_\perp \int_0^\infty \mathrm{d}v_\parallel v_\parallel \cdot \sum_k \sum_\sigma \\ \frac{\partial F_0}{\partial E}\frac{(\omega-\hat{\omega}_*^m)}{\omega-(\sigma S_m^0+k)\omega_p}K_{m,p,k,\sigma}\cdot\left[a_{k,m,\sigma}\left(\phi_m\left(r^0\right)-\psi_m\left(r^0\right)\right)+a^G_{k,m,\sigma}\psi_m\left(r^0\right)\right],\end{array} \tag{7.12}$$

where

$$S_m\left(r^0\right) = nq\left(r^0\right) - m, \tag{7.13}$$

and r^0 stands for the orbit-averaged radial position of a particle. Furthermore,

$$\hat{\omega}_*^m = -\frac{b \times \nabla F_0}{eB\frac{\partial F_0}{\partial E}} \cdot k_m = -\frac{k_m \times b}{eB\frac{\partial F_0}{\partial E}} \cdot \nabla F_0 = -\frac{k_{m,\theta}}{eB\frac{\partial F_0}{\partial E}} \cdot \nabla F_0, \tag{7.14}$$

with $k_m \times b = k_{m,\theta}$. For simplicity, in contrast to Ref. [4], we neglect the precessional motion described by the frequency ω_{prec}.

Eq. (7.16) is given for passing particles: $\sigma = 1$ passing, $\sigma = -1$ counter passing. Similar expressions can be obtained for trapped particles.

• **Further Simplification: Strongly Passing Particles** For numerical computations, Eq. 7.16 is enough to solve the linear gyrokinetic system. However, it is useful to analytically simplify further and derive a general dispersion relation. The simplification is based on the expansion of the drift operator $\hat{\omega}_d$, that is only valid for passing particles with negligible perpendicular energy, i.e. $\omega_p t \approx \theta$, $\omega_p = v_\parallel / qR$. The expansions coefficients can be simplified as:

$$\begin{aligned} K_{m,p,k,\sigma=\pm1} &= \delta_{p,m\mp k} \\ a_{k,m,\sigma=+1} = \delta_k &= a_{-k,m,-1} \\ a^G_{k,m,\sigma=+1} &= \frac{\delta_{k,\pm1}}{2\omega}\hat{\omega}_d^\pm \\ a^G_{k,m,\sigma=-1} &= \frac{\delta_{k,\pm1}}{2\omega}\hat{\omega}_d^\pm \\ \hat{\omega}_{d,a}^\pm &= \frac{v_{th,a}^2}{\Omega_a R}\left(\frac{m}{r} \pm \frac{\partial}{\partial r}\right)\frac{v_\parallel^2 + v_\perp^2/2}{v_{th,a}^2} \end{aligned} \tag{7.15}$$

where the precession term from Ref. [4] is once again neglected. The passing particles approximation, consisting in summing exclusively over strongly passing particles trajectories, is hence adopted, as it has been shown to be sufficiently accurate approximation for many practical cases, e.g., EGAMs [40]

• **Split the Non-Adiabatic Density Response** The non-adiabatic density response from Eq. (7.16) is split into two terms by defining a symmetric term $\mathbf{S}_{p,m}$ multiplied by $(\phi_m - \psi_m)$, and another term $\mathbf{A}_{p,m}$ multiplied by ψ_m:

$$\left(\int_{-\pi}^{\pi}\frac{\mathrm{d}\theta}{2\pi}\mathcal{J}_\theta e^{ip\theta}\int J_0 h_a \mathrm{d}^3\mathbf{v}\right)^{circ} = -2\pi e_a \sum_m \left[\mathbf{S}_{p,m}(\phi_m - \psi_m) + \mathbf{A}_{p,m}\psi_m\right], \tag{7.16}$$

with

$$\mathbf{S}_{p,m} = \int_0^\infty \mathrm{d}v_\perp \int_0^\infty \mathrm{d}v_\parallel v_\parallel \cdot \sum_k \sum_\sigma \frac{\partial F_0}{\partial E}\frac{(\omega - \hat{\omega}_*^m)}{\omega - (\sigma S_m^0 + k)\,\omega_p} K_{m,p,k,\sigma}\cdot a_{k,m,\sigma}. \tag{7.17}$$

By using the approximated expressions (7.15) for the bounce harmonic coefficients, the sum over k and σ appearing in Eq. (7.17) is performed over passing and counter-passing particles. This results in

$$\sum_k \sum_\sigma \frac{(\omega - \hat{\omega}_*^m)}{\omega - (\sigma S_m^0 + k)\,\omega_t} K_{m,p,k,\sigma}\cdot a_{k,m,\sigma} = 2\omega \frac{(\omega - \hat{\omega}_*^m)}{\omega^2 - (S_m^0\omega_t)^2}\delta_{p,m}. \tag{7.18}$$

Similar expressions can be obtained for $A_{p,m}$ as well (see Extra at the end of the present chapter).

7.1.2 New Expression for the Symmetric Kinetic Integral $\mathbf{S}_{p,m}$

So far, we have essentially followed step by step the derivation in Ref [4]. Now, in contrast to the reference, we do not use the Maxwellian distribution and we express $\mathbf{S}_{p,m}$ in a more general way:

$$\begin{aligned}
\mathbf{S}_{p,m} &= \int_0^\infty \mathrm{d}v_\parallel \int_0^\infty \mathrm{d}v_\perp v_\perp \cdot \frac{\partial F_0}{\partial E}\sum_k\sum_\sigma \frac{(\omega - \hat{\omega}_*^m)}{\omega - (\sigma S_m^0 + k)\,\omega_t} K_{m,p,k,\sigma}\cdot a_{k,m,\sigma} \\
&= v_{th}^3 \int_0^\infty \mathrm{d}t \int_0^\infty \mathrm{d}s \cdot s \frac{\partial F_0}{\partial E}\frac{2\omega\,(\omega - \hat{\omega}_*^m)}{\omega^2 - \left(tk_{\parallel,m}v_{th}\right)^2}\delta_{p,m} \\
&= 2\omega v_{th}^3 \int_0^\infty \mathrm{d}t \frac{1}{\omega^2 - \left(tk_{\parallel,m}v_{th}\right)^2}\int_0^\infty \mathrm{d}s \cdot s \frac{\partial F_0}{\partial E}\,(\omega - \hat{\omega}_*^m)\,\delta_{p,m} \\
&= 2\frac{\omega}{(k_{\parallel,m}v_{th})^2} v_{th}^3 \int_0^\infty \mathrm{d}t \frac{1}{\left(\omega/(k_{\parallel,m}v_{th})\right)^2 - t^2}\int_0^\infty \mathrm{d}s \cdot s \frac{\partial F_0}{\partial E}\,(\omega - \hat{\omega}_*^m)\,\delta_{p,m} \\
&= \frac{x_m^2 v_{th}^3}{T}\int_0^\infty \mathrm{d}t \frac{1}{x_m^2 - t^2}\int_{Tt^2}^\infty \mathrm{d}E \cdot \frac{\partial F_0}{\partial E}\left(1 - \frac{\hat{\omega}_*^m}{\omega}\right)\delta_{p,m} \\
&= \frac{x_m^2 v_{th}^3}{T}\int_0^\infty \mathrm{d}t \frac{1}{x_m^2 - t^2}\left[-F_0(Tt^2) + \frac{k_{m,\theta}}{\omega e B}\int_{Tt^2}^\infty \mathrm{d}E \cdot \nabla F_0(E)\right]\delta_{p,m} \\
&= -\frac{x_m v_{th}^3}{2T}\left[-Z(x_m, F_0(Tt^2)) + \frac{k_{m,\theta}}{\omega e B} Z\left(x_m, \int_{Tt^2}^\infty \mathrm{d}E \cdot \nabla F_0(E)\right)\right]\delta_{p,m} = \mathbf{S}^m(x_m)\delta_{p,m},
\end{aligned} \tag{7.19}$$

where $x_m = \frac{\omega}{k_{\parallel,m} v_{th}}$, $E/T = t^2 + s^2$, $t = v_\parallel / v_{th}$, $s = v_\parallel / v_{th}$, $v_{th} = \sqrt{2T/m}$, and we make use of the identity

$$\begin{aligned}\int_0^\infty \mathrm{d}t \frac{f(t^2)}{x^2 - t^2} &= \frac{1}{2x}\left[\int_0^\infty \mathrm{d}t \frac{f(t^2)}{x - t} + \int_0^\infty \mathrm{d}t \frac{f(t^2)}{x + t}\right] \\ &= \frac{1}{2x}\left[\int_0^\infty \mathrm{d}t \frac{f(t^2)}{x - t} + \int_{-\infty}^0 \mathrm{d}t \frac{f(t^2)}{x - t}\right] \\ &= -\frac{1}{2x}\int_{-\infty}^\infty \mathrm{d}t \frac{f(t^2)}{t - x} = -\frac{Z(x, f(t^2))}{2x}\end{aligned} \tag{7.20}$$

$Z(z, f)$ is here defined as the well known integral

$$Z(x, f) = \int_{-\infty}^\infty \mathrm{d}t \frac{f(t^2)}{t - x}, \tag{7.21}$$

that diverges when x is real and that is discontinuous when moving from the UHP to the LHP:

$$\lim_{\Im(x)\to 0^+} Z(x, f) \neq \lim_{\Im(x)\to 0^-} Z(x, f) \tag{7.22}$$

To overcome this issue, we simply redefine $Z(x, f)$ by means of Landau contour,

$$Z(x, f) = \int_{-\infty}^\infty \mathrm{d}t \frac{f(t^2)}{t - x} \to Z(x, f) = \int_{LC} \mathrm{d}t \frac{f(t^2)}{t - x}, \tag{7.23}$$

and the new $Z(x, f)$ corresponds to the generalized plasma dispersion function from Eq. (2.22). In the next chapter we will argue that redefining $Z(x, f)$ via the Landau contour might not be fully justified. For the time being, we ignore possible complications.

Going back to the series of identities (7.19), we then define the function $\tilde{D}$ to uniform our notation with the reference literature:

$$\begin{aligned}\tilde{D}^m(x_m) &= \frac{2\pi T_a}{n_a}\mathbf{S}^m(x_m) \\ &= \frac{2\pi T_a}{n_a}\left\{-\frac{x_m v_{th,a}^3}{2T_a}\left[-Z(x_m, F_0(Tt^2)) + \frac{k_{m,\theta}}{\omega e B} Z\left(x_m, \int_{Tt^2}^\infty \mathrm{d}E \cdot \nabla F_0(E)\right)\right]\right\} \\ &= \left\{-\frac{\pi x_m v_{th,a}^3}{n_a}\left[-Z(x_m, F_0(Tt^2)) + \frac{k_{m,\theta}}{\omega e B} Z\left(x_m, \int_{Tt^2}^\infty \mathrm{d}E \cdot \nabla F_0(E)\right)\right]\right\}.\end{aligned} \tag{7.24}$$

7.1.3 Dispersion Relation with New D, N and H Terms

By repeating calculations very similar to the ones shown in Sections 7.1.1 and 7.1.2 for the 'non-symmetric' term $\mathbf{A}_{p,m}$ and for the GKM equation, we arrive at the dispersion relation

$$\begin{aligned}\omega^2\left(1 - \frac{\omega^*_{mi}}{\omega}\right) - \bar{k}_\parallel^2 \omega_A^2 R_0^2 =& \frac{2v_{th,i}^2}{R_0^2}\Bigg(-\left[H^p(x_{m-1}) + H^p(x_{m+1})\right] \\ &+\tau\left[\frac{N^{m-1}(x_{m-1})N^m(x_{m-1})}{D^{m-1}(x_{m-1})} + \frac{N^{m+1}(x_{m+1})N^m(x_{m+1})}{D^{m+1}(x_{m+1})}\right]\Bigg)\end{aligned} \tag{7.25}$$

with

$$D^p(x_p) = \left[1 + \tilde{D}^p(x_{p,e})\right] + \tau\left[1 + \tilde{D}^p(x_{p,i})\right], \tag{7.26}$$

$$N^m(x_p) = -\tilde{N}^m(x_{p,e}) + \tilde{N}^m(x_{p,i}), \tag{7.27}$$

$$H^m(x_p) = \tilde{H}^m(x_{p,i}) + \tau\tilde{H}^m(x_{p,e}). \tag{7.28}$$

and for the generic species s, $x_{p,s} = \omega/(|k_{\parallel,m}|v_{th,s})$, with $k_{\parallel,m} = (n - m/q)/R$. The expression for $\bar{k}_{\parallel,m}$ is provided in Extra A.

The form of the dispersion relation is identical to Ref. [4]. The only and substantial difference consists in the redefinition of the $\tilde{D}$, $\tilde{N}$ and $\tilde{H}$ terms, that are here summarized.

D term

$$\tilde{D}^m(x_p) = -\frac{\pi x_p v_{th}^3}{n}\left[-Z(x_m, F_0(Tt^2)) + \frac{k_{m,\theta}}{\omega eB} Z\left(x_p, \int_{Tt^2}^{\infty} \mathrm{d}E \cdot \nabla F_0(E)\right)\right]. \tag{7.29}$$

N term

$$\tilde{N}^m(x_p) = -\frac{\pi x_p v_{th}^3}{2n}\left[Z\left(x_p, \int_{Tt^2}^{\infty} \mathrm{d}E \frac{\partial F_0}{\partial E}\left(\frac{E}{2T} + \frac{t^2}{2}\right)\right) + \frac{k_{m,\theta}}{\omega eB} Z\left(x_p, \int_{Tt^2}^{\infty} \mathrm{d}E \nabla F_0\left(\frac{E}{2T} + \frac{t^2}{2}\right)\right)\right]. \tag{7.30}$$

H term

$$\tilde{H}^m(x_p) = -\frac{\pi x_p v_{th}^3}{4n}\left[Z\left(x_p, \int_{Tt^2}^{\infty} \mathrm{d}E \frac{\partial F_0}{\partial E}\left(\frac{E}{2T} + \frac{t^2}{2}\right)^2\right) + \frac{k_{m,\theta}}{\omega eB} Z\left(x_p, \int_{Tt^2}^{\infty} \mathrm{d}E \nabla F_0\left(\frac{E}{2T} + \frac{t^2}{2}\right)^2\right)\right]. \tag{7.31}$$

The utility of Eqs. (7.2), (7.2) and (7.2) is clear. They ideally allow to include non-Maxwellian distribution functions in the dispersion relation via the generalized plasma dispersion function $Z(x, f)$, that can be evaluated by means of Xie's numerical scheme. Unfortunately, as we will illustrate in the next chapter, including non-Maxwellian is in general not straightforward and raises some mathematical issues. Before diving into such issues, we first verify the correctness of our formulas for the Maxwellian case.

As side comments let us point out two further aspects. Firstly, for simplicity we assumed for the derivation above that the plasma under study entails only two species, electrons and ions. The generalization to three species is straightforward and it is carried out in Extra B. Secondly, we mention that the definitions of $\tilde{D}$, $\tilde{N}$ and $\tilde{H}$ will be used and implemented in a slightly different form, where $\partial F_0/\partial E$ is removed. The modified expressions, useful especially when F_0 is given as the product of two or more functions, are shown in Extra C.

7.2 Testing the New Formulas: Maxwellian Distribution

In Ref. [4], the expressions for $\tilde{D}$, $\tilde{N}$ and $\tilde{H}$ are given for the specific case of a Maxwellian distribution,

$$F_{0,M}(v(E), r) = \frac{n(r)}{\sqrt{2\pi T(r)}} e^{-\frac{E}{T(r)}}, \tag{7.32}$$

and they are expressed in terms of the Faddeeva function $Z_{Fad}(x)$:

$$\tilde{D}^m_{Fad}(x) = \left(1 - \frac{\omega^m_*}{\omega}\right) x Z_{Fad}(x) - \frac{\omega^m_*}{\omega}\eta\left(x^2 + x Z_{Fad}(x)(x^2 - \frac{1}{2})\right), \tag{7.33}$$

$$2\tilde{N}^m_{Fad}(x) = \left(1 - \frac{\omega^m_*}{\omega}\right)\left[x^2 + xZ_{Fad}(x)\left(x^2 + \frac{1}{2}\right)\right] - \frac{\omega^m_*}{\omega}\eta\left[x^2\left(x^2 + \frac{1}{2}\right) + xZ_{Fad}(x)\left(\frac{1}{4} + x^4\right)\right], \tag{7.34}$$

$$\begin{aligned}
\tilde{H}^m_{Fad}(x) &= \frac{1}{2}\left[\left(1 - \frac{\omega^m_*}{\omega}\right)\tilde{F}(x) - \eta\frac{\omega^m_*}{\omega}\tilde{G}(x)\right], \\
2\tilde{F}(x) &= xZ_{Fad}(x)\left(\frac{1}{2} + x^2 + x^4\right) + \frac{3x^2}{2} + x^4, \\
2\tilde{G}(x) &= xZ_{Fad}(x)\left(\frac{3}{4} + x^2 + \frac{x^4}{2} + x^6\right) + 2x^2 + x^4 + x^6,
\end{aligned} \tag{7.35}$$

where $\eta = \frac{\nabla n}{n}\frac{T}{\nabla T}$.

To test the correctness of the expressions introduced in the previous chapter, we than compare N, D and H from Eqs. , and , computed by means of Xie's numerical scheme, to $\tilde{D}_{Fad}$, $\tilde{N}_{Fad}$ and $\tilde{H}_{Fad}$.

The comparison is shown in Fig. 7.1 and proves the correctness of our formulas. Depending on the parameters used for the numerical scheme, accuracy up to 10^{-15} can be achieved.

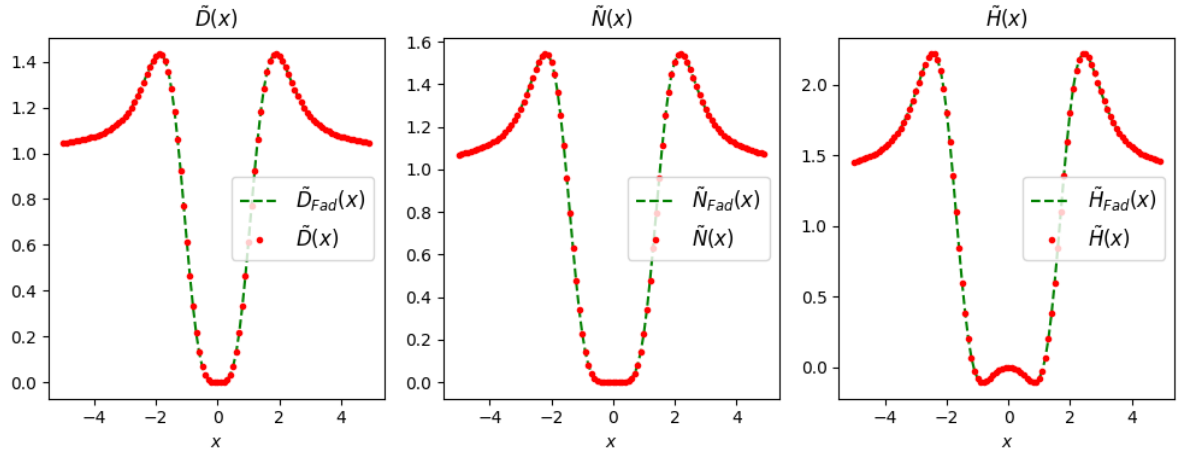

Figure 7.1: Real axis comparison of the terms N, D and H to the reference Maxwellian terms $\tilde{D}_{Fad}$, $\tilde{N}_{Fad}$ and $\tilde{H}_{Fad}$. Chosen parameters for the Maxwellian distribution $F_{0,M}(E, r_0)$: $T(r_0) = 2$, $m = e = 1$, $n(r_0) = 1$, $\nabla n(r_0) = \nabla T(r_0) = 1$.

Extra A: Derivation of the Shear Alfvén Dispersion Relation

We sketch the remaining part of the derivation for the shear Alfvén dispersion relation, including the explicit calculations for the generalized $\tilde{N}$ and $\tilde{H}$. As already mentioned, we closely follow Ref. [4] and the only substantial difference consists in how the kinetic integrals $\int \mathrm{d}v_\parallel \int \mathrm{d}v_\perp v_\perp$ are carried out.

Integrate $\mathbf{A_{p,m}}$ and Rewrite QN equation

• **Integrate $\mathbf{A_{p,m}}$ term:** We observe that $S_m^0 \pm 1 = nq - m \pm 1 = np - (m \mp 1) = S_{m\mp1}^0$ and proceed similarly to the previous point

$$\begin{aligned}
\sum_k \sum_\sigma \frac{\omega - \hat{\omega}_*^m}{\omega - (\sigma S_m^0 + k)\,\omega_t} K_{m,p,k,\sigma} \cdot a_{k,m,\sigma}^G &= \sum_k \Bigg[\frac{\omega - \hat{\omega}_*^m}{\omega - (S_m^0 + k)\,\omega_t} \delta_{p,m-k} \cdot \frac{\delta_{k,\pm1}}{2\omega} \hat{\omega}_d^\pm \\
&\quad + \frac{\omega - \hat{\omega}_*^m}{\omega - (-S_m^0 + k)\,\omega_t} \delta_{p,m+k} \cdot \frac{\delta_{k,\pm1}}{2\omega} \hat{\omega}_d^\mp \Bigg] \\
&= \sum_k \left[\frac{\omega - \hat{\omega}_*^m}{\omega^2 - (S_m^0 + k)^2\,\omega_t^2} \delta_{p,m-k} \cdot \delta_{k,\pm1} \hat{\omega}_d^\pm \right] \\
&= \frac{\omega - \hat{\omega}_*^m}{\omega^2 - (S_m^0 \pm 1)^2\,\omega_t^2} \delta_{p,m\mp1} \cdot \hat{\omega}_d^\pm \\
&= \frac{\omega - \hat{\omega}_*^m}{\omega^2 - (S_p^0 \omega_t)^2} \delta_{p,m\mp1} \cdot \hat{\omega}_d^\pm \\
&= \frac{\omega - \hat{\omega}_*^m}{\omega^2 - (v_\parallel k_{\parallel,p})^2} \delta_{p,m\mp1} \cdot \hat{\omega}_d^\pm = G_p^m \delta_{p,m\mp1} \hat{\omega}_d^\pm .
\end{aligned} \tag{7.36}$$

We then integrate

$$\begin{aligned}
\mathbf{A}_{p,m} &= \int_0^\infty \mathrm{d}v_\parallel \int_0^\infty \mathrm{d}v_\perp v_\perp \cdot \frac{\partial F_0}{\partial E} G_p^m \hat{\omega}_d^\pm \\
&= v_{th}^3 \int_0^\infty dt \frac{1}{\omega^2 - \left(t v_{th} k_{\parallel,p}\right)^2} \int_0^\infty \mathrm{d}t s \cdot \frac{\partial F_0}{\partial E} \left(\omega - \hat{\omega}_*^m\right) \hat{\omega}_d^\pm \\
&= v_{th}^3 \frac{\omega_d^\pm}{\omega} \frac{\omega^2}{v_{th}^2 k_\parallel^2} \int_0^\infty dt \frac{1}{x_p^2 - t^2} \int_{Tt^2}^\infty \frac{\mathrm{d}E}{2T} \cdot \frac{\partial F_0}{\partial E} \left(1 - \frac{\hat{\omega}_*^m}{\omega}\right) \left(\frac{E}{2T} + \frac{t^2}{2}\right) \\
&= v_{th}^3 \frac{\omega_d^\pm}{\omega} \frac{x_p^2}{2T} \int_0^\infty dt \frac{1}{x_p^2 - t^2} \int_{Tt^2}^\infty \mathrm{d}E \cdot \left[\frac{\partial F_0}{\partial E} \left(\frac{E}{2T} + \frac{t^2}{2}\right) + \frac{k_{m,\theta}}{\omega e B} \cdot \nabla F_0 \left(\frac{E}{2T} + \frac{t^2}{2}\right) \right] \\
&= -v_{th}^3 \frac{\omega_d^\pm}{\omega} \frac{x_p}{4T} \Bigg[Z\left(x_p, \int_{Tt^2}^\infty \mathrm{d}E \frac{\partial F_0}{\partial E} \left(\frac{E}{2T} + \frac{t^2}{2}\right)\right) + \\
&\qquad + \frac{k_{m,\theta}}{\omega e B} Z\left(x_p, \int_{Tt^2}^\infty \mathrm{d}E \nabla F_0 \left(\frac{E}{2T} + \frac{t^2}{2}\right)\right) \Bigg] = \frac{\omega_d^\pm}{\omega} A^m(x_p),
\end{aligned} \tag{7.37}$$

and to uniform the notation we define N:

$$\begin{aligned}\tilde{N}^m(x_p) &= \frac{2\pi T_a}{n_a} A^m(x_p) \\ &= \frac{2\pi T_a}{n_a}\left\{-\frac{x_p v_{th}^3}{4T_a}\left[Z\left(x_p, \int_{Tt^2}^{\infty} \mathrm{d}E \frac{\partial F_0}{\partial E}\left(\frac{E}{2T}+\frac{t^2}{2}\right)\right)+\frac{k_{m,\theta}}{\omega e B} Z\left(x_p, \int_{Tt^2}^{\infty} \mathrm{d}E \nabla F_0\left(\frac{E}{2T}+\frac{t^2}{2}\right)\right)\right]\right\} \\ &= \left\{-\frac{\pi x_p v_{th}^3}{2n_a}\left[Z\left(x_p, \int_{Tt^2}^{\infty} \mathrm{d}E \frac{\partial F_0}{\partial E}\left(\frac{E}{2T}+\frac{t^2}{2}\right)\right)+\frac{k_{m,\theta}}{\omega e B} Z\left(x_p, \int_{Tt^2}^{\infty} \mathrm{d}E \nabla F_0\left(\frac{E}{2T}+\frac{t^2}{2}\right)\right)\right]\right\}.\end{aligned} \tag{7.38}$$

• **Combine and Sum over Ions and Electrons:** By combining the integrations for $\mathbf{S_{p,m}}$ and $\mathbf{A_{p,m}}$, we obtain

$$\begin{aligned}\left(\int_{-\pi}^{\pi} \frac{d\theta}{2\pi} \mathcal{J}_\theta e^{ip\theta} \int J_0 h \mathrm{d}^3\mathbf{v}\right)^{circ} &= -2\pi \sum_m \left[\tilde{S}^m(x_m)\delta_{p,m}(\phi_m-\psi_m)+\frac{\omega_d^{\pm}}{\omega}\tilde{A}^m(x_p)\delta_{p,m\mp1}\psi_m\right] \\ &= \frac{-e_a n_a}{T_a}\sum_m \left[\tilde{D}^m(x_m)\delta_{p,m}(\phi_m-\psi_m)+\frac{\omega_d^{\pm}}{\omega}\tilde{N}^m(x_p)\delta_{p,m\mp1}\psi_m\right] \\ &= \frac{-e_a n_a}{T_a}\left[\tilde{D}^p(x_p)(\phi_p-\psi_p)+\sum_m \frac{\omega_d^{\pm}}{\omega}\tilde{N}^m(x_p)\delta_{p,m\mp1}\psi_m\right].\end{aligned} \tag{7.39}$$

We then sum up into Eq.(7.7). After defining D and N as

$$D^p(x_p) = \left[1+\tilde{D}^p(x_{p,e})\right]+\tau\left[1+\tilde{D}^p(x_{p,i})\right], \tag{7.40}$$

$$N^m(x_p) = -\tilde{N}^m(x_{p,e})+\tilde{N}^m(x_{p,i}). \tag{7.41}$$

QN equation hence assumes its final form:

$$0 = D^p(x_p)(\phi_p-\psi_p)+\tau\sum_m \frac{\omega_{di}^{\pm}}{\omega} N^m(x_p)\delta_{p,m\mp1}\psi_m. \tag{7.42}$$

GKM equation

We now take into account the GKM equation. After similar steps to those of the previous sections, we plug QN into GKM and obtain the dispersion relation.

• **Integral Term in GKM:** We consider the integral term in Eq. (6.17) and simplify it by leaving only the non-adiabatic component with h,

$$\int e_a \frac{v_d}{i\omega}\cdot\nabla f_a \mathrm{d}^3 v = \int e\frac{v_d}{i\omega}\cdot\nabla h_a \mathrm{d}^3 v + \text{O.T.}. \tag{7.43}$$

• **Integration over Plasma Volume:** As before, we use Eq. (7.2) and the bounce harmonic expansions, and we arrive at the following expression for the volume integrated GKM integral

$$\begin{aligned}&\left(\int_{-\pi}^{\pi}\frac{\mathrm{d}\theta}{2\pi}\mathcal{J}_\theta e^{ip\theta}\int e_a\frac{v_d}{i\omega}\cdot\nabla f \mathrm{d}^3 v\right)^{circ} = -2\pi e_a^2 \textstyle\sum_m \int_0^\infty \mathrm{d}v_\perp \int_0^\infty \mathrm{d}v_\parallel v_\parallel \cdot \sum_k \sum_\sigma \\ &\frac{\partial F_0}{\partial E}\frac{(\omega-\hat{\omega}_*^m)}{\omega-(\sigma S_m^0+k)\omega_t} K^G_{m,p,k,\sigma}\cdot\left[a_{k,m,\sigma}\phi_m\left(r^0\right)-\left(a_{k,m,\sigma}-a^G_{k,m,\sigma}\right)\psi_m\left(r^0\right)\right].\end{aligned} \tag{7.44}$$

• **New 'Bounce' Coefficients:** Under the same assumptions used for the other bounce harmonics coefficients, and by neglecting the precession term, we have

$$\begin{aligned} K^G_{m,p,k,1} &\approx \delta_{p,m-k\pm1}\frac{\omega_d^{\mp}}{2\omega}, \\ K^G_{m,p,k,-1} &\approx \delta_{p,m+k\pm1}\frac{\omega_d^{\pm}}{2\omega}, \end{aligned} \tag{7.45}$$

with the following symmetry relation

$$K^G_{m,p,k,+1} = K^G_{m,p,-k,+1}. \tag{7.46}$$

• **Integrate $K^G_{m,p,k,\sigma}a_{k,m,\sigma}$ Term:** The integral of Eq. (7.44) is split into two components. The first one, containing the $K^G_{m,p,k,\sigma}a_{k,m,\sigma}$ term, leads to the same A function previously introduced. Summing over passing and counter-passing particles:

$$\begin{aligned} \sum_k\sum_\sigma \frac{(\omega-\hat{\omega}_*^m)}{\omega-(\sigma S_m^0+k)\,\omega_t}K^G_{m,p,k,\sigma}\cdot a_{k,m,\sigma} &= \sum_k \frac{(\omega-\hat{\omega}_*^m)\,\hat{\omega}_d^{\mp}}{\omega^2-(S_m^0+k)^2\,\omega_t^2}\delta_{p,m-k\pm1}\cdot\delta_k \\ &= \frac{(\omega-\hat{\omega}_*^m)\,\hat{\omega}_d^{\mp}}{\omega^2-(S_m^0\omega_t)^2}\delta_{p,m\pm1} \\ &= G_m^m\delta_{p,m\pm1}\hat{\omega}_d^{\mp} \end{aligned} \tag{7.47}$$

integrating leads then to:

$$\int_0^\infty \mathrm{d}v_\parallel \int_0^\infty \mathrm{d}v_\perp v_\perp\cdot\frac{\partial F_0}{\partial E}G_m^m\hat{\omega}_d^{\mp} = \frac{\omega_d^{\mp}}{\omega}A^m(x_m) \tag{7.48}$$

• **Integrate $K^G_{m,p,k,\sigma}a^G_{k,m,\sigma}$ Term:** For the $K^G_{m,p,k,\sigma}a^G_{k,m,\sigma}$ term, we have

$$\begin{aligned} \sum_k\sum_\sigma \frac{(\omega-\hat{\omega}_*^m)}{\omega-(\sigma S_m^0+k)\,\omega_t}K^G_{m,p,k,\sigma}\cdot a^G_{k,m,\sigma} &= \sum_k \frac{(\omega-\hat{\omega}_*^m)\,\frac{\omega_d^{\mp}}{2\omega}}{\omega^2-(S_m^0+k)^2\,\omega_t^2}\delta_{p,m-k\pm1}\cdot\delta_{k,\pm1}\hat{\omega}_d^{\pm} \\ &= \frac{(\omega-\hat{\omega}_*^m)\,\omega_d^{\mp}}{\omega^2-(S_m^0+1)^2\,\omega_t^2}\delta_{p,m-1\pm1}\cdot\frac{\hat{\omega}_d^{+}}{2\omega} + \frac{(\omega-\hat{\omega}_*^m)\,\omega_d^{\mp}}{\omega^2-(S_m^0-1)^2\,\omega_t^2}\delta_{p,m+1\pm1}\cdot\frac{\hat{\omega}_d^{-}}{2\omega} \\ &= \frac{(\omega-\hat{\omega}_*^m)}{\omega^2-(S_m^0+1)^2\,\omega_t^2}\delta_{p,m}\frac{\hat{\omega}_d^{-}\hat{\omega}_d^{+}}{2\omega} + \frac{(\omega-\hat{\omega}_*^m)}{\omega^2-(S_m^0-1)^2\,\omega_t^2}\delta_{p,m}\frac{\hat{\omega}_d^{+}\hat{\omega}_d^{-}}{2\omega} \\ &= \frac{(\omega-\hat{\omega}_*^m)}{\omega^2-\left(S_{m-1}^0\omega_t\right)^2}\delta_{p,m}\frac{\hat{\omega}_d^{-}\hat{\omega}_d^{+}}{2\omega} + \frac{(\omega-\hat{\omega}_*^m)}{\omega^2-\left(S_{m+1}^0\omega_t\right)^2}\delta_{p,m}\frac{\hat{\omega}_d^{+}\hat{\omega}_d^{-}}{2\omega} \\ &= G_{m-1}^m\delta_{p,m}\frac{\hat{\omega}_d^{-}\hat{\omega}_d^{+}}{2\omega} + G_{m+1}^m\delta_{p,m}\frac{\hat{\omega}_d^{+}\hat{\omega}_d^{-}}{2\omega}, \end{aligned} \tag{7.49}$$

(neglecting terms proportional to ω_{prec} and to $\delta_{p,m\pm2}$) where $p = m \pm 1$. The corresponding integral becomes

$$\begin{aligned}
&\int_0^\infty \mathrm{d}v_\parallel \int_0^\infty \mathrm{d}v_\perp v_\perp \cdot \frac{\partial F_0}{\partial E} G_p^m \frac{\hat{\omega}_d^- \hat{\omega}_d^+}{2\omega} \\
&\quad = \int_0^\infty \mathrm{d}v_\parallel \int_0^\infty \mathrm{d}v_\perp v_\perp \cdot \frac{\partial F_0}{\partial E} \frac{(\omega - \hat{\omega}_*^m)}{\omega^2 - \left(S_p^0 \omega_t\right)^2} \frac{\hat{\omega}_d^- \hat{\omega}_d^+}{2\omega} \\
&\quad = v_{th}^3 \int_0^\infty \mathrm{d}t \frac{1}{\omega^2 - \left(t v_{th} k_{\parallel,p}\right)^2} \int_0^\infty \mathrm{d}t s \cdot \frac{\partial F_0}{\partial E} \left(\omega - \hat{\omega}_*^m\right) \cdot \frac{\hat{\omega}_d^- \hat{\omega}_d^+}{2\omega} \\
&\quad = v_{th}^3 \frac{x_p^2 \omega_d^- \omega_d^+}{2\omega^2} \int_0^\infty \mathrm{d}t \frac{1}{x_p^2 - t^2} \int_{Tt^2}^\infty \frac{\mathrm{d}E}{2T} \cdot \frac{\partial F_0}{\partial E} \left(1 - \frac{\hat{\omega}_*^m}{\omega}\right) \left(\frac{E}{2T} + \frac{t^2}{2}\right)^2 \\
&\quad = v_{th}^3 \frac{\omega_d^- \omega_d^+}{2\omega^2} \frac{x_p^2}{2T} \int_0^\infty \mathrm{d}t \frac{1}{x_p^2 - t^2} \int_{Tt^2}^\infty \mathrm{d}E \cdot \left[\frac{\partial F_0}{\partial E} \left(\frac{E}{2T} + \frac{t^2}{2}\right)^2 + \frac{k_{m,\theta}}{\omega e B} \cdot \nabla F_0 \left(\frac{E}{2T} + \frac{t^2}{2}\right)^2 \right] \\
&\quad = -v_{th}^3 \frac{\omega_d^- \omega_d^+}{2\omega^2} \frac{x_p}{4T} \left[Z\left(x_p, \int_{Tt^2}^\infty \mathrm{d}E \frac{\partial F_0}{\partial E} \left(\frac{E}{2T} + \frac{t^2}{2}\right)^2\right) + \right. \\
&\qquad \left. + \frac{k_{m,\theta}}{\omega e B} Z\left(x_p, \int_{Tt^2}^\infty \mathrm{d}E \nabla F_0 \left(\frac{E}{2T} + \frac{t^2}{2}\right)\right)^2 \right] = \frac{\omega_d^- \omega_d^+}{\omega^2} B^m(x_p).
\end{aligned} \tag{7.50}$$

Next, we define the $\tilde{H}$ function:

$$\begin{aligned}
\tilde{H}^m(x_p) &= \frac{2\pi T_a}{n_a} B^m(x_p) \\
&= \frac{2\pi T_a}{n_a} \left\{ -\frac{x_p v_{th}^3}{8T_a} \left[Z\left(x_p, \int_{Tt^2}^\infty \mathrm{d}E \frac{\partial F_0}{\partial E} \left(\frac{E}{2T} + \frac{t^2}{2}\right)^2\right) + \frac{k_{m,\theta}}{\omega e B} Z\left(x_p, \int_{Tt^2}^\infty \mathrm{d}E \nabla F_0 \left(\frac{E}{2T} + \frac{t^2}{2}\right)^2\right)\right]\right\} \\
&= \left\{ -\frac{\pi x_p v_{th}^3}{4n_a} \left[Z\left(x_p, \int_{Tt^2}^\infty \mathrm{d}E \frac{\partial F_0}{\partial E} \left(\frac{E}{2T} + \frac{t^2}{2}\right)^2\right) + \frac{k_{m,\theta}}{\omega e B} Z\left(x_p, \int_{Tt^2}^\infty \mathrm{d}E \nabla F_0 \left(\frac{E}{2T} + \frac{t^2}{2}\right)^2\right)\right]\right\}.
\end{aligned} \tag{7.51}$$

• **Sum Up over Electrons and Ions:**

$$\begin{aligned}
&\frac{e_i^2 n_i}{\omega^2 T_i} \omega_{di}^- \omega_{di}^+ \tilde{H}^m(x_{pi}) + \frac{e_e^2 n_e}{\omega^2 T_e} \omega_{de}^- \omega_{de}^+ \tilde{H}^m(x_{pe}) = \frac{e^2 n_e \tau}{\omega^2 T_e} \omega_{di}^- \omega_{di}^+ \tilde{H}^m(x_{pi}) + \frac{e^2 n_e}{\omega^2 T_e} \tau^2 \omega_{di}^- \omega_{di}^+ \tilde{H}^m(x_{pe}) \\
&\quad \frac{e^2 n_e \tau}{\omega^2 T_e} \omega_{di}^- \omega_{di}^+ \left[\tilde{H}^m(x_{pi}) + \tau \tilde{H}^m(x_{pi})\right] = \omega_{di}^- \omega_{di}^+ \frac{e^2 n_e \tau}{\omega^2 T_e} H^m(x_p).
\end{aligned} \tag{7.52}$$

• **Plug QN into GKM:** With $\tilde{N}$ and $\tilde{H}$ the kinetic integral for GKM becomes

$$\begin{aligned}
\left(\int_{-\pi}^{\pi} \frac{\mathrm{d}\theta}{2\pi} \mathcal{J}_\theta e^{ip\theta} \int e_a \frac{v_d}{i\omega} \cdot \nabla J_0 f \mathrm{d}^3 v\right)^{circ} &= -\frac{e^2 n_e \tau}{\omega^2 T_e} \left[\omega_{di}^- \omega_{di}^+ H^p(x_{p-1}) + \omega_{di}^- \omega_{di}^+ H^p(x_{p+1})\right] \psi_p \\
&\quad + \frac{e^2 n_e \tau^2}{\omega T_e} \sum_m \omega_d^\mp \delta_{p,m\pm1} N^m(x_m)(\phi_m - \psi_m).
\end{aligned} \tag{7.53}$$

We now plug the in QN equation by replacing $(\phi - \psi)$ through Eq. (7.42). Taking only $l = p$ terms proportional to ψ_p:

$$\begin{aligned}
&\sum_m \omega_{di}^{\mp}\delta_{p,m\pm1}N^m(x_m)\left(\sum_l \frac{\omega_{di}^{\pm}}{\omega}\delta_{l,m\mp1}\frac{N^l(x_m)}{D^m(x_m)}\psi_l\right)\Bigg|_{\psi_p} \\
&= \sum_m \omega_{di}^{\mp}\delta_{p,m\pm1}N^m(x_m)\left(\frac{\omega_{di}^{\pm}}{\omega}\delta_{p,m\mp1}\frac{N^p(x_m)}{D^m(x_m)}\psi_p\right) \\
&= \frac{\omega_{di}^{-}\omega_{di}^{+}}{\omega}\left[\frac{N^{p-1}(x_{p-1})N^p(x_{p-1})}{D^{m-1}(x_{m-1})} + \frac{N^{p+1}(x_{p+1})N^p(x_{p+1})}{D^{p+1}(x_{p+1})}\right]\psi_p,
\end{aligned} \tag{7.54}$$

and we get

$$\begin{aligned}
\left(\int_{-\pi}^{\pi}\frac{\mathrm{d}\theta}{2\pi}\mathcal{J}_\theta e^{ip\theta}\int e_a\frac{v_d}{i\omega}\cdot\nabla J_0 f\mathrm{d}^3v\right)^{circ} =& -\frac{e^2n_e\tau}{\omega^2T_e}\left[\omega_{di}^{-}\omega_{di}^{+}H^p(x_{p-1}) + \omega_{di}^{-}\omega_{di}^{+}H^p(x_{p+1})\right]\psi_p \\
&+ \frac{e^2n_e\tau^2}{\omega^2T_e}\omega_{di}^{-}\omega_{di}^{+}\left[\frac{N^{p-1}(x_{p-1})N^p(x_{p-1})}{D^{m-1}(x_{m-1})} + \frac{N^{p+1}(x_{p+1})N^p(x_{p+1})}{D^{p+1}(x_{p+1})}\right]\psi_p.
\end{aligned} \tag{7.55}$$

Dispersion Relation

We recall the GKM equation, where only non-adiabatic term is kept inside the integral:

$$\begin{aligned}
&-\omega^2\nabla_\perp\frac{1}{v_A^2}\nabla_\perp\phi + \left[\nabla(\nabla\psi)_\parallel\times\mathbf{b}\right]\cdot\nabla\left(\frac{\mu_0 j_{0\parallel}}{B}\right) + (\mathbf{B}\cdot\nabla)\frac{\left(\nabla\times\nabla\times(\nabla\psi)_\parallel\right)\cdot\mathbf{B}}{B^2} \\
&= \omega^2\mu_0\sum_a e_a\int\frac{\mathbf{v}_{d,a}\cdot\nabla}{i\omega}J_0h_a\mathrm{d}^3\mathbf{v} + \sum_a b\times\nabla\left(\frac{\beta_{a\perp}}{2\Omega_a}\right)\cdot\nabla\nabla_\perp^2\phi.
\end{aligned} \tag{6.17}$$

We rewrite the second term on the rhs, after defining $p_\perp = \int \mathrm{d}^3vB\mu F_0 = m_a\int\mathrm{d}^3vv_\perp^2F_0$:

$$\begin{aligned}
\sum_a b\times\nabla\left(\frac{\beta_{a\perp}}{2\Omega_a}\right)\cdot\nabla &\approx b\times\nabla\left(\frac{\beta_{i\perp}}{2\Omega_i}\right)\cdot\nabla \\
&= b\times\nabla\left(\frac{m_i\mu_0p_\perp}{e_iB^3}\right)\cdot\nabla \\
&\approx i\frac{\mu_0m_in_i}{B^2}\frac{b\times\nabla p_\perp}{ie_iBn_i}\cdot\nabla \\
&= i\frac{\omega_{pi}^*}{v_A^2},
\end{aligned} \tag{7.56}$$

with

$$\omega_{pi} = \frac{b\times\nabla p_\perp}{ie_iBn_i}\cdot\nabla = \frac{k_{m,\theta}}{e_iBn_i}\nabla p_\perp \approx \frac{k_{m,\theta}}{e_iBn_i}\frac{\partial p_\perp}{\partial r}, \tag{7.57}$$

and we notice

$$\begin{aligned}
\mu_0\frac{e^2n_e}{\omega^2T_e}\omega_{di}^{-}\omega_{di}^{+} &\approx -\mu_0\frac{e^2n_e}{\omega^2T_e}\left(\frac{1}{\Omega_iR_0}\frac{\partial}{\partial r}\right)^2 \\
&= \mu_0\frac{e^2n_e}{\omega^2T_e}\frac{m_i^2}{e^2B^2}\frac{1}{R_0^2}k_\perp^2 \\
&= 2\frac{1}{v_A^2v_{thi}^2}\frac{1}{\tau}\frac{k_\perp^2}{R_0^2}.
\end{aligned} \tag{7.58}$$

Now, by applying the ansatz for the EM potentials, by integrating over the plasma volume, by keeping only the radial derivatives and by expanding up to second order in ω_d^r, we obtain:

$$\begin{aligned}\omega^2\left(1-\frac{\omega_{pi}^*}{\omega}\right)-\hat{k}_{\|p}^2\omega_A^2R_0^2=&\frac{2v_{thi}^2}{R_0^2}\Bigg(-\left[H^p(x_{p-1})+H^p(x_{p+1})\right]\\&+\tau\left[\frac{N^{p-1}(x_{p-1})N^p(x_{p-1})}{D^{p-1}(x_{p-1})}+\frac{N^{p+1}(x_{p+1})N^p(x_{p+1})}{D^{p+1}(x_{p+1})}\right]\Bigg),\end{aligned}\tag{7.59}$$

where $\bar{k}_{\|p}^2$ stands for the parallel wave vector including the toroidal coupling up to first order in ϵ, e.g. $\bar{k}_{\|p}^2=\left(k_{\|p}^2+k_{\|p+1}^2\pm\sqrt{\left(k_{\|p}^2-k_{\|p+1}^2\right)^2+4\hat{\epsilon}^2r^2k_{\|p}^2k_{\|p+1}^2}\right)/\left(2\left(1-\hat{\epsilon}^2r^2\right)\right)$ where $\hat{\epsilon}$ is $\hat{\epsilon}=5r/2R$.

Extra B: D, N and H for the Three-Species Case

We consider a plasma consisting of three species: electrons, ions and a third ion species a with charge $e_a = Ze$. We denote the equilibrium densities as

$$n_{e0}, \quad n_{i0} = \beta n_{e0}, \quad n_{i0} = \alpha n_{e0}. \tag{7.60}$$

From the neutrality condition at equilibrium, $\sum e_s n_{s,0}$, we have $\beta = 1 - Z\alpha$.

If we now add the third species into the series of identities (7.5), we obtain

$$\begin{aligned} 0 &\approx \frac{|e|}{\epsilon_0}\left[\int d^3\boldsymbol{v}(h_i + Zh_a - h_e) + |e|(\phi-\psi)\left(-\frac{n_{i0}}{T_i} + -\frac{n_{e0}}{T_e} + -\frac{Z^2 n_{a0}}{T_a}\right)\right] \\ &\approx \frac{e^2 n_0}{\epsilon_0 T_e}\left[\frac{T_e}{|e|n_0}\int d^3\boldsymbol{v}(h_i + Zh_a - h_e) + (\phi-\psi)\left(-\beta\frac{T_e}{T_i} - 1 - \frac{Z^2\alpha T_e}{T_a}\right)\right] \\ &\approx \frac{e^2 n_0}{\epsilon_0 T_e}\left[\frac{T_e}{|e|n_0}\int d^3\boldsymbol{v}(h_e - h_i - Zh_a) + (\phi-\psi)\left(1 + \beta\tau_i + Z^2\alpha\tau_a\right)\right]. \end{aligned} \tag{7.61}$$

Here, we define $\tau_i = T_e/T_i$ and $\tau_a = T_e/T_a$. Next, inserting the symmetric part of the kinetic integral $\int d^3\boldsymbol{v} h_s$, expressed in terms of $\tilde{D^p}(x_{ps})$, yields

$$\begin{aligned} &\frac{T_e}{|e|n_0}\left[\frac{-e_e n_e}{T_e}\tilde{D}^p(x_{pe}) - \frac{-e_i n_i}{T_i}\tilde{D}^p(x_{pi}) - Z\frac{-e_a n_a}{T_a}\tilde{D}^p(x_{pa})\right] + \left(1 + \beta\tau_i + Z^2\alpha\tau_a\right) = \\ &= \left[\tilde{D}^p(x_{pe}) + \beta\tau_i\tilde{D}^p(x_{pi}) + Z^2\alpha\tau_a\tilde{D}^p(x_{pa})\right] + \left(1 + \beta\tau_i + Z^2\alpha\tau_a\right) = \\ &= \left[1 + \tilde{D}^p(x_{pe})\right] + \beta\tau_i\left[1 + \tilde{D}^p(x_{pi})\right] + Z^2\alpha\tau_a\left[1 + \tilde{D}^p(x_{pi})\right] \\ &= D^p(x_p) \end{aligned} \tag{7.62}$$

For N and H, we can proceed similarly and by retracing the derivation in Extra A we are led to the following re-definitions:

$$\tilde{N}^m(x_p) = -\tilde{N}^m(x_{pe}) + \beta\tilde{N}^m(x_{pi}) + Z^2\alpha\tilde{N}^m(x_{pa}), \tag{7.63}$$

and

$$H^m(x_p) = \beta\tilde{H}^m(x_{pi}) + \tau_i\tilde{H}^m(x_{pe}) + Z^2\alpha\frac{\tau_i}{\tau_a}\tilde{H}^m(x_{pa}). \tag{7.64}$$

By setting $\alpha = 0$, it is immediate to check that the definitions just introduced match definitions (7.2), (7.2) and (7.2) for the electron-ion plasma case.

Extra C: Useful Expressions

The integrals containing $\partial F_0/\partial E$ in the definitions of $\tilde{N}$ and $\tilde{H}$ — as per Eqs. (7.2) and (7.2) — are conveniently rewritten as

$$\begin{aligned}\int_{Tt^2}^{\infty} \mathrm{d}E \frac{\partial F_0}{\partial E}\left(\frac{E}{2T}+\frac{t^2}{2}\right) &= \left[\frac{E}{2T}F_0(Tt^2)\right]_{Tt^2}^{\infty} - \int_{Tt^2}^{\infty}\mathrm{d}E\frac{F_0(E)}{2T} - \frac{t^2}{2}F_0(Tt^2) \\ &= -t^2F_0(Tt^2) - \frac{1}{2T}\int_{Tt^2}^{\infty}\mathrm{d}EF_0(E),\end{aligned} \tag{7.65}$$

and

$$\int_{Tt^2}^{\infty} \mathrm{d}E \frac{\partial F_0}{\partial E}\left(\frac{E}{2T}+\frac{t^2}{2}\right)^2 = -t^4F_0(Tt^2) - \frac{t^2}{2T}\int_{Tt^2}^{\infty}\mathrm{d}EF_0(E) - \frac{1}{2T^2}\int_{Tt^2}^{\infty}\mathrm{d}EEF_0(E). \tag{7.66}$$

These expressions are useful when distribution functions such as $F_0 = f_0(E)H(E_c - E)$ are taken into account[3], since they avoid the introduction of a correction term due to the derivative singularity. Similarly, when H is replaced by a sigmoid, the expressions avoid using the product rule and the associated term $F_0\partial\sigma/\partial E$; where $F_0\partial\sigma/\partial E$ diverges in the limit $\sigma \to H$ and it is likely to determine computational overflow.

[3]In case $F_0 = f_0(E)H(E_c - E)$ the equalities (7.65) have to be modified by taking into account a $\delta(E_c)$ term. Nevertheless, the final expression remains the same.

Chapter 8

Extending the Dispersion Relation into the Lower Half-Plane

In the previous section, we briefly mentioned how the $\tilde{D}$, $\tilde{N}$ and $\tilde{H}$ terms are extended into the complex plane by employing Landau's contour. Similarly to the Vlasov-Poisson problem, this means that integrals such as

$$\int_{-\infty}^{\infty} \frac{G(t)}{t-x} \mathrm{d}t, \tag{8.1}$$

are redefined by means of the Landau analytical continuation:

$$\int_{LC} \frac{G(t)}{t-x} \mathrm{d}t. \tag{8.2}$$

In this chapter, illustrating the discontinuities of $\tilde{D}$, $\tilde{N}$ and $\tilde{H}$ (Sec. 8.1) leads us to argue that this operation might not be fully legitimate when distributions function $F_0(v)$ that are neither Maxwellian nor κ are considered, and that the overall eigenvalue problem might require a reformulation as initial value problem (Sec. 8.2).

8.1 Analysing the Integral Function $\int_{Tx^2}^{\infty} g(E)\mathrm{d}E$: a Collection of Vexing Discontinuities

In Chapter 7, we did not mention an important feature of the $Z = Z(x, G(x))$ functions appearing in the definition of $\tilde{D}$, $\tilde{N}$ and $\tilde{H}$. Specifically, the argument $G(x)$ of $Z(x, G(x))$ is an integral function, that we generically indicate as

$$G(x) = \int_{Tx^2}^{\infty} g(E)\mathrm{d}E = \int_{Tx^2}^{\infty} E^n F_0(E)\mathrm{d}E = -\int_0^{Tx^2} E^n F_0(E)\mathrm{d}E + G(0) = -\bar{G}(x) + G(0). \tag{8.3}$$

Here, the x variable appears in the lower bound Tx^2 and the integrand function $g(E)$ can be expressed as $E^n F_0(E)$ — with F_0 the equilibrium distribution function and $n = 0, 1, 2$ — because of the expressions given in Extra C of Chapter 7. Moreover, to slightly simplify the following discussion, in the last equality $G(x)$ is rewritten as the sum of $\bar{G}(x)$ and a real constant $G(0)$, so to replace the $[Tx^2, \infty]$ integration interval with a more convenient $[0, Tx^2]$.

If $x \in \mathbb{R}$, $G(x)$ is clearly well defined as a real-variable integral function with a real function as integrand. However, when evaluating the $2i\pi G(x)$ term for the analytical continuation of $Z(x, G(x))$, as per Eq. (2.22), x takes complex values and the integral $\bar{G} = \int_0^{Tx^2} g(E)\mathrm{d}E$ is no longer confined on the real axis. Two 'complex' definitions are then required:

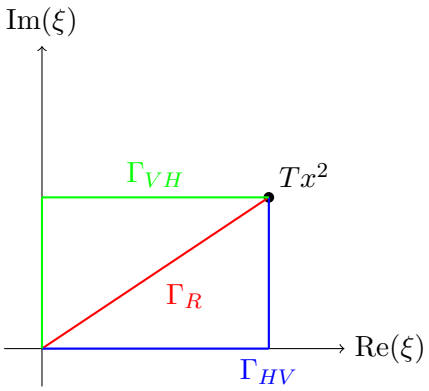

Figure 8.1: Different complex contour adopted for $\int_0^{Tx^2}$

- The real variable integrand function $g(E)$ needs to be redefined as a complex variable function $g(\xi)$. As we have already discussed for the Vlasov-Poisson system, such a redefinition cannot be always performed in a unique way.
- The complex integration contour, connecting the origin and Tx^2, has to be specified. Again, a multiplicity of choices is available.

For the Maxwellian case, the complex definition of $g(E) = E^n F_{0,M}(E)$ can be easily and uniquely performed by replacing E with a complex variable ξ. As regards the contour, we opt for the choice expressed by the following identity:

$$\begin{aligned} G(x) &= G(0) - \int_0^{Tx^2} g(\xi)\mathrm{d}\xi \\ &= G(0) - \int_0^{\Re[Tx^2]} g(\xi)\mathrm{d}\xi - \int_{\Re[Tx^2]}^{Tx^2} g(\xi)\mathrm{d}\xi. \end{aligned} \tag{8.4}$$

Hence, we decompose $\int_0^{Tx^2}$ as a sum of a real line 'horizontal' segment, $[0, \Re[Tx^2]]$, and a vertical segment $[\Re[Tx^2], Tx^2]$; we denote such contour as Γ_{HV} (see Fig. 8.1). As $g(\xi) = \xi^n F_{0,M}(\xi)$ does not have singularity points in the complex plane, it is easy to show via the residue theorem[1] that $G(x)$ does not depend on the chosen contour. This is why we overlooked this detail in Sec. 7.2.

However, as different distribution functions $F_0(x)$ are introduced, such an argument does no longer hold true, and fearsome discontinuities in the LHP definition of $G(x)$ arise. In the present section we examine such discontinuities.

8.1.1 Discontinuities due to $F_0(E)$ singularities

The first kind of discontinuity we analyse is generated by the singularity points of the function $g(\xi) = \xi^n F_0(\xi)$. To illustrate practically how this discontinuity emerges, let us consider the example of $g(E) = 1/(1+E)^\kappa$, corresponding to the case of κ distributions. $g(\xi)$ has a singularity of order κ at $\xi_s = -1$. If we adopt the same Γ_{HV} contour to compute $G(x)$, it is clear that whenever $\Re(Tx^2) < -1$, ξ_s belongs to the real axis interval $[\Re(Tx^2), \infty]$ and $G(x)$ diverges (see left sub-figure of Fig. 8.4). To properly define $G(x)$ when $\Re(Tx^2) < -1$ we then need to change

[1] Consider two arbitrary contours connecting the origin and Tx^2, Γ_1 and Γ_2, that do not intersect one another. As no residues are present, the integral over the contour $\Gamma_1 \cup \bar{\Gamma}_2$ must vanish — where $\bar{\Gamma}_2$ stands for Γ_2 with opposite curve orientation — hence the equivalency of the contours.

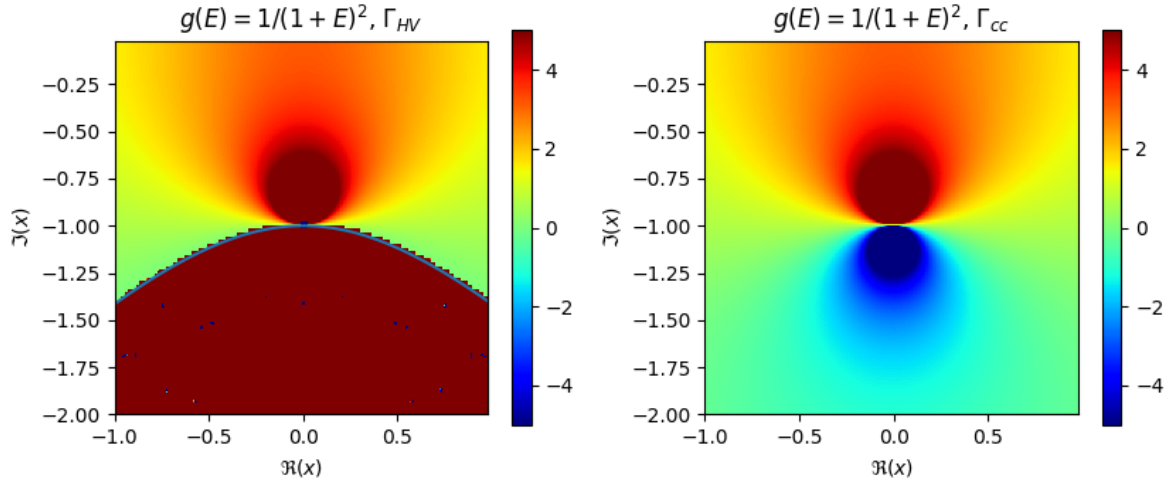

Figure 8.2: κ distribution case. **Left** - 'wrong' contour Γ_{HV} intercepting the singularity. **Right** - Corrected contour, as per Eq. (8.5)

contour in a way to get around ξ_s. Since the residue in ξ_s is zero, the specific contour chosen does not matter, as long as it does not intercept the discontinuity.[2]

We then integrate as follows:

$$\int_0^{Tx^2} ... = \int_0^{z0} ... + \int_{z0}^{z_1} ... + \int_{z_1}^{Tx^2} ..., \tag{8.5}$$

where z_0 and z_1 are any two complex numbers that allow to avoid the point ξ_s. The integral function with $g(E) = 1/(1+E)^2$ can be observed in the right sub-figure of Fig. 8.4. Therefore, with a proper adjustment of the integration contour, κ distributions are in general well defined and the integral $G(z)$ does not raise any issue.[3]

However, the good behaviour of κ distribution relies on the null residues of its singularities. If $g(\xi)$ exhibits a singularity with residue different than zero, a line discontinuity cannot be avoided. If we repeat the same reasoning of footnote 1 (previous page), but by including a singularity with residue different than zero, we immediately deduce that different contours lead to different integral values and that a discontinuity has to be created.

As an example, we consider $g(E) = 1/(1+E^2)^2$, singular at $\xi_s = \pm i$, and two different integration contour methods, Γ_{VH} and Γ_R. Γ_{VH} consists of a vertical segment from $0 + i0$ to $i\Im(Tx^2)$ and a horizontal segment from $i\Im(Tx^2)$ to Tx^2; Γ_R consists of a segment from 0 to Tx^2 at fixed phase angle ξ (both contours are shown in Fig. 8.1). The results for $G(x)$ are shown in Fig. 8.3 and we conclude that the complex singularities of $F_0(\xi)$ generate line discontinuities for $G(x)$, whose orientation depends on the chosen contour method.

8.1.2 Cut-off Discontinuity

Analogously to the observations of Chapter 4, a discontinuity can be induced by the step of the cut-off distributions. We set $g(E) = g_0(E)H(E_c - E)$, and we observe that on the real axis

$$G(t) = \int_{Tt^2}^{\infty} g_0(E)H(E_c - E)\mathrm{d}E = H(E_c - Tt^2) \cdot \int_{Tt^2}^{E_c} g_0(E)\mathrm{d}E. \tag{8.6}$$

[2]Going around around the discontinuity is equivalent to take the principal value of a diverging integral. But since the implementation of a principal value would be more complicated, we prefer going around the singularity.

[3]As it could have been easily predicted by observing that the integral $\int \mathrm{d}\xi 1/(1+\xi)^\kappa$ is well defined and equal to $(1+E)^{-\kappa+1}/(-\kappa+1)$, provided $\kappa > 1$.

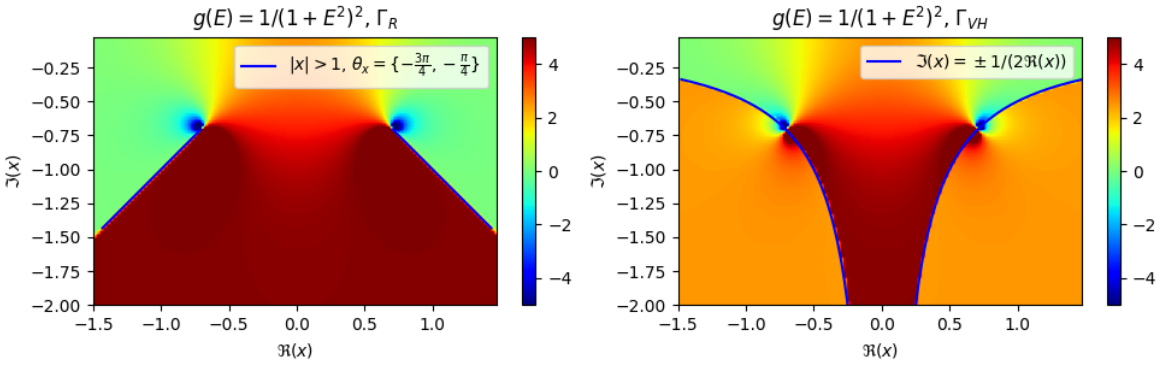

Figure 8.3: Singularity discontinuities for $G(x)$ when $g(E) = 1/(1+E^2)^2$. We notice the different discontinuities (blue curves) arising, depending on the chosen contour, Γ_R (**Left**) and Γ_{VH} (**Right**).

Assuming $g_0(E)$ is well-behaved, we can define G in the complex plane by replacing t with the complex variable x and by arbitrarlily choosing $H(E_c - \Re(Tx^2))$ as the complex definition of $H(E_c - Tt^2)$. Moreover we choose the complex contour Γ_{HV}. The complex variable function $G(z)$, and correspondingly $Z(z, G)$, is then discontinuous at $\Re(Tx^2) = E_c$, or, equivalently, at $\Im(x) = \pm\sqrt{\Re(x)^2 - E_c/T}$.

Can we smooth out the discontinuity with the same approach used for Landau damping? At first impact, one might be temped to introduce a sigmoid function to smooth out the function g_0. However, neither one of the sigmoids that have been mentioned in the present work, seem to be working. The logistic function is not removing the discontinuity because of its complex plane singularities; on the other hand, despite not presenting the singularity problem of the logistic function, the erf sigmoid has an excessively complicated structure and it is very prone to overflow.

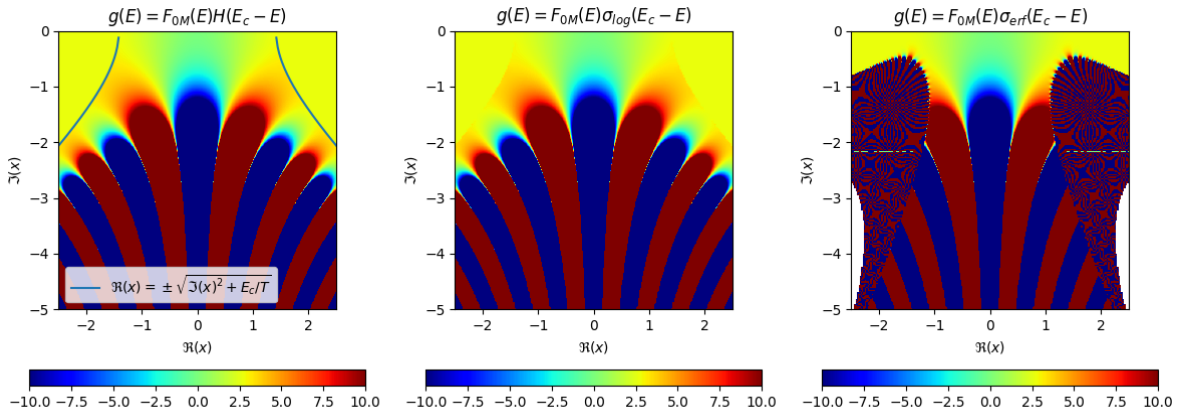

Figure 8.4: Cut-off discontinuity (**Left**) and 'smoothing' attempts with $\sigma_{log,\alpha=0.2}$ (**Center**) and $\sigma_{erf,\alpha=0.5}$ (**Right**). A Maxwellian is chosen as support function $g_0(E)$.

8.1.3 Branch Cut Discontinuity

A third type of discontinuity is related to the branch cut of functions such as $1/(1+E^r)$, with non integer r power dependency. In this case, we choose to place the branch cut of E^r on the negative real semi-axis. Setting $Tx_s^2 = [-\infty, 0]$ yields that the singular points associated to the branch cut discontinuity correspond to the whole imaginary axis. An illustration of this, $r = 1.5$ is given and commented for the Slowing Down case in Fig. 8.5.

8.1.4 Summary Example: Slowing Down

Let us summarize the previous cases in a single example, represented by a Slowing Down distribution with $E_t = 1$.

$$g(E) = \frac{1}{1+E^{1.5}} H(E_c - E). \tag{8.7}$$

In Fig. 8.5, we plot the real and imaginary part of $G(x) = \int_{Tx^2}^{\infty} g(\xi)\mathrm{d}\xi$, using the Γ_{HV} and Γ_R. For the contour Γ_{HV} (left sub-figure) the following comments on the discontinuities can be made:

- Singularity: $g_0(E)$ has three singularities: $E_s = \exp(-2\pi/3)$, $\exp(2\pi/3)$, $\exp(2\pi)$. Only the first two belong to the selected Riemann surface $[-\pi, \pi]$. By setting $Tx^2 = E_s$ we get four points in the x-plane, $x_s = \exp(\pm\pi/3)$, $\exp(\pm 4\pi/3)$. The chosen contour Γ_{HV} will hit a singularity, and then produce a discontinuity, at $\Re(Tx^2) = \Re(E_s)$, $|\Im(Tx^2)| > \Im(E_s)$.
- Cut-off: the $\Im(x) = \pm\sqrt{\Re(x)^2 - E_c/T}$ curves correspond to the $H(E_c - \Re(E))$ cut-off. Clearly, the definition in the complex plane is arbitrary and an infinity of other definition could be chosen to extend $H(E_c - E)$ into the complex plane.
- Branch cut: according to Subsection 8.1.3, we would expect a discontinuity on the imaginary axis. To explain why this is not observed, let us consider two points $E_\pm = -a \pm i\epsilon$ ($a < 0$) located on different sides of the branch cut. $\mathrm{G}(E_\pm = -a \pm i\epsilon)$ will then be:

$$G(E_\pm) = \int_{\pm\epsilon}^{-a} g(E)\mathrm{d}E + \int_{-a}^{\infty} g(E)\mathrm{d}E. \tag{8.8}$$

  It is clear then, as $\epsilon \to 0$, $|G(E_+) - G(E_-)| \to 0$, hence proving that $G(z)$ is continuous around on branch cut. However, continuity does not imply analyticity. Indeed, $G(z)$ is not analytical on the branch cut: as $g(E_+) \neq g(E_-)$ the derivative is discontinuous.

Fig. 8.5 shows the case with Γ_R as well. Similar considerations apply. However, in contrast to the Γ_{HV} case, the branch cut discontinuity appears, while the cut-off one disappears. As before, the discontinuity is only hidden and it is retained in the derivative of $G(z)$. In general, whether a discontinuity gets hidden or not depends on the orientation of the contour w.r.t. the line discontinuities of $g(E)$: if it cuts the $g(E)$ discontinuity transversally, then the discontinuity of $G(E)$ is hidden.

8.2 What Consequences?

The preceding section illustrates that the integral term $\int_{Tx^2}^{\infty} g(E)\mathrm{d}E$ is generally associated to discontinuities in the complex plane. Since each one of the terms $\tilde{D}$, $\tilde{N}$ and $\tilde{H}$ contains such an integral, the dispersion relation will be discontinuous in the LHP.

In Chapter 4 we showed for the linear Vlasov-Poisson system that if the dispersion relation is discontinuous, the residue contribution coming from the roots of the dispersion relation is

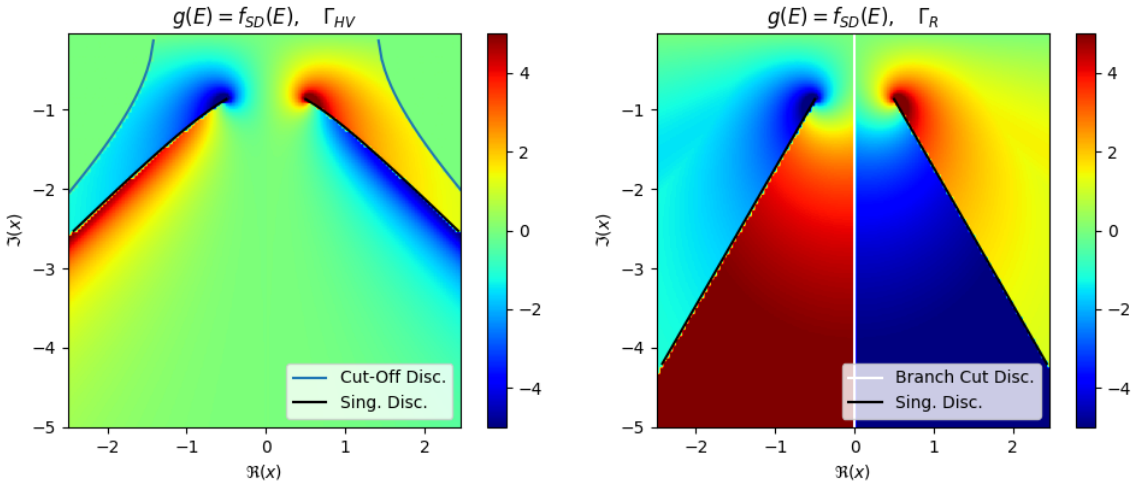

Figure 8.5: $G(x)$ discontinuities for the Slowing-Down case, $g(E) = f_{SD}(E)$, with two different contours, Γ_{HV} (**Left**) and Γ_R (**Right**).

only part of the electric field solution. To evaluate the remaining component we had to resort to the integration around the discontinuity lines of the Laplace transform of the electric field E. However, such integration was made possible by the initial value treatment we adopted for the linear Vlasov-Poisson system. An eigenvalue formulation would lead exclusively to the dispersion relation, and the evaluation of the discontinuity contributions would be precluded.

The linear gyrokinetic dispersion relation emerges from an eigenvalue formulation. As such no direct access to the discontinuity contribution seems possible. Two possible scenarios are then foreseen:

1. **Simple scenario:** the discontinuities influence the dispersion relation and the pole structure only marginally. We retain the eigenvalue formulation and neglect the contributions from the discontinuities.

2. **Not as simple scenario:** the discontinuities significantly impact the dispersion relation and the pole structure. An initial value reformulation is required.

Determining which scenario applies to the linear gyrokinetic problem is left for future investigation. Especially for the latter scenario, understanding how the GAMs pole extraction mechanism relates to the multiple LHP descriptions may be interesting.

For the preliminary testing of the next chapter we restrict ourselves to the simple scenario.

Chapter 9

Preliminary Results for GAMs

In the current and last chapter we present the outcomes of the preliminary investigation, based on the newly introduced dispersion relation, of Geodesic Acoustic Modes (GAMs). After a brief introduction to the GAMs dispersion relation (Sec. 9.1) we proceed to its visualization for two distinct scenarios: an ion-electron plasma with different ion distribution functions (Sec. 9.2), and an ion-electron-α plasma with different α distribution functions (Sec. 9.3). The main goal of this chapter is to run some simple test cases to show that the implementation of the framework built in the present thesis, comprising the extended dispersion relation and Xie's algorythm, yields plausible results. Consequently, our discussion here will be intentionally concise, and a comprehensive and systematic exploration of the underlying physics depicted in the presented plots is deferred to future work. For the time being we just invite the reader to sit back and enjoy the plots that illustrate the challenges of the problems.

9.1 Dispersion Relation

In Sec. 6.5 we have qualitatively introduced GAMs. Now, from a more rigorous standpoint, the dispersion relation for GAMs can be derived by simplifying the general dispersion relation Eq. (7.25) and setting m, n, $k_{m,\theta}$, and $k_{m,\|}$ to zero. The resulting expression for the GAMs dispersion relation is thus given by:

$$\omega^2 = \frac{2v_{thi}^2}{R_0^2}\left(-2H(x_1) + 2\tau\frac{N(x_1)^2}{D(x_1)}\right), \tag{9.1}$$

where terms involving ∇F_0 in the definitions of D, N, and H vanish, leading to the omission of the superscript for these terms.

At a fixed value for $k_{1,\|} = 1/qR$, Eq.(9.1) can be represented as $\mathbf{DR}(\omega) = 0$. In the following sections, we plot the absolute value $|\mathbf{DR}(\omega)|$ for two distinct cases: a 2 species plasma comprising ions and electrons, and a 3 species plasma with an additional population of α particles.

9.2 Ion-Electron Plasma

The first scenario correspond to a 2 species, ions and electrons, plasma. The typical reference case for GAMs consist of ions and electrons distributed according to a Maxwellian distribution. Here, as a test for our implementation we replace the ion Maxwellian distribution with a κ distribution and we keep electrons with a Maxwellian distribution[1] Specifically, we choose the

[1]It can be verified that electrons exert a small contribution on the dispersion relation. This is why we vary the ion distribution function and leave the electrons unchanged.

following parameters:

- General: $q = 1$, $B = 5\text{T}$, $R = 6.2\text{m}$, $n_0 = 10^{20}\text{m}^{-3}$
- Electrons: $T = 8\text{keV}$, Maxwellian.
- Ions: $T = 8\text{keV}$, Maxwellian and κ distribution with $= \{16, 40\}$

The κ distribution is taken from Ref. [25] and it is given as

$$f_\kappa(E) = \frac{m^{3/2}}{(2\pi T(\kappa - 0.5))^{3/2}} \frac{\Gamma(\kappa + 1)}{\Gamma(\kappa - 1/2)} \left[1 + \frac{E}{T(\kappa - 1/2)}\right]^{-\kappa - 1} \tag{9.2}$$

The results are shown in Fig. 9.1. A tendency analogous to the one observed in Chapter 3 is spotted, with κ roots approaching Maxwellian roots as κ grows. Since the reference case with Maxwellian ions and Maxwellian electrons is computed by using the non-generalized D, N and H terms, as per Eqs. (7.33), (7.34) and (7.35), the same figure is also proof that the adopted implementation works, at least in this case, smoothly.

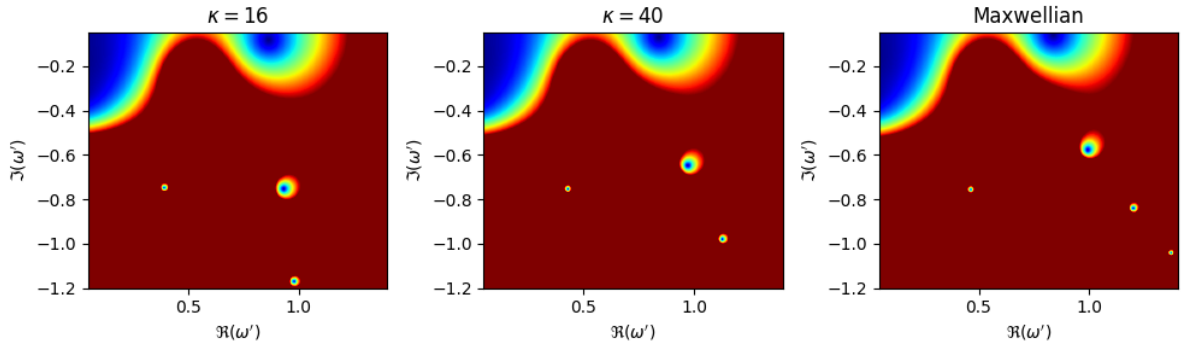

Figure 9.1: GAMs dispersion relation $|DR(\omega)| = 0$ for an ion-electron plasma. Ion distribution functions: $f_{\kappa=16}$ (**Left**), $f_{\kappa=40}$ (**Center**), Maxwellian (**Right**).

9.3 Ion-Electron-α Plasma

The previous scenario is of limited interest since the ion distribution is never a κ distribution in a tokamak plasma. We then consider a more interesting case, where we add an α-population to the ion-electron plasma.

We assume ions and electrons to be distributed according to a Maxwellian with temperature $T = 8\text{keV}$. General parameters are the same as in the previous section. For the α population we choose three different distributions:

- **Maxwellian**, $T = 667\text{keV}$, α-fraction $n_{0\alpha}/n_{0e} = \{0, 0.01, 0.1\}$ (Fig. 9.2).
- **Incomplete Maxwellian**, $T = 667\text{keV}$, cut-energy $E_0 = 1500\text{keV}$, α-fraction $n_{0\alpha}/n_{0e} = \{0, 0.01, 0.1\}$ (Fig. 9.3).

- **Slowing-Down**[2], birth energy $E_0 = 3520$keV, $E_c = 667$keV, $\Delta E = 335$keV, α-fraction $n_{0\alpha}/n_{0e} = \{0, 0.1, 0.4\}$ (Fig. 9.4).

Figs.9.2, 9.3 and 9.4 depict the GAMs modes with the different distributions for αs, at different α-fractions. By observing the figures we can categorize the roots into two classes, and a few general considerations can be made:

- The first class consists of those roots that appear in the ion-electron plasma (case $\alpha = 0$) and move in the complex plane as the α-fraction is increased. The general tendency of these roots, independent from the chosen distribution, is that they move deeper into the complex plane, i.e., their damping coefficient increases as the α-fraction grows. By drawing an analogy with Landau damping and the general properties of Sec. 2.2, we can argue that the α distributions chosen here are stabilizing. They do not feature any positive gradient $\partial F_0/\partial E$ region and they just act as an extra species drawing energy from the wave, hence increasing the damping.

- The second class consists of those roots that are specifically introduced by the chosen α-population. In particular:

  - Maxwellian, Fig. 9.2: we observe a new root that approaches the real axis as the α-fraction is increased.
  - Incomplete-Maxwellian, Fig. 9.3: the same root observed for the Maxwellian seems to appear for the $\alpha = 0.01$ case, but it is partially cut away by the cut-off discontinuity (refer to Sec. 8.1.2) represented by the white line. For the $\alpha = 0.1$ case a stable root is observed. In analogy to a previous discussion relating singularities in the LHP and the roots of the dispersion relation (Sec.2.2), this root is likely related to the singularity of the integral
  $$\text{P.V.}\int_{-v_c}^{v_c} \frac{F_0(v)}{v - z} dv, \tag{9.4}$$
  where $F_0(v)$ is an incomplete Maxwellian, i.e., $F_0(v) = 0$ for $|v| > v_c$. The principal value allows to avoid the divergence of the integral as long as $z \in (-v_c, v_c)$, but when $z = v_c$ the P.V. integral approaching v_c from $v_c + \varepsilon$ is null, and the integral approaching v_c from $v_c - \varepsilon$ diverges, hence the singularity.
  - Slowing-Down, Fig.9.4: no extra roots are observed.

Given the considerations above, we believe that these plots, after proper exploration, bear an interesting idea that might be worth exploring. In Sec. 6.5 we mentioned the EGAMs mechanism that extracts GAMs roots from the lower half-plane. Clearly, the chosen distributions of α particles are not suitable for extracting GAMs roots from the lower half plane, since they do not have free-energy regions with positive gradient, and indeed we showed that they move the $\alpha = 0$ damped roots further down into the lower half-plane. However, instead of considering the case of Ref. [34], where EGAMs by an unstable distribution, e.g., bump on tail, are excited from the stable Maxwellian GAM root in ion-electron plasmas, we consider the EGAM excitation from an ion-electron-α plasma by an additional anisotropic EPs species (NBI, ICRF).

[2]Here, we use the Slowing-Down definition from Ref. [35]:

$$f_{SD}(E) = \frac{N}{E_c^{3/2} + E^{3/2}} \,\text{erfc}\left(\frac{E - E_0}{\Delta E}\right), \tag{9.3}$$

where erfc stands for the complementary error function and N is the normalization constant.

Coming back to the discussion of the previous chapter about the challenges related to the discontinuities of the dispersion relation, we observe a clear discontinuity for the incomplete Maxwellian case at α-fraction $\alpha = 0.01$, but not at $\alpha = 0.1$. Moreover, for the Slowing-Down case, we do not observe neither the complicated structure induced the erf sigmoid (see right subfigure of Fig. 8.4) nor the singularity discontinuities (see Fig. 8.5) that we showed for the Slowing-Down case. Understanding the reasons for that needs further investigation.

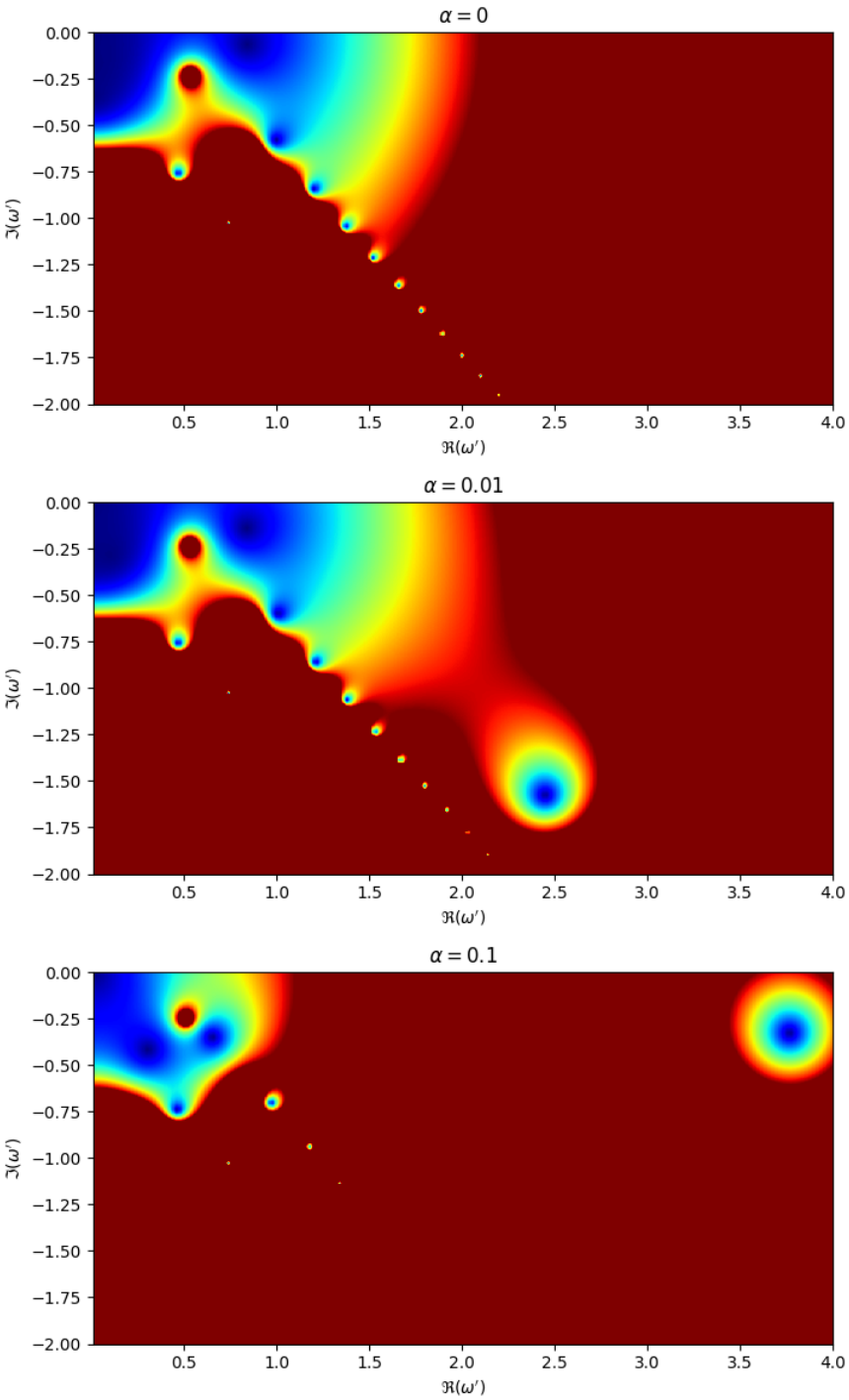

Figure 9.2: Maxwellian distribution for αs - GAMs dispersion relation $|DR(\omega)| = 0$ for an ion-electron-α plasma. α-fraction is 0 (**Top**), 0.01 (**Center**), 0.1 (**Bottom**).

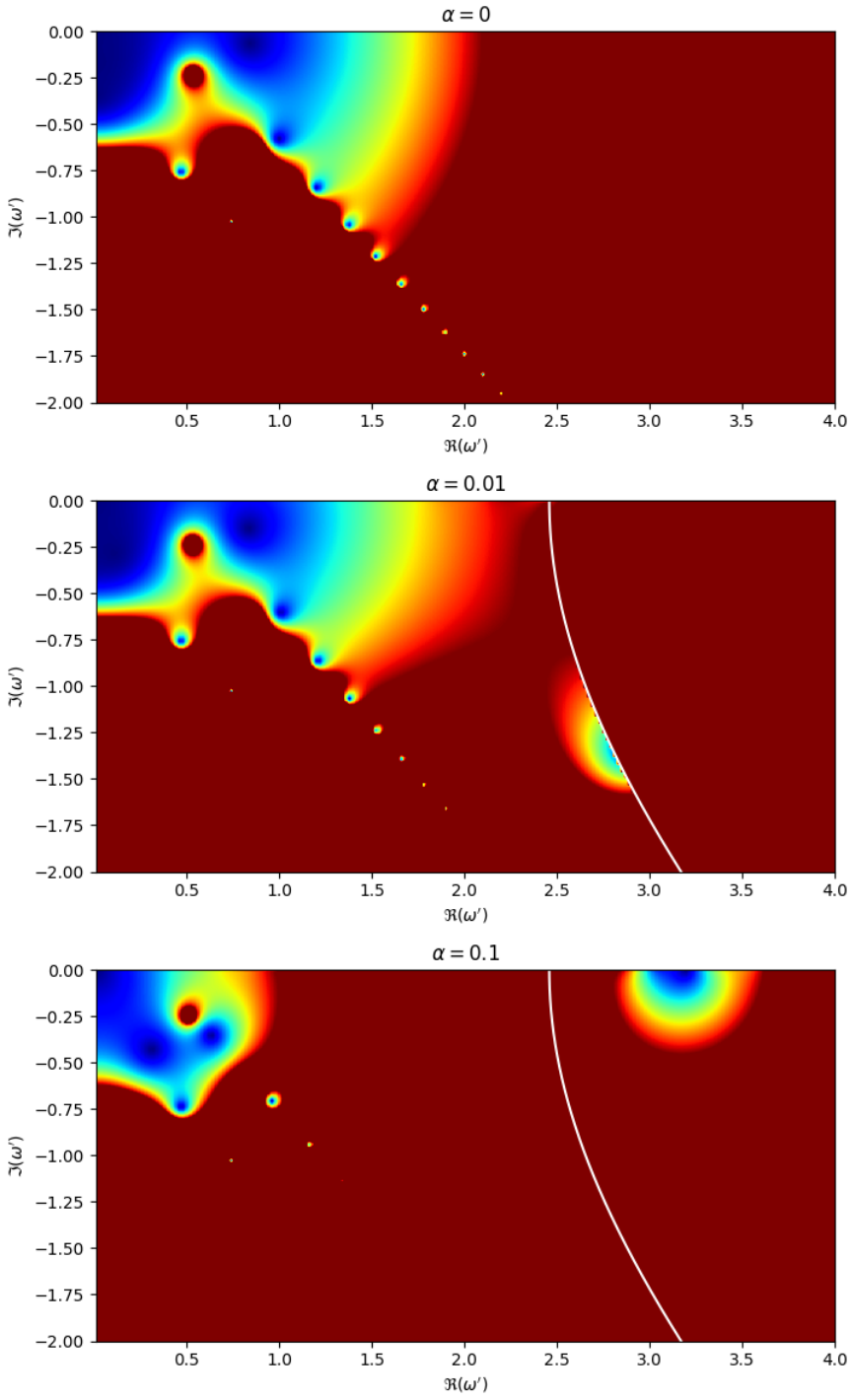

Figure 9.3: Incomplete Maxwellian distribution for αs - GAMs dispersion relation $|DR(\omega)| = 0$ for an ion-electron-α plasma. α-fraction is 0 (**Top**), 0.01 (**Center**), 0.1 (**Bottom**). The white line represents the cut-off discontinuity.

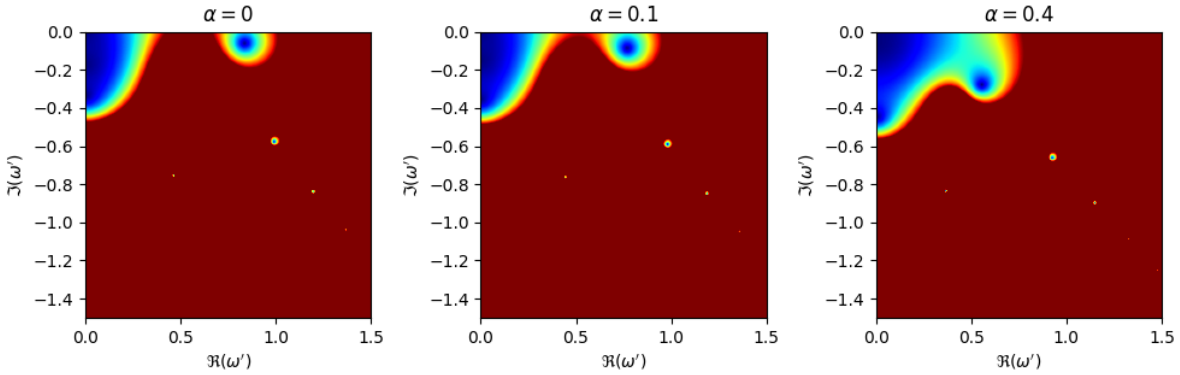

Figure 9.4: Slowing-Down distribution for αs - GAMs dispersion relation $|DR(\omega)| = 0$ for an ion-electron-α plasma. α-fraction is 0 (**Left**), 0.01 (**Center**), 0.1 (**Right**).

Conclusions & Outlook

We conclude the master's thesis by summarizing its main contents and by identifying possible directions for future investigations.

In Part I we tackled the Landau damping problem for non-Maxwellian distribution functions. In particular:

- In Chapter 1 we provided an overview of the main physical interpretation of Landau damping, with the additional contribution of illustrations that we believe might facilitate the intuitive understanding of the phenomenon.
- In Chapter 2 the Landau's approach to the linear Vlasov-Poisson system has been presented, in terms of formal derivation and solution properties; we included a discussion about the number of damped solutions.
- In Chapter 3 Maxwellian and κ distributions were analysed. We described analytically the Maxwellian multi-pole structure and we speculated on a potential link between particle correlation and multiple solutions to the linear Vlasov-Poisson system.
- In Chapter 4 we focused on distribution functions with non-unique analytical continuations. After confirming that the different treatments provided in literature are equivalent, we approached the problem with a novel method by means of sigmoid functions. In particular, the method proved successful in the case of a Slowing-Down distribution.

Between Part I and Part I, we presented and reviewed Xie's algorithm, a crucial tool for our work, that allows to compute the Hilbert transform for arbitrary input functions. Minor modifications were incorporated, and an error analysis was conducted.

In Part II we dived into the fusion field and we concentrated on the linear gyrokinetic dispersion relation. Specifically:

- In Chapter 7 we generalized the original dispersion relation to non-Maxwellian distributions, by rewriting it in a way that allows the immediate integration of Xie's algorithm. In addition, we verified the correctness of the new formulas with a comparison to the reference Maxwellian case.
- In Chapter 8 we presented some critical points, in terms of discontinuities in the lower half-plane, related to the complex plane extension of the dispersion relation.
- In Chapter 9 we showed some preliminary results for the generalized dispersion relation in the case of Geodesic Acoustic Modes (GAMs).

Outlook

Looking ahead, possible paths for further exploration include:

- Improving the understanding of discontinuities in the context of GAMs generated by non-Maxwellian distributions, in order to be able to accurately and reliably express solutions of the linear gyrokinetic dispersion relation.
- Inspecting how the EGAM extraction mechanism is influenced by different EPs distribution functions (α and NBI).
- Completing the presented framework, that integrates Xie's algorithm into the generalized dispersion relation, to include finite toroidal mode numbers, and implementing it in the LIGKA code.
- With the completed framework, reviewing the first two points for finite toroidal numbers and investigating the role of non-Maxwellians for quasi-linear and non-linear transport theories [41] especially in relation to multi-modes systems comprising EPs.

On the more fundamental level, in relation to the Landau damping problem, potential lines of investigation are:

- Understanding the physical meaning, provided it exists, of the different lower half-plane descriptions for functions that do non admit a unique analytical continuation.
- Seeking a rigorous mathematical description for the speculation regarding a possible connection between particle correlation and the solution to the Landau damping problem.

Bibliography

[1] C. Tsallis, E. Brigatti, *Continuum Mechanics and Thermodynamics* **2004**, *16*, 223–235.

[2] G. Livadiotis, *Journal of Geophysical Research: Space Physics* **2015**, *120*, 1607–1619.

[3] J. D. Gaffey, *Journal of Plasma Physics* **1976**, *16*, 149–169.

[4] P. Lauber, *Physics Reports* **2013**, *533*, 33–68.

[5] H.-S. Xie, *Physics of Plasmas* **2013**, *20*, 092125.

[6] F. F. Chen et al., *Introduction to plasma physics and controlled fusion*, *Vol. 1*, Springer, **1984**.

[7] T. O'neil, *The physics of fluids* **1965**, *8*, 2255–2262.

[8] A. Vlasov, *Russ. Phys. J.* **1945**, *9*, 25–40.

[9] L. Landau, *Journ. of Phys.* **1946**, *10*, 25–34.

[10] N. G. Van Kampen, *Physica* **1955**, *21*, 949–963.

[11] J. Malmberg, C. Wharton, *Physical Review Letters* **1964**, *13*, 184.

[12] J. Dawson, *The physics of fluids* **1961**, *4*, 869–874.

[13] D. Ryutov, *Plasma physics and controlled fusion* **1999**, *41*, A1.

[14] C. Mouhot, C. Villani, *On Landau damping*, **2011**.

[15] T. H. Stix, *The theory of plasma waves*, **1962**.

[16] P. Stubbe, A. Sukhorukov, *Physics of Plasmas* **1999**, *6*, 2976–2988.

[17] H. Y., *Notes on Landau damping*, Institute of Plasmas, Chinese Academy of Sciences, **2013**.

[18] R. Bilato, M. Brambilla, *Communications in Nonlinear Science and Numerical Simulation* **2008**, *13*, 18–23.

[19] G. Backus, *Journal of Mathematical Physics* **1960**, *1*, 178–191.

[20] G. Belmont, F. Mottez, T. Chust, S. Hess, *Physics of Plasmas* **2008**, *15*, 052310.

[21] E. Meyer, G. Sessler, *Zeitschrift für Physik* **1957**, *149*, 15–39.

[22] A. Sukhorukov, P. Stubbe, *Physics of Plasmas* **1995**, *2*, 4059–4074.

[23] D. F. Escande, D. Bénisti, Y. Elskens, D. Zarzoso, F. Doveil, *Reviews of Modern Plasma Physics* **2018**, *2*, 1–68.

[24] R. Z. Sagdeev, A. A. Galeev, *Nonlinear plasma theory*, **1969**.

[25] M. Lazar, H. Fichtner, *Kappa Distributions*, Springer, **2021**.

[26] G. Livadiotis, *Entropy* **2015**, *17*, 2062–2081.

[27] G. Livadiotis, D. J. McComas, *The Astrophysical Journal* **2022**, *940*, 83.

[28] J. Lima, R. Silva Jr, J. Santos, *Physical Review E* **2000**, *61*, 3260.

[29] E. Saberian, G. Livadiotis, *Physica A: Statistical Mechanics and its Applications* **2022**, *593*, 126909.

[30] H. Weitzner, *The Physics of Fluids* **1963**, *6*, 1123–1127.

[31] R. Twiss, *Physical Review* **1952**, *88*, 1392.

[32] B. Godfrey, B. Newberger, K. Taggart, *IEEE Plas. Sci.* **1975**, *2*, 60–67.

[33] J. F. Hudson, **1962**, *58*, 119–129.

[34] J.-B. Girardo, PhD thesis, Ecode doctorale de l'Ecole Polytechnique (EDX), **2015**.

[35] P. Lauber, PhD thesis, **2003**.

[36] H.-S. Xie, Supplemetary material for [5] with the MATLAB numerical implementation. **2013**, `https://doi.org/10.1063/1.4822332`.

[37] J. Citrin, P. Mantica, *Plasma Physics and Controlled Fusion* **2023**, *65*, 033001.

[38] H. Sugama, *Physics of Plasmas* **2000**, *7*, 466–480.

[39] L. Chen, F. Zonca, *Reviews of Modern Physics* **2016**, *88*, 015008.

[40] P. Lauber, *Private Communication*, **2023**.

[41] A. N. Kaufman, *The Physics of Fluids* **1972**, *15*, 1063–1069.

Acknowledgments

During the course of my master's thesis at IPP, I have had the pleasure of sharing the time and work with many great people, that made my year long plasma-journey not only academically fulfilling, but also extremely enriching on a personal level.

In particular, I am deeply grateful to my supervisor Dr. Philipp Lauber on multiple fronts. Firstly, for the project he chose for me, aligned with my explicit request for an analytical focus. Secondly, for his guidance, support, and the invaluable knowledge he shared with me during our discussions. Lastly, and most importantly, for welcoming me in his amazing research group and for making me feel integral part of it.

A special thanks to my fellow adventurers in office 130 and in the L7A building. Our shared moments, be they breaks, chats, music-plasma work evenings, or mythological obliterations, have added a truly enjoyable dimension to my year at IPP. Particularly in the last weeks, I am sincerely grateful for the support that propelled me towards the conclusion of the thesis.

Lastly, I am thankful to my family for their constant support, and for the privilege I have been given to study abroad and pursue my passions.